Single-crystalline GaP waveguide-integrated resonators on diamond for future quantum information processing applications

Nicole K. Thomas

A dissertation

submitted in partial fulfillment of the

requirements for the degree of

Doctor of Philosophy

University of Washington

2014

Reading Committee:

Kai-Mei C. Fu, Chair

Lih Y. Lin

Karl Böhringer

Program Authorized to Offer Degree:

Electrical Engineering

University of Washington

Abstract

Single-crystalline GaP waveguide-integrated resonators on diamond for future quantum information processing applications

Nicole K. Thomas

Chair of the Supervisory Committee:

Dr. Kai-Mei Fu

Electrical Engineering

The nitrogen-vacancy (NV) defect center in diamond is considered a promising quantum bit system due its long spin coherence time, the possibility for optical manipulation and read-out and integration into solid-state photonic networks. Multi-qubit entanglement generation is essential for novel quantum information processing applications based on measurement-based quantum computing. Linear electro-optic materials such as gallium phosphide (GaP) may be crucial for the implementation of active optical device functionalities in these networks. Currently, the

realization of coupled GaP photonic structures with diamond has been limited due to the lack of high-quality GaP layers on diamond.

This dissertation explores different approaches toward the integration of GaP coupled optical device structures with near-surface NV centers in diamond. Initially, GaP layers grown directly on diamond using a molecular beam epitaxy system are evaluated for their optical loss properties, and found to be inadequate for the realization of high-quality GaP micro-cavity structures. Thereafter, different approaches for the transfer of single-crystalline, sub-micrometer thick GaP device layers onto diamond are investigated. Reliable transfer is achieved by an epitaxial lift-off process and subsequent van der Waals bonding of mm^2-sized GaP sheets on the diamond substrate. GaP disk resonator structures integrated with bus waveguides are implemented, and their device properties are shown to be promising for the efficient collection and coupling of the relevant NV spectral line. Finally, coupling of the NV emission to a hybrid GaP\diamond optical network and on-chip photon routing is demonstrated. The work presented here is expected to open the path toward the realization of large-scale optical networks with active device functionalities, which may eventually enable high-fidelity entanglement generation between distant NV qubits in the diamond substrate.

Table of Contents

List of Tables

List of Figures

List of Abbreviations

Abbreviation	Description
2-D	Two-dimensional
3-D	Three-dimensional
AFM	Atomic force microscopy
AlGaP	Aluminum gallium phosphide
AlN	Aluminum nitride
Al_2O_3	Aluminum oxide
Ar	Argon
BCl_3	Boron trichloride
BOE	Buffered oxide etch
C	Carbon
CdSe/ZnS	Cadmium selenide/zinc sulfide
CCD	Charge-coupled device
Cl_2	Chlorine
CMP	Chemical mechanical polishing
cw	Continuous-wave
CVD	Chemical vapor deposition
DC	Direct current
DI H_2O	De-ionized water
EO	Electro-optic
FDTD	Finite-difference time-domain
Ga	Gallium
GaAs	Gallium arsenide
GaP	Gallium phosphide
H_2	Hydrogen
HCl	Hydrochloric acid
HF	Hydrofluoric acid
HMDS	Hexamethyldisilazane
HT	High-temperature
HPHT	High-pressure high-temperature
HSQ	Hydrogen silsesquioxane
ICP-RIE	Inductively-coupled plasma reactive ion etching
IPA	Isopropyl alcohol

$K_3Fe(CN)_6$	Potassium ferricyanide
KOH	Potassium hydroxide
LED	Light-emitting diode
LER	Line edge roughness
LT	Low-temperature
MBQC	Measurement-based quantum computing
MBD	Molecular beam deposition
MBE	Molecular beam epitaxy
MPI	Message passing interface
N	Nitrogen
NV	Nitrogen-vacancy center
NV^-	Negatively charged nitrogen-vacancy center
NV^0	Neutral nitrogen-vacancy center
QD	Quantum dot
QIP	Quantum information processing
qubit	Quantum bit
PECVD	Plasma enhanced chemical vapor deposition
PhC	Photonic crystal cavity
P_2	Phosphorous
PL	Photoluminescence
PSB	Phonon sideband
RF	Radio-frequency
RHEED	Reflection high-energy electron diffraction
RMS	Root-mean-square
SEM	Scanning electron microscopy
SF_6	Sulfur hexafluoride
Si	Silicon
SIL	Solid immersion lens
SiO_2	Silicon dioxide
TE	Transverse electric
TEM	Transmission electron microscopy
Ti	Titanium
TM	Transverse magnetic
ZPL	Zero-phonon line

Chapter 1:
Introduction

The integration of quantum mechanical systems, such as ions, electrons, or photons, with nano-scale device structures for active manipulation and read-out is expected to open up new technological applications. Two quantum properties in particular, superposition and entanglement, are essential to novel quantum information processing (QIP) systems. In a classical computing architecture, j bits can represent one state out of 2^j permutations at a time. In QIP, the smallest unit of information is the quantum bit (qubit), which can exist in an arbitrary vector superposition of 0 and 1. Thereby, superposition allows j qubits to be concurrently present in all 2^j states. This enables the implementation of novel computing architectures, with applications, for example, in large-scale classical or quantum simulations [1], [2], cryptography [3]–[5], and optimized search algorithms [6]. There are many theoretical quantum information protocols, and this work aims to develop fundamental technologies to enable the particularly promising measurement-based, or one-way, quantum computing (MBQC). MBQC relies on the preparation of numerous qubits in an entangled state: The computational algorithm is then driven through the system solely by measurement on single qubits, eliminating the need for two-qubit gates that depend on physical proximity of the qubits [7]–[9].

While numerous qubit systems are currently under investigation [10]–[14], the negatively charged nitrogen-vacancy (NV^-) defect in diamond is considered a particular promising candidate due to long spin coherence times and the ability to perform optical initialization and read-out, which are essential for the MBQC platform [15]–[17]. Spin coherence times affect the

maximum possible computation time. Entanglement generation between two NV^- center electron spins by a free-space photon interference measurement has recently been demonstrated [18]. However, the entanglement process is currently characterized by a low success rate, due to the limited collection efficiency for the relevant zero-phonon-line (ZPL) photons in free space. Coupling of the NV^- ZPL emission to integrated optical networks should significantly improve this efficiency, due to photon emission rates being enhanced in the fields of a resonant micro-cavity structure [19]. All-diamond photonic networks have been used successfully to enhance the ZPL photon collection efficiency and couple the NV^- emission off-chip [20]–[23]. Large-scale functional entanglement networks, however, will require active photonic device capabilities, which are currently limited in the all-diamond platform [24], [25].

Here, as an alternative to the all-diamond approach, the implementation of a hybrid material system, consisting of a gallium phosphide (GaP) device layer on diamond, is investigated for use in optical entanglement networks. GaP is a high refractive index, linear electro-optic material and may therefore be utilized as a tunable waveguiding layer on diamond substrates prepared with near-surface NV^- centers [26], [27]. Linear electro-optic devices implemented from similar materials have been employed as effective optical modulators with small footprint and facile fabrication approaches [28]. Hence, hybrid integrated networks combining the promising NV^- characteristics with the tunable optical properties of GaP could be a viable solution for future QIP applications.

While single GaP\diamond resonator structures have been implemented [29], [30], the realization of complex hybrid networks remains an unsolved challenge due the availability of high-quality GaP device layers on diamond. Thus, the implementation of waveguide-integrated GaP cavity structures on diamond for passive photon collection and routing is a critical step

toward demonstrating the feasibility of large-scale optical networks for entanglement generation in hybrid systems.

The work described in the following chapters aims to explore different approaches toward the realization of passive coupled GaP photonic device structures on diamond substrates. Two avenues are investigated: deposition of GaP directly on diamond and transfer of sub-micrometer thick GaP sheets epitaxially grown on a secondary substrate. Single-crystalline waveguide-integrated GaP resonators are successfully fabricated using the latter method. The device characteristics are demonstrated to be promising for efficient collection of NV^- ZPL photons. Furthermore, off-chip coupling of the NV^- emission using hybrid GaP\diamond structures is achieved. This work opens the path toward the integration of a linear electro-optic material on diamond for the realization of future optical networks with active device capabilities.

The remainder of this dissertation is organized as follows:

Chapter 2 provides a brief introduction to one-way quantum computing and the NV^- qubit system in diamond. Furthermore, all-diamond photonic networks for QIP are reviewed, and the investigation of hybrid GaP\diamond optical networks is motivated.

In chapter 3, the potential of polycrystalline GaP layers deposited directly on diamond substrates with near-surface NV^- centers is evaluated for the realization of high-quality photonic devices. Properties of the GaP layers, deposited in a molecular beam epitaxy (MBE) system on both diamond and SiO_2\Si substrates, are studied using physical characterization methods and waveguide loss measurements. It is found that significant improvements in the polycrystalline GaP material characteristics are necessary for this to be a viable platform for a hybrid optical network.

A different approach to the integration of GaP with diamond substrates is discussed in

chapter 4. MBE grown single-crystalline GaP layers show promising optical material characteristics. An epitaxial lift-off process is found to be reliable for the transfer of sub-micrometer thick, mm^2-sized GaP sheets onto diamond. Finally, coupling of the near-surface NV emission to an array of GaP resonators is demonstrated, indicating suitability of the epitaxial lift-off process for the integration of GaP devices with the defect centers in diamond.

The design and implementation of waveguide-integrated GaP resonators on a mechanical-grade diamond substrate is presented in chapter 5. The coupling characteristics of μm-sized GaP ring and disk resonator structures are simulated with finite-difference-time-domain (FDTD) methods. Electron beam lithography and dry etch processes are adapted for fabrication of sub-100 nm features on small-scale diamond substrates. The final device structures are characterized by optical transmission measurements, and the device performance is evaluated with regard to potential collection efficiencies of NV^- ZPL photons for a future integration with the defect centers.

In chapter 6, GaP resonators coupled to waveguides and grating structures are utilized for the off-chip collection of NV^- ZPL photons. Tuning of the GaP cavity resonance wavelength onto the NV^- ZPL is demonstrated using a gas condensation technique. The demonstration of successful collection of the NV^- ZPL in a coupled hybrid GaP\diamond resonator-waveguide structure is an essential step toward their future integration into large-scale optical networks for entanglement generation. Finally, current limitations for an integration of the present devices in large-scale entanglement networks are discussed.

Chapter 7 concludes this dissertation with a summary of results and an outlook to the future challenges and opportunities for hybrid GaP\diamond photonic networks integrated with NV^- defects in diamond.

Chapter 2:
Background

The utilization of quantum effects is expected to enable the implementation of computing applications which either have previously been limited by the physical resources of classical computing or are utilizing completely new operating mechanisms and protocols based on these quantum properties. Such applications include the simulation of quantum systems [1], [2], prime factorization of large numbers using Shor's algorithm [3] and fundamentally secure communication [4], [5], [31], optimization speed-up, search algorithms or image recognition [6], [32], and quantum teleportation [33], [34]. Numerous candidates for physical qubits are currently investigated for their use in potential QIP systems. Quantum entanglement, a resource for QIP, has been demonstrated, for example, between atoms trapped in optical cavities [10], [13], electrons in double quantum dot structures [14], and between phase [12] and transmon qubits [11] in superconducting Josephson junctions. For a large number of these potential candidates, limiting factors for future integration into large-scale quantum networks are insufficient coherence times, extreme operating environments, and non-scalable qubit-qubit interactions for quantum gate implementations [8], [9], [35]. The NV center in diamond has the potential to overcome those limitations: it exhibits long electron spin coherence times even at room-temperature, allows for optical initialization, manipulation, and read-out, and has the potential for integration into scalable solid-state QIP platforms.

This chapter introduces basic principles of measurement-based, or one-way, quantum computing, and the requirements it poses on the properties of physical qubits, such as the NV

center in diamond. Recently, free-space entanglement of NV centers has been demonstrated; however, the entanglement process has been characterized by low success probability. Instead, on-chip optical networks may provide a future platform for multi-qubit entanglement generation. Current state-of-the-art photonic devices integrated with NV defects are presented, and the need for integration of linear electro-optic materials for active device capabilities is reviewed.

2.1 Entanglement as resource for measurement-based quantum computing

Entanglement between qubits is a universal resource for measurement-based quantum computing. Qubits are a two-state quantum mechanical system, with the system being present in a superposition of the two states. The qubit states $|\Psi\rangle$, evolving according to the Schrödinger equation, can be described as a linear superposition of two levels $|0\rangle$ and $|1\rangle$:

$$|\Psi\rangle = \alpha|0\rangle + \beta|1\rangle \qquad \text{Eq. 2.1}$$

with $|\alpha|^2$ and $|\beta|^2$ the probability amplitudes for state $|0\rangle$ or $|1\rangle$, respectively:

$$|\alpha|^2 + |\beta|^2 = 1 \qquad \text{Eq. 2.2}$$

QIP systems initially were designed with a quantum circuit architecture resembling classical circuits; two-qubit gate operations were performed on closely spaced qubits. In 2001, measurement-based, or one-way, quantum computing was introduced [7], [36]. In the one-way scheme, numerous distant qubits are entangled and the computational algorithm is implemented by measurement of single qubit states. Via entanglement, measurement causes the new state to be driven to the next qubits, which can then be further manipulated or read out. [8], [9]

Entanglement can occur locally, e.g. due to the exchange interaction of two closely spaced electrons, or it can be created by measurement of two separate physical objects. It is the latter implementation that is most interesting for large-scale entanglement creation between distant qubits. In the following section, each step of a simple measurement-based entanglement scheme

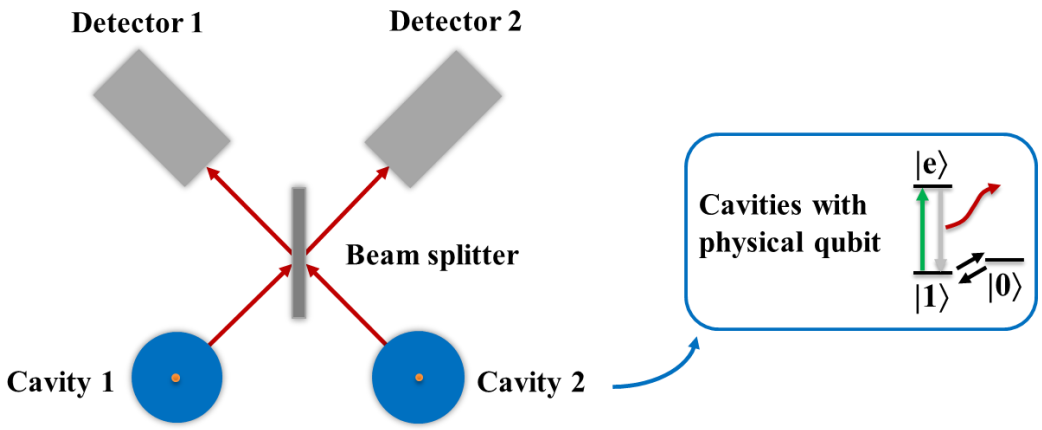

Fig. 2.1.1: Entanglement by measurement. The beam splitter erases the path information of photons emitted from one of the two cavities with a qubit relaxing from its excited state. Detection of a single photon in either detector constitutes entanglement creation between the two quantum systems. Schematic adapted from [9].

is described with the physical requirements it poses on a physical qubit system.

Fig. 2.1.1 displays a schematic for entanglement creation between two distant qubits, located in separate cavities, using a beam splitter for erasure of the photon path information [8], [9]. The cavity enables efficient photon collection from the physical qubit and further routing of the collected photons. Each physical qubit consists of two ground states, which form the logical qubit. Any physical implementation requires a minimum three-level structure with at least one logically qubit optically coupled to the excited state (Fig. 2.1.1, inset).

After initialization and preparation of the respective qubit in the desired superposition state $\frac{1}{\sqrt{2}}(|0\rangle + |1\rangle)$ in each cavity, the transition between $|1\rangle$ and $|e\rangle$ is simultaneously exited in the two three-level systems:

$$\frac{1}{\sqrt{2}}(|0\rangle + |1\rangle) \rightarrow \frac{1}{\sqrt{2}}(|0\rangle + |e\rangle). \qquad \text{Eq. 2.3}$$

The state of the entire system can be described as:

$$\frac{1}{2}(|ee\rangle + |e0\rangle + |0e\rangle + |00\rangle). \qquad \text{Eq. 2.4}$$

Upon decay of the excited state, there are four different possibilities for radiative decay: both qubits emit a photon, the left qubit emits a photon, the right qubits emits a photon, or neither one emits a photon. Assuming 100% photon collection efficiency, we eliminate the cases where zero or two photons are emitted. After the single photon emission, the state of the system can also be expressed as:

$$(|\mathrm{e0}\rangle + |\mathrm{0e}\rangle)|\mathrm{vac}\rangle \rightarrow (|10\rangle\alpha_r^\dagger + (|01\rangle\alpha_l^\dagger)|\mathrm{vac}\rangle \qquad \text{Eq. 2.5}$$

where $\alpha_r^\dagger$ ($\alpha_l^\dagger$) is the photon creation operator in the lower right (left) channel and $|\mathrm{vac}\rangle$ is the electromagnetic vacuum state (i.e. no photons).

The single photon leaving one of the two cavities is routed toward a beam splitter, which either transmits or reflects each photon with equal probability (Fig. 2.1.1). The beam splitter therefore removes the information about which of the qubits emits the single photon *if the emission is coherent and possesses identical emission wavelengths*. It transforms the above photon operators from the input to the output modes in the upper left and right paths, respectively:

$$a_r^\dagger \rightarrow \frac{1}{\sqrt{2}}\left(b_L^\dagger + ib_r^\dagger\right) \quad , \quad a_l^\dagger \rightarrow \frac{1}{\sqrt{2}}\left(ib_L^\dagger + b_r^\dagger\right). \qquad \text{Eq. 2.6}$$

The state of the system after the photons have passed the beam splitter is therefore:

$$\frac{1}{\sqrt{2}}\left((|10\rangle + \mathrm{i}|01\rangle)b_L^\dagger + (i|10\rangle + |01\rangle)b_r^\dagger\right)|\mathrm{vac}\rangle. \qquad \text{Eq. 2.7}$$

The photon is then collected, or read out, by one of the detectors, where it is projected into one of the maximally entangled states $\frac{1}{\sqrt{2}}(|10\rangle + i|01\rangle)$ (left detector) or $\frac{1}{\sqrt{2}}(i|10\rangle + |01\rangle)$ (right detector). Entanglement generation requires that all information that can identify which qubit emitted the photon is erased. Hence, the photons emitted from the two qubits must be spectrally and temporally identical. Furthermore, entanglement lifetime is limited by the logical qubit

coherence time. To create entanglement in a multi-qubit network, all single entanglement steps have to be carried out within the ground state coherence time of the physical qubits. With this scheme, the ability to initialize, manipulate, and optically read-out the logic qubit, as well as long coherence times are critical for successful entanglement generation [9], [35].

The entangled network can be represented by a graph state. The qubits are represented by vertices, and the vertices indicate a controlled phase gate (a similar procedure to the entanglement gate described above) has been performed between the two nodes. Once this graph state is constructed, any quantum computation can be performed by a simple series of single qubit measurements (i.e. determining the state of the qubit) [9]. Of immediate practical significance, protocols exist to build infinitely large graph states even when the success probability of entanglement is finite. Additionally, the graph states can be built simultaneously as a measurement proceeds, lowering the requirement for the number of qubits needed in a quantum computation.

2.2 The nitrogen-vacancy defect center in diamond

One promising qubit system for entanglement generation is the NV^- center in diamond, due to the ability to optically address and read out its spin states and long coherence times even at room temperature [16], [17], [35], [37]–[42]. The NV^- center is a point defect consisting of a substitutional nitrogen atom (N) adjacent to a vacant carbon (C) lattice site in the face-centered cubic diamond crystal (Fig. 2.2.1(a)). The defect center can be incorporated into the diamond lattice in four different orientations: $[111]$, $[1\bar{1}\bar{1}]$, $[\bar{1}\bar{1}1]$, and $[\bar{1}1\bar{1}]$.

Single NV^- color centers in type Ib electron irradiated diamond were first explored by Gruber et al. through room-temperature confocal microscopy and photoluminescence (PL) spectroscopy [15]. Fig. 2.2.1(b) displays a confocal microscopy image of single NV^- defects in diamond.

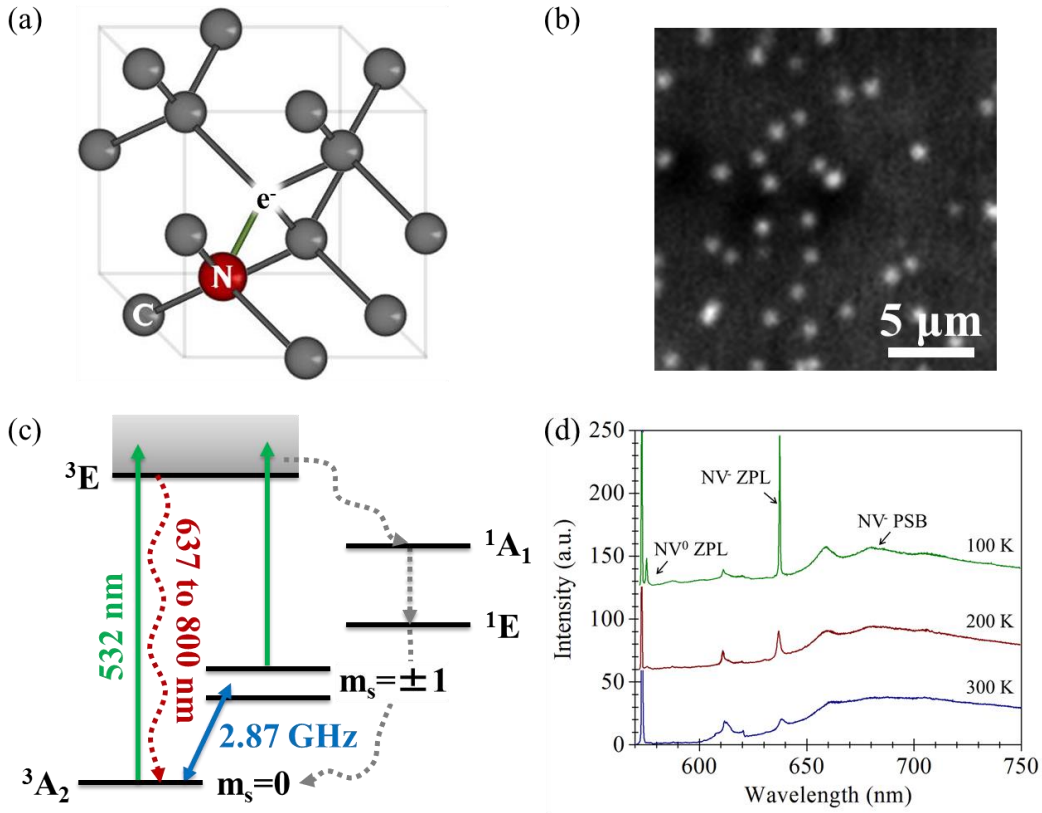

Fig. 2.2.1: The NV^- defect center in diamond. (a) Schematic of the point defect with a substitutional nitrogen atom next to a vacant carbon lattice site and two free electrons. (b) Confocal scan of the diamond surface showing single NV^- centers in a CVD diamond substrate. (c) Schematic energy level diagram with the three different ground state qubit spin levels, and the visible and dark relaxation pathways for the $m_s=0$ and $m_s=\pm1$ levels, respectively. (d) Room-temperature and low-temperature PL spectra of NV^- with the characteristic zero-phonon-line at 637 nm and the phonon sideband at longer wavelengths. [15], [17] Data for (b),(d) taken by author.

Fig. 2.2.1(c) displays a schematic of energy levels of the defect center with $^3A_2$ the ground state, ^3E the excited state, and $^1A_1$ and ^1E intermediate shelving states. The separation between the ground and the excited state is 1.945 eV (637 nm). Strong coupling between the NV^- electrons and phonons in the diamond lattice cause the majority of the spontaneous emission (~ 97%) into the phonon sideband (PSB) and only ~ 3% into the zero-phonon line (ZPL) [43], [44].

The ZPL optical transition is the transition of interest for photon-mediated entanglement. At room temperature, the ZPL is broadened through phonon interactions. These are suppressed at lower temperatures resulting in a narrower ZPL width. These optical characteristics are evident

in the three PL spectra, taken by the author, of NV^- centers between 100 K and 300 K shown in Fig. 2.2.1(d). The spectra show the characteristic ZPL for a pure photon transition at ~ 637 nm and the PSB from phonon-assisted transitions ranging up to ~ 800 nm.

The ground state of the NV center is a two electron spin triplet state with total angular momentum S = 1. The $m_s = 0$ and $m_s = \pm 1$ ground state spin triplets are separated by a 2.87 GHz zero-field splitting. The ground state spins can therefore be manipulated by the application of a microwave field. Typically, the $m_s = 0$ and either the $m_s = -1$ or the $m_s = +1$ levels are utilized as qubit states, while other schemes use the $m_s = -1$ and the $m_s = +1$ levels.

Upon optical excitation, the $m_s = 0$ and $m_s = \pm 1$ spin projections undergo different relaxation pathways. The $m_s = 0$ projection decays predominantly back into the $m_s = 0$ sub-level with the emission of a photon in the visible range. In contrast, defects excited from the $m_s = \pm 1$ levels are more likely to undergo a spin-polarized, non-radiative decay through the intermediate, metastable dark states ($^1A_1$, ^1E) back into the $m_s = 0$ level. NV^- centers can therefore be initialized into the $m_s = 0$ projection by cycling of the optical excitation. The electron state can then be initialized into an arbitrary superposition state by a resonant microwave pulse. Additionally, because fluorescence from the $m_s=0$ state is brighter than the emission from the defect in the $m_s = \pm 1$ state, the spin-state can be read optically.

Of particular interest is the long spin coherence time of the defect, which is 1.8 ms at room temperature for single defects in ultrapure, isotopically purified diamond substrates [41]. Dynamic decoupling techniques can further minimize decoherence effects by isolating the spins from the environment, leading to spin coherence times above 6 ms at room temperature and 0.6 s at 77 K for spin ensembles [45], [46]. The electron qubit state can be transferred to the nuclear state through the electron-nuclear hyperfine interaction. The nuclear spin coherence can persist

up to 1 s at room temperature [47]. The coherence time is the upper limit on the qubit memory time.

NV^- centers can occur naturally during diamond formation, or they can be created artificially in diamond substrates by electron irradiation [48], [49], ion implantation [50]–[54] or incorporation during diamond chemical vapor deposition (CVD) [38], [55], [56]. Ideally, for QIP applications, NV^- defects for should be integrated in pre-defined locations with a specific lattice orientation for optimal coupling of their photons to the optical modes in photonic devices. Furthermore, they should emit stable, spectrally identical photons and maintain long spin coherence times for successful entanglement creation.

Engineering of NV^- characteristics by modifications of diamond growth or implantation processes, engineering of diamond host substrates, as well as external control of the NV^- properties is an active area of research. Nitrogen implantation through nanoscale apertures on the diamond substrates, for example, results in the fabrication of regular "NV^- patterns" in the substrate [50]. Implantation processes and nitrogen doping during diamond CVD growth further enable engineering of the final NV^- depth in the diamond substrate. Recently, 3-dimensional control over the spatial NV^- location in the diamond lattice (localized to a volume of ~ $(180\ nm)^3$) has been achieved by a combination of N delta-doping during CVD diamond growth and subsequent patterned C implantation [56]. Furthermore, the preferential alignment of NV^- defects along selected orientations in the diamond lattice can be controlled during diamond CVD growth [38], [57].

In addition to control over the position and orientation, it is necessary to control the NV center emission frequency. Two different NV centers typically do not emit photons at the same frequency. This inhomogeneous broadening of the ZPL center wavelength is due to microscale

static variations of strain and electric fields in the diamond host lattice (e.g. due to defects). This static variation can be overcome by applying electric fields to Stark-shift the ZPL center wavelength. This techniques has been successfully employed to entangle two distant NV^- centers [18], [58], [59]. Of greater difficulty is spectral diffusion, i.e. time-dependent variations in the ZPL center wavelength due to interactions with impurities in the diamond host material. Dynamic stabilization of the emission of a natural NV^- defect has been achieved by Stark tuning within a feedback system. However, dynamic stabilization of the NV^- ZPL has yet to be integrated with photonic devices.

2.3 Entanglement creation between NV^- defect centers in diamond

Different schemes for the entanglement of NV^- center pairs have recently been explored as a first step toward the realization of large-scale NV^- qubit networks. Strong coupling to the ground state magnetic dipole moment of closely spaced NV^- defects in bulk diamond [60] as well as measurement-based entanglement of distant NV^- center electron spins [18] are presented here as examples of state-of-the-art schemes for entanglement generation.

Coherent magnetic dipolar coupling between the ground state electron spins of two defects separated by ~ 25 nm was utilized to mediate interactions between their respective nuclear spins for room-temperature entanglement creation with a fidelity of 0.67 [60], [61]. This entanglement scheme relies on spatial proximity between the physical qubits, and addressability of each individual NV^- center with a characteristic microwave frequency. Hence, this approach appears limited for entanglement generation between large numbers of interacting NV^- defects.

Entanglement of distant NV^- defects has been demonstrated utilizing a measurement-based approach similar to the one discussed in section 2.1, in which an optical beam splitter is used to erase the which-path information for photons emitted from defects in two separate diamond

substrates [18]. Fig. 2.3.1 displays a schematic of the entanglement generation setup. Several technologies are employed for enhancement of the NV^- photon collection efficiencies and tuning of the emission wavelength: the NV^- defects are located in solid immersion lenses (SILs) for enhanced out-coupling of the NV^- emission from the diamond substrate [62], [63]. Electrodes and microwave strip lines surrounding the defects are used for Stark tuning of the NV^- emission toward identical wavelengths, and manipulation of the NV^- electron spin state, respectively. The quantum information is encoded in the $m_s = 0$ and $m_s = -1$ ground state levels, with the PSB used for read-out of the NV^- spin state [64]. Decoupling techniques are employed for enhancement of the spin coherence time. Local spin-photon entanglement is achieved through spontaneous emission after laser excitation of the NV^- ground states prepared in the electron spin superposition state. A spin-flip technique is employed to test for successful single photon

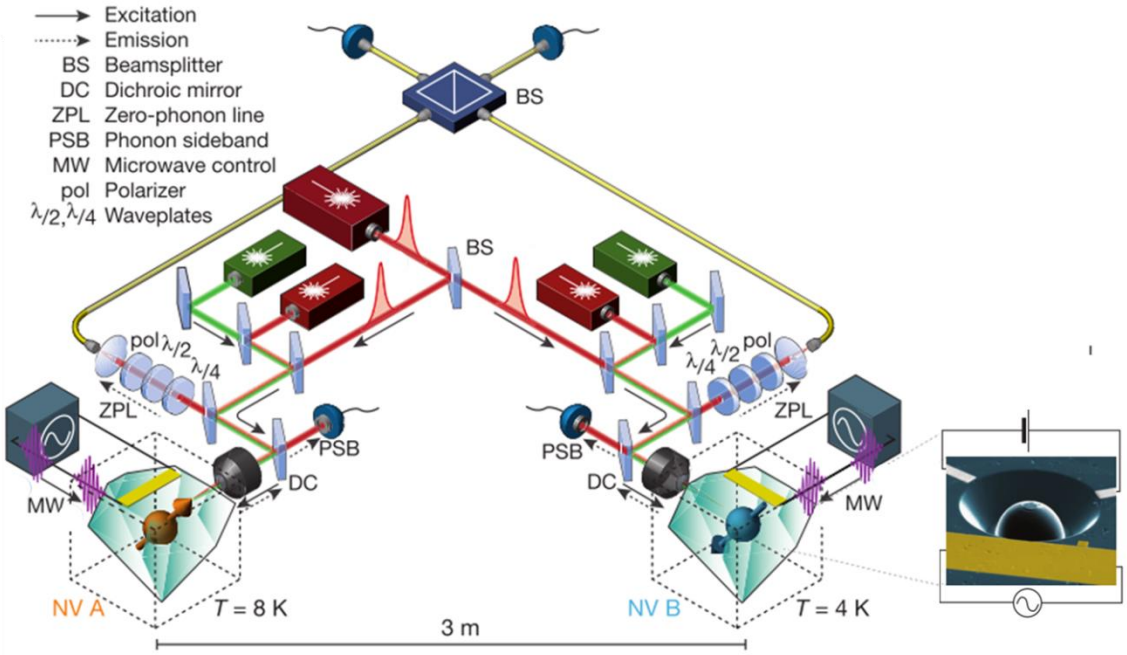

Fig. 2.3.1: Measurement-based entanglement generation between two NV^- electron spins separated by three meters. [18], [59] (a) Schematic of the measurement setup with the beam splitter and detectors for the entanglement creation of ZPL photons in blue. NV^-s are embedded in solid immersion lenses for enhanced out-coupling of the PL from the diamond substrate into free space, and their optical transitions are d.c. Stark-tuned onto resonance. (b) Measured spin-spin correlations verify entanglement between both qubits. Figure from [18].

creation between both NV^-, and enhances the coherence properties of the system. The resonant ZPL photons are overlapped on a beam splitter and detected in the output ports, creating physical entanglement.

While free-space entanglement generation between distant NV^- electron spins is a crucial step toward the realization of future QIP platforms, current entanglement success rates do not allow for scaling toward multi-qubit networks. Successful entanglement could only be achieved once every 10 min. This currently limits scaling of this entanglement scheme to more than 2 physical qubits. Ideally, entanglement creation can be achieved within the coherence times of the respective qubits to allow for multi-qubit operations [8], [9], [35]. The major obstacles toward achieving this goal in the free-space system are limited emission into the ZPL, low collection efficiencies of the photons from the diamond substrate even with the SILs and spectral diffusion of the NV^- ZPL.

Thus, enhancement of the photon collection efficiencies and an increased emission into the NV^- ZPL will be crucial for the implementation of large-scale qubit networks. Optical micro-cavities can be utilized for both enhancement of emission rates into desired resonance modes as well as collection and routing of photons toward on-chip bus waveguides. Solid-state optical networks can integrate on-chip initialization and spin manipulation, Stark tuning of the ZPL transition, effective photon collection and on-chip routing as well as entanglement functionalities.

2.4 Integrated optical cavities for efficient collection and enhancement of NV^- ZPL emission

Different integrated optical device geometries can be utilized to enhance the collection efficiency of NV^- ZPL photons from the diamond substrate. Non-resonant structures, such as SILs [62], [63] or diamond nanowires [65], rely on overcoming the total internal reflection at the

diamond\air interface. In contrast, resonant micro-cavity structures offer the additional advantage of enhancement of the NV^- ZPL line by the Purcell effect [19], [20], [66], which actually increases the percentage of the NV^- emission into the ZPL.

Integrated optical micro-cavities with different geometries, such as integrated Bragg reflectors, photonic crystal cavities (PhCs) or dielectric disk, ring or toroid resonators, have gained significant interest for numerous applications in lasing, quantum optics, optical communications, or sensing [67]–[70]. Whispering-gallery-mode disk and ring resonators are of particular interest for QIP applications since they can be realized with high quality factors and small mode volumes for a potential large Purcell enhancement of the desired NV^- ZPL. Furthermore, they can be coupled to on-chip waveguides for efficient photon collection and routing.

2.4.1 Whispering-gallery-mode resonators

High index, dielectric optical micrometer-sized resonator structures, such as disks, rings, or spheres, can confine electromagnetic fields to small volumes due to total internal reflection of light at the boundaries of the structures with a high refractive index, surrounded by a low-index material. These modes are commonly imagined as closed-ray surface trajectories, confined and focused by continuous reflection at the curved surfaces. Fig. 2.4.1 (a) illustrates the ray paths in a micro-disk resonator with a refractive index n_1 larger than the refractive index n_2 of the surrounding material. The arising circular resonance modes are called whispering-gallery-modes. For dielectric disk resonators with a radius r much greater than the wavelength of interest λ, the following resonance condition for constructive interference of the confined field exists:

$$m\frac{\lambda_{res}}{n_{eff}} = 2\pi r_{eff} \qquad \text{Eq. 2.8}$$

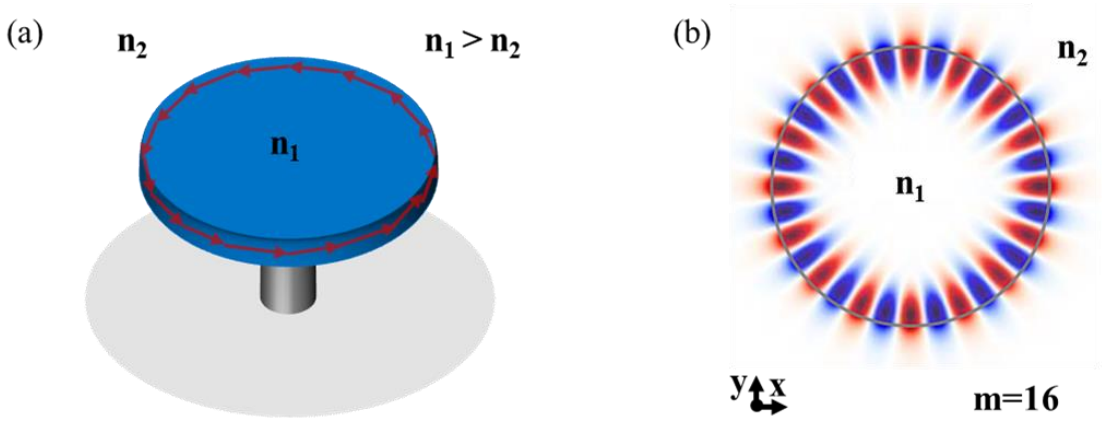

Fig. 2.4.1: Whispering-gallery-mode resonators. (a) Schematic of rays reflected and refocused at curved interface between high-index disk resonator and low-index environment under resonance conditions. (b) Quasi-TM mode in a corresponding disk resonator (grey outline), m=16, top view.

where m is the angular mode number, λ_{res} the vacuum resonance wavelength, n_{eff} the effective refractive index, and r_{eff} the effective radius of the whispering-gallery-mode.

The optical modes in such a resonance structure can be calculated from Helmholtz equations. The ray optics picture is intuitively appealing but is not accurate for devices with sizes on the order of the wavelength. For these devices, a full electromagnetic simulation must be performed to determine the mode characteristics. Transverse magnetic (TM) modes possess an electric field parallel to the sidewall of a disk or ring resonator, or parallel to a spherical surface. In contrast, transverse electric (TE) modes exhibit an electric field component in the radial direction of the cavity structures. Fig. 2.4.1(b) displays the radial electric field distribution of a high index-disk resonator with a fundamental quasi-TM mode (radial mode number n=1) with an azimuthal mode number m=16.

The resonance spectrum of a micro-cavity is size-dependent. Several parameters characterize the resonance spectrum of an optical resonator. The free spectral range (*FSR*) is defined as:

$$FSR = \lambda_{res,m+1} - \lambda_{res,m} = \Delta\lambda_{res} \approx \frac{{\lambda_{res,m}}^2}{2\pi r n_{eff}} \quad \text{Eq. 2.9}$$

with $\lambda_{res,m}$ and $\lambda_{res,m+1}$ neighboring resonance modes. The resonance mode is given by Eq. 2.8 in which n_{eff} is the effective refractive index (taking into account that the mode is not completely confined to the cavity).

An ideal optical cavity is lossless and can retain light forever. For real devices, the loss properties of a resonator are characterized by the quality factor Q:

$$Q = 2\pi \frac{Energy\ stored}{Energy\ lost/Optical\ cycle} \quad \text{Eq. 2.10}$$

The overall quality factor of a cavity is limited by the intrinsic absorption in the dielectric material ($Q_{material}$), absorption at the cavity surface, e.g. due to an absorbent interface or adsorbed layers ($Q_{surface}$), scattering losses ($Q_{scatter}$), and bending loss in cavities with a small radius of curvature (Q_{bend}) [71]:

$$\frac{1}{Q} = \frac{1}{Q_{material}} + \frac{1}{Q_{surface}} + \frac{1}{Q_{scatter}} + \frac{1}{Q_{bend}} \quad \text{Eq. 2.11}$$

The quality factor is also a measure of the cavity decay rate γ, i.e. the rate for the cavity field intensity to decay to the environment by e:

$$Q = \pi \frac{\vartheta_{res}}{\gamma} \quad \text{Eq. 2.12}$$

where υ_{res} is the cavity resonance frequency and c is the speed of light. The resonator Q may be limited further by coupling to an external mode, e.g. in a bus waveguide for routing of the photons between cavities. In practice, the quality factor can be determined experimentally by measurement of the resonance wavelength and the corresponding linewidth (full width at half maximum of the resonance peak – $\Delta\lambda_{FWHM}$):

$$Q = \frac{\lambda_{res}}{\Delta\lambda_{FWHM}} \qquad \text{Eq. 2.13}$$

Another characteristic feature of the resonance mode of a micro-cavity is its mode volume *V*, which is defined as the ratio of the energy stored in this mode vs. the maximum energy density in the mode [72]:

$$V = \frac{Energy\ stored}{Maximum\ energy\ density} \qquad \text{Eq. 2.14}$$

From the spatial distribution of the electric field, the mode volume can be calculated by:

$$V = \frac{\int_V \varepsilon(\boldsymbol{r})|\boldsymbol{E}(\boldsymbol{r})|^2\, d^3\boldsymbol{r}}{max[\varepsilon(\boldsymbol{r})|\boldsymbol{E}(\boldsymbol{r})|^2]} \qquad \text{Eq. 2.15}$$

where $\varepsilon(\boldsymbol{r})=\varepsilon_0\varepsilon_r(\boldsymbol{r})$ is the electric permittivity and $\boldsymbol{E(r)}$ the electric field at point $\boldsymbol{r}$. ε_0 and $\varepsilon_r(\boldsymbol{r})$ are the vacuum permittivity and relative permittivity at $\boldsymbol{r}$, respectively.

2.4.2 Purcell effect in integrated optical cavities

To increase the number of indistinguishable photons for entanglement creation, the photon emission rate of the NV^- center can be engineered by the field of a resonant optical micro-cavity due to the Purcell effect (Fig. 2.4.2) [19], [73]. If a single-photon source is placed in a resonator, its interaction with the cavity field can be described by the coupling rate g between the cavity and the emitter, the spontaneous emission rate $\gamma_{spontaneous}$ and the cavity decay rate γ. In the weak coupling regime, $g^2 > \gamma \cdot \gamma_{spontaneous,}$ the Purcell factor F_P characterizes the enhancement of the spontaneous photon emission rate.

The spontaneous emission rate of photons is proportional to the density of states *N*. In free space, this density scales quadratically in frequency ω:

$$N(\omega) \propto \frac{2\omega^2}{\pi c^3} \qquad \text{Eq. 2.16}$$

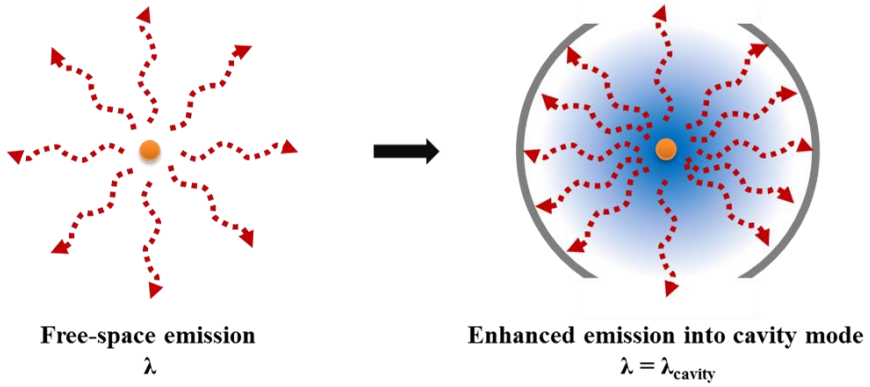

Fig. 2.4.2: Purcell enhancement of the photon emission rates of single-photon emitters confined in a micro-cavity structure (grey outline) under weak coupling conditions.

where *c* is the speed of light. In contrast, the density of states in a cavity scales linearly with the cavity quality factor, and is inversely proportional to the size of the cavity:

$$N(\omega_0) \propto \frac{2\pi}{\Delta\omega V} = \frac{2\pi Q}{\omega_0 V} \qquad \text{Eq. 2.17}$$

High *Q*, small *V* cavities show a significantly enhanced density of photon states at resonance. Hence, the spontaneous emission rate of a photon source can be tuned by the parameters of the cavity field. The Purcell factor quantifies the enhancement of the spontaneous emission rates in a cavity field versus the free-space emission rate:

$$F_P \propto \frac{\pi^2 c^3 Q}{\omega^3 V} \propto \frac{3\lambda^3}{4\pi^2}\frac{Q}{V} \qquad \text{Eq. 2.18}$$

The Purcell factor for an emitter in a dielectric cavity with index of refraction *n* - with optimal spatial location and polarization with respect to the cavity electric field – is given by:

$$F_P = \frac{3}{4\pi^2}\left(\frac{\lambda}{n}\right)^3 \frac{Q}{V} \qquad \text{Eq. 2.19}$$

2.5 On-chip integration of NV^- centers with optical resonators

The integration of NV^- centers with optical resonators can not only enhance the collection efficiencies of the ZPL photons but also enable evanescent coupling of the emission to bus

waveguides for interconnection with a large-scale NV^- network. These networks, however, will not only rely on cavity structures for photon collection but also active optical switches for the implementation of quantum entanglement between pre-selected NV^- qubit nodes. Ideally, these modulators are formed by integrated linear electro-optic (EO) resonator devices with a compact and efficient, simplistic design for facile fabrication.

2.5.1 Purcell enhancement and off-chip coupling of the NV^- ZPL in integrated all-diamond networks

Different resonator geometries have been explored for the integration with NV^- centers in bulk diamond as well as with diamond nano-crystals, such as disk and ring resonators or photonic crystal cavities (PhCs) [20]–[22], [66], [74], [75]. Typically, NV^- centers in bulk diamond exhibit superior properties to defects in diamond crystals.

In these devices, Eq. 2.19 has to be modified to account for the location and spatial orientation of the NV^- dipole with regard to the cavity field:

$$F_P = \frac{3}{4\pi^2}\left(\frac{\lambda}{n}\right)^3 \frac{Q}{V}\left(\frac{|\hat{\mu}\cdot \boldsymbol{E}_{NV}|}{|\boldsymbol{E}_{max}|}\right)^2 \qquad \text{Eq. 2.20}$$

Resonators with small mode volumes, such as PhCs, offer the highest theoretical Purcell factors. One-dimensional diamond nano-beams fabricated from single-crystalline diamond membranes with naturally occurring NV^- show a quality factor of 6,000 [75]. With a small mode volume of ~ $3.7(\frac{\lambda}{n})^3$ (Fig. 2.5.1 (b)), the theoretically expected enhancement is ~ 34. A maximum enhancement of only ~ 7 was measured, likely due to the non-ideal NV^- placement and orientation. A Purcell factor of ~ 70 was achieved for 2-dimensional mono-crystalline PhCs (Fig. 2.5.1(c)) [66] with mode volumes < 1 $(\frac{\lambda}{n})^3$.

Ring resonators are an alternative cavity geometry for engineering Purcell enhancements. Although mode volumes are larger than in PhCs, they are more readily integrated with

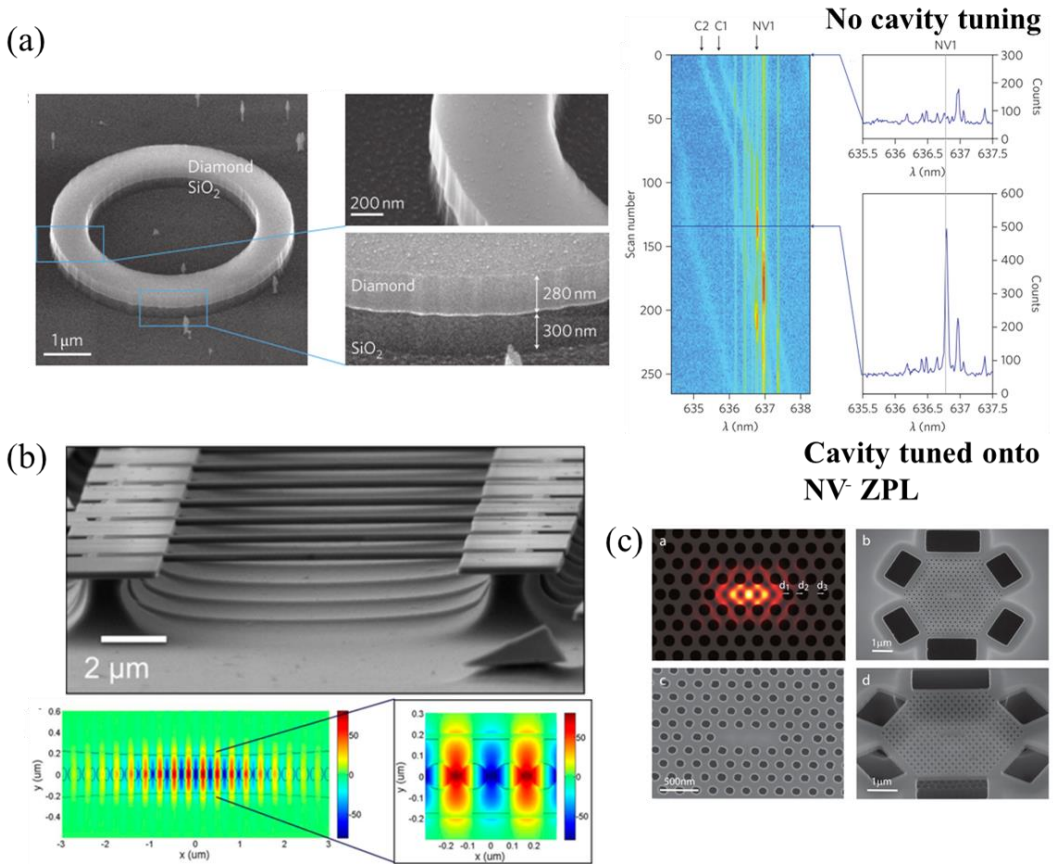

Fig. 2.5.1: Purcell enhancement of the NV^- ZPL in diamond micro-cavity structures. [20], [23], [66], [74], [75] (a) Diamond ring resonator on SiO_2. The cavity resonance mode is tuned onto the NV^- ZPL wavelength by condensation of xenon gas onto the sample. A Purcell factor > 10 is achieved. Figures from [20]. (b) A Purcell enhancement of ~ 7 is accomplished for NV^- centers embedded in 1-D tapered diamond nanobeams. Figures from [75]. (c) The emission rates of NV^- embedded in single-crystalline diamond PhCs is enhanced by a factor of ~ 70. Figure from [66].

waveguides and thus more suitable for large-scale optical networks. Fig. 2.5.1(a) shows a 4.8 µm diameter, 700 nm wide diamond ring resonator on silicon dioxide (SiO_2) fabricated from a 280 nm thick single-crystalline diamond membrane [20]. NV^- centers were incorporated during diamond growth. Maximum *Q*-factors of ~ 5,000 with mode volumes of ~ $17(\frac{\lambda}{n})^3$ to ~ $32(\frac{\lambda}{n})^3$ were achieved. Single NV^- centers in this resonator could be coupled to the resonance mode, and the ZPL emission was selectively enhanced by a factor F_P ~ 10, very close to the theoretical maximum. Off-chip coupling of the NV^- ZPL emission using all-diamond resonator-waveguide

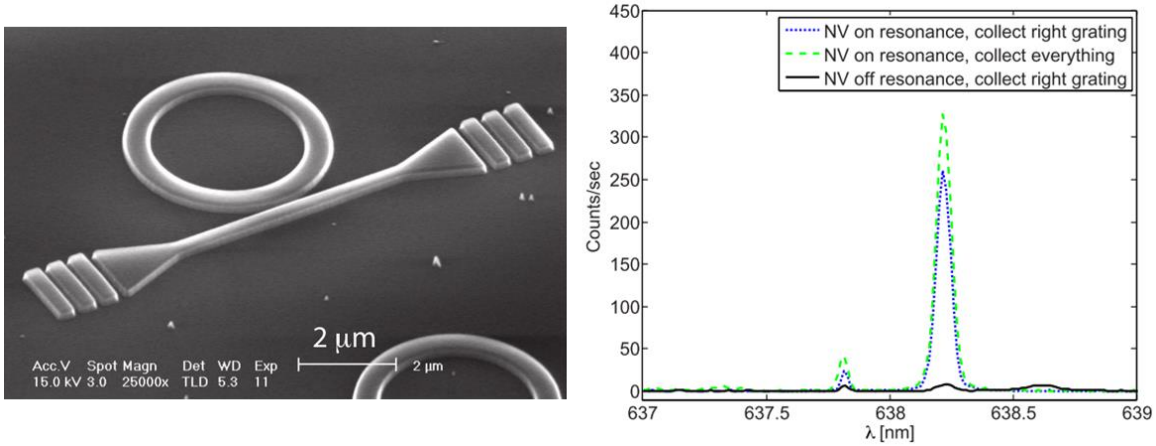

Fig. 2.5.2: Off-chip coupling of the NV^- center emission using all-diamond waveguide-integrated resonator structures. [21]–[23], [76] Disk or ring resonators are evanescently coupled to bus waveguide. The cavity modes can be tuned onto the NV^- ZPL and coupled off-chip with out-of-plane grating couplers. Figures from [22].

systems integrated with off-chip grating couplers has recently been demonstrated (Fig. 2.5.2) [21], [66].

All-diamond networks potentially offer high photon collection efficiencies due to small device dimensions and the defect center located close to the cavity field maximum. However, the development of active optical devices for switching capabilities in an all-optical diamond photonic network has been hindered by its material properties [25]. Thermal diamond switches based on the shift of the diamond refractive index with temperature [24] are inherently slow and affect the inhomogeneous broadening of NV^- centers in their vicinity.

2.5.2 Linear electro-optic tuning in integrated resonator structures

The implementation of active devices is one of the primary motivations for the integration of GaP optical devices with NV^- defect centers in diamond. Although experimental work was not done on such device structures, the linear EO properties of GaP lend themselves to the realization of optical switches similar to what have been achieved with other EO materials such as aluminum nitride (AlN).

Crystals in an applied electric field experience a redistribution of the bond charges between their atoms, concurrent with a slight deformation of the lattice. These changes are anisotropic; hence, the dielectric properties of the material change differently for various directions in the crystals. The change in the refractive index as function of the field *E* applied in direction *j* is:

$$\Delta\left(\frac{1}{n^2}\right)_i = \sum_j r_{ij}\, E_j \qquad \text{Eq. 2.21}$$

with i = 1, …, 6 and j = x, y, z = 1, 2, 3. r_{ij} described the *ij*th element of the linear EO tensor.

Crystalline materials without an inversion symmetry center exhibit a linear EO or Pockels effect. In contrast to silicon or diamond, binary compound semiconductors such as AlN or GaP lack inversion symmetry, and therefore possess linear EO properties.

Sputter-deposited AlN has recently been investigated as linear EO material for fast resonance tuning in silicon photonics [28], [77], [78]. Fig. 2.5.3 shows a schematic of the AlN crystal

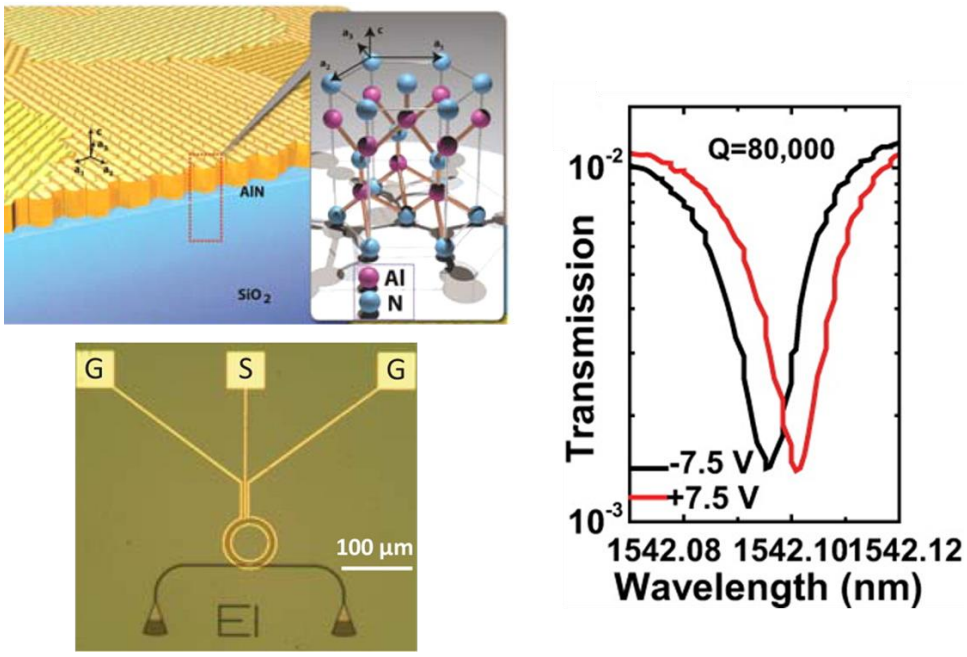

Fig. 2.5.3: Linear electro-optic modulators based on Pockels effect in AlN. [28], [77], [78] The resonance wavelength can be tuned with the application of an electric field. Figures from [28].

structure with one symmetry axis perpendicular to the surface of the film. AlN micro-ring resonators were fabricated on a SiO_2 substrate integrated with planar electrodes on top and adjacent to the devices for application of an out-of-plane electric field component for maximum exploitation of the linear EO coefficient $\chi^{(2)}$. With a DC bias applied, the resonance condition of the device changes due to the change in refractive index. The transmission spectrum in Fig. 2.5.3 displays the resonance dips for two different bias conditions, with a clear shift in the resonance wavelength.

This work is promising for the feasibility of utilizing an EO system in diamond. AlN has a large bandgap of 6.2 eV, and thereby a large transparency window ranging from the ultraviolet to infrared, and shows low propagation loss. Its low refractive index of 2.1, however, does not allow for waveguiding in the material if integrated with a diamond substrate (refractive index of diamond at 637 nm ~ 2.4). This motivates the study of GaP as a linear EO material with a high refractive index for efficient light confinement on a diamond substrate.

2.5.3 Integration of GaP devices with diamond

GaP has a high refractive index of 3.31 at 637 nm (1.945 eV) (Fig. 2.5.4(c)) and an indirect bandgap of 2.26 eV (Fig. 2.5.4(b)) [26], [27]; hence, it is transparent for the wavelength range of interest and can be used as a waveguiding layer on top of diamond. In addition, it is a linear electro-optic material with an EO coefficient $\chi^{(2)} \sim -0.97 \cdot 10^{-12}$ m/V [26], making it a prime candidate for the integration with diamond substrates for the realization of hybrid GaP\diamond networks with active device capabilities.

GaP crystallizes in the zinc blende structure (Fig. 2.5.4(a)); it is a cubic crystal with of point group $\bar{4}3m$, and therefore only exhibits one EO component, r_{41}:

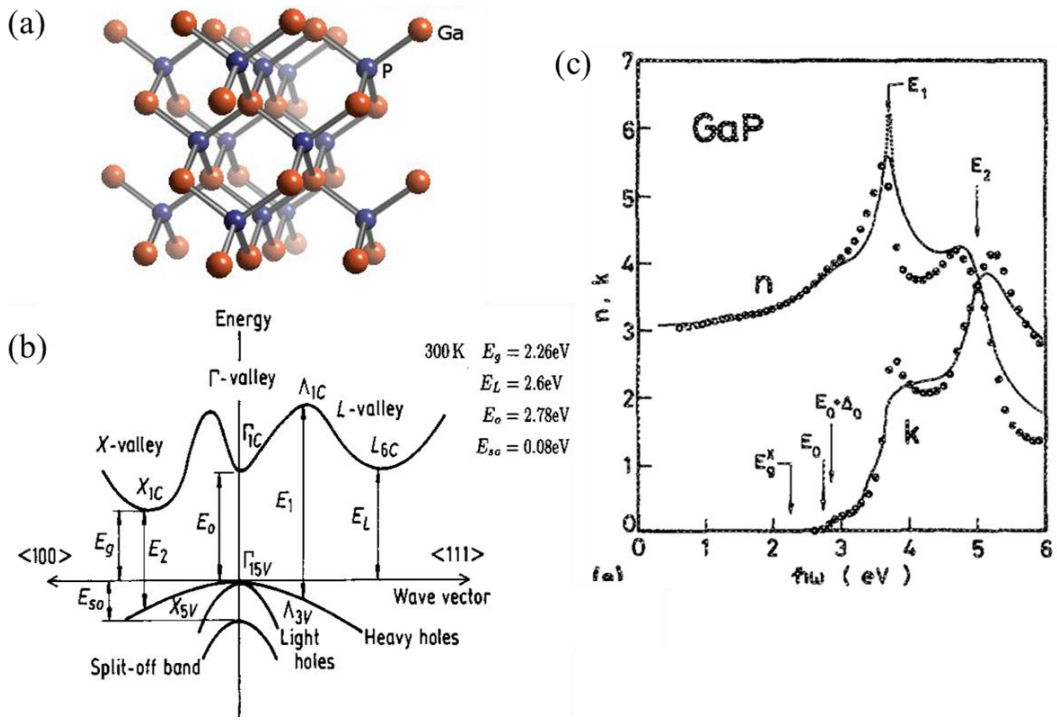

Fig. 2.5.4: GaP electronic and optical properties [26], [27], [79], [80]. (a) Schematic of the zinc blende structure of single-crystalline GaP. Figure from [81]. (b) Band structure of the indirect semiconductor [80]. (c) Refractive index and extinction coefficients. GaP has a refractive index of ~ 3.31 at 637 nm (1.95 eV), and is transparent at this wavelength. [27] Figure from [79].

$$\Delta\left(\frac{1}{n^2}\right)_i = \begin{pmatrix} 0 & 0 & 0 \\ 0 & 0 & 0 \\ 0 & 0 & 0 \\ r_{41} & 0 & 0 \\ 0 & r_{41} & 0 \\ 0 & 0 & r_{41} \end{pmatrix} \begin{pmatrix} E_x \\ E_y \\ E_z \end{pmatrix} \qquad \text{Eq. 2.22}$$

Hence, the change in the refractive index will mainly depend on the orientation of the applied electric field in hybrid GaP\diamond device structures. Maximum index changes can be expected for the applied bias and optical field both aligned in the <111> direction [26].

Significant progress has been made in proof-of-principle demonstrations of GaP optical devices integrated with diamond NV centers. Single GaP cavity structures, ring and disk resonators as well as PhCs, have been integrated with near-surface NV^- centers in bulk diamond and diamond nano-crystals [30], [82]–[85]. However, the fabrication approaches utilized –

probabilistic release of pre-fabricated resonator structures or manual positioning of single devices with respect to the location of single NV^- centers for optimal coupling – will not allow for the realization of large-scale networks for NV^- entanglement generation.

Fig. 2.5.5 shows GaP ring resonators (Fig. 2.5.5(a)) on a diamond substrate [30] and GaP PhCs (Fig. 2.5.5(b)) on a glass substrate prepared with diamond nanoparticles containing NV^- defects [84]. The GaP ring resonators were fabricated on a secondary substrate before transfer to the diamond [29], [30]: The devices are released from an GaP\AlGaP\GaP substrate by selective etching of the AlGaP layer in HF. The resonators either fall onto the diamond where they stick via van der Waals forces or onto the GaP substrate. Hence, placement of the GaP resonators on the diamond substrate is highly probabilistic. The 900 nm diameter GaP ring exhibits a *Q*-factor of ~ 6,800. The cavity field interacts evanescently with near-surface NV^- centers created via ion implantation and annealing in an electronic-grade diamond substrate. Lifetime measurements were employed to determine the enhancement of the spontaneous emission rate. A Purcell factor of ~ 6 was measured.

The GaP PhCs were transferred from a similar GaP\AlGaP\GaP substrate, where they were

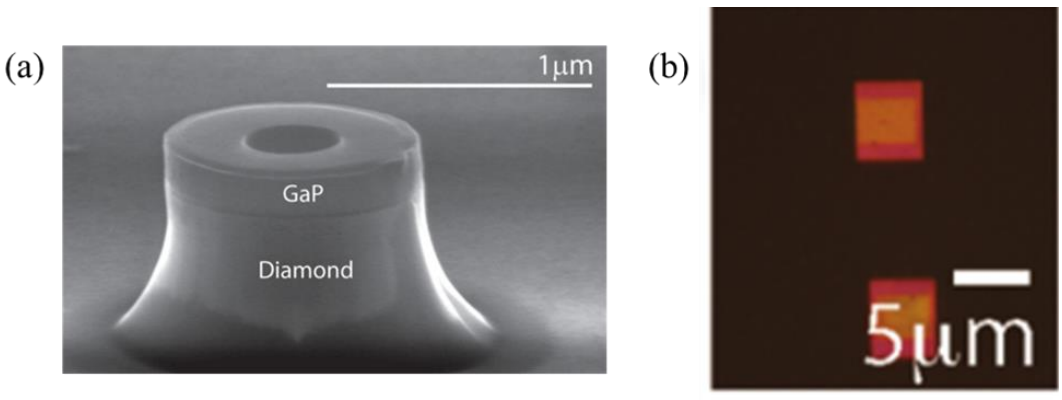

Fig. 2.5.5: GaP resonators integrated with NV^- centers in diamond [29], [30], [82], [84], [85]. (a) A GaP ring resonator on diamond. The resonators are pre-fabricated on an epitaxially grown GaP\AlGaP\GaP substrate, and released onto the diamond from HF solution. Figures from [20]. (b) Optical micrograph of GaP PhCs transferred onto glass substrate with diamond nano-crystals by PDMS stamping. Figure from [84].

defined via electron beam lithography and dry etching of the GaP layer. After selective removal of the AlGaP layer, the free-standing GaP PhCs membranes were picked up with a polydimethylsiloxane (PDMS) stamp, and transferred to a glass slide on which diamond nanoparticles were dispersed. Positioning of the PhCs relative to a single NV^- center is achieved by scanning them across the substrate to find the optimal position for maximum ZPL coupling. [84]

The integration of near-surface NV^- defects in diamond with single GaP resonant cavities and Purcell enhancement of the ZPL emission proves an important step toward large-scale hybrid GaP\diamond networks. However, it is not practical to manually align the components to implement a multi-qubit network. The probabilistic release of pre-fabricated structures onto the diamond substrate, on the other hand, neither provides for the integration of the micro-cavities with bus waveguides nor placement accuracy for efficient collection of the NV^- emission.

Integrated, large-scale optical networks for the entanglement of NV^- electron spins will depend on the efficient collection and enhancement of the NV^- ZPL in resonant cavities, coupling of selected qubits to bus waveguides for on-chip routing using EO switches, interference in integrated optical couplers and on-chip detection for entanglement by measurement, for example, with waveguide-integrated superconducting single photon detectors [86], [87]. A promising platform for realizing such networks is the hybrid GaP\diamond material system. Purcell enhancement of the NV^- ZPL in single hybrid GaP\diamond cavities has been demonstrated. However, other essential technologies have yet to be realized. The first critical step toward the implementation of future photonic networks with active device capabilities is the integration of a linear EO material with waveguiding capabilities on the diamond substrate for

the demonstration of coupled hybrid optical device structures for on-chip routing of the NV^- optical emission.

Chapter 3:
Exploration of nano-crystalline GaP for diamond photonic device applications

A straight-forward but hitherto unexplored approach toward the integration of coupled GaP photonic device structures with NV^- centers in diamond is the deposition of the waveguiding layer directly on the substrate containing the optical defects. GaP sputtering [88]–[90], metal-organic chemical vapor deposition [91], [92] and epitaxial deposition [92]–[94] have been demonstrated for applications such as light-emitting diodes (LEDs) [95], [96], photovoltaics [92], [97], and III-V electronic and optoelectronic devices on silicon (Si) [98]–[100].

Single-crystalline GaP, grown via molecular beam epitaxy (MBE), has been successfully employed for high-*Q* photonic devices, such as disk and ring resonators [29], [30] as well as photonic crystal cavities [83], [84], [101]. GaP layers deposited on diamond in an MBE system, however, are expected to exhibit either an amorphous or polycrystalline morphology due to the significantly different lattice constants of the two materials ($a_{0,GaP}$=5.45 Å and $a_{0,diamond}$=3.57 Å at room temperature). The deposition of gallium arsenide (GaAs) on polycrystalline diamond at reduced temperatures was shown to result in smooth, polycrystalline layers [102]. Motivated by these results, GaP layers are deposited on diamond samples with near-surface NV^- defects at a temperature of ~ 250°C from solid phosphorous (P_2) and gallium (Ga) sources (the GaP depositions are carried out by Y. Song and M. L. Lee at Yale University, CT).

The integration of NV^- defect centers with a hybrid GaP\diamond optical network requires high-quality GaP layers for large resonator quality factors, and good coupling of the NV^- emission into the waveguiding layer. Hence, the as-deposited material is evaluated for optical

loss as well as the potential for collection of the NV^- emission from the diamond substrate. Significant optical losses are observed, and the loss mechanisms are further investigated by studying GaP deposited on more readily available SiO_2 layers.

3.1 Preparation of near-surface NV^- centers via ion implantation and a two-step anneal

The GaP layers studied in the following section are deposited on electronic-grade diamond substrates grown by chemical vapor deposition (CVD) (ElementSix, < 5 ppb N) and high-pressure high-temperature (HPHT) diamond substrates (Sumitomo, 30 – 100 ppm N), in which NV^- centers are created using ion implantation and annealing processes. The implantation and annealing processes provide an easy and reliable means for NV^- creation.

Fig. 3.1.1(a) illustrates the procedure for the creation of near-surface NV^- defects in the diamond lattice. The implantation of $^{14}N^+$ ions with energies of either 10 kV or 50 kV for the CVD and HPHT substrates, respectively, provides the substrate with N^+ ions (CVD diamond) and creates vacancies (CVD and HPHT diamond). A subsequent high-temperature (850°C) annealing process in a hydrogen (H_2) / argon (Ar) atmosphere allows the interstitial nitrogen atoms to move onto carbon lattice sites, and the vacancies to diffuse toward the N to form neutral

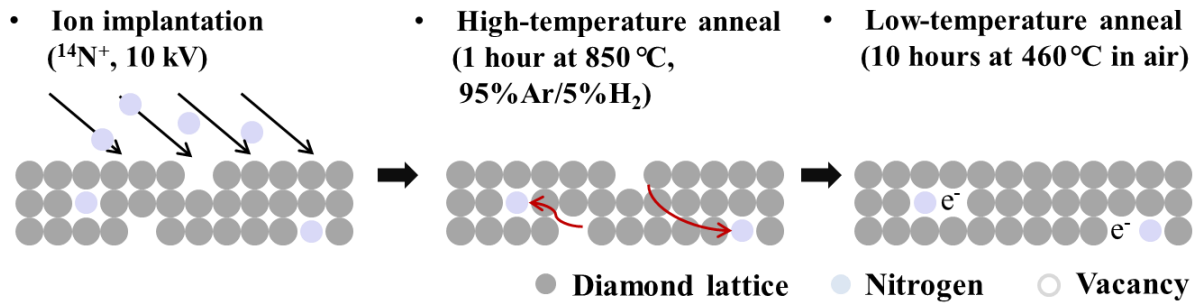

Fig. 3.1.1: Creation of near-surface NV^- centers in diamond. The optical defects are introduced into the diamond lattice by a low-energy implantation of N^+ ions, and a two-step annealing process. The high-temperature anneal allows for the diffusion of vacancies toward substitutional N^+ created during the implantation process. Neutral NV centers are converted to the negative charge state in the subsequent air anneal. Typical conversion efficiencies are 3% to 10% [103]–[105].

nitrogen-vacancy centers (NV^0). A low-temperature (465°C) annealing step in air enables conversion of these neutral defects into the negatively charged state [104], [105].

3.2 Molecular beam deposited GaP on diamond

GaP layers with a target thickness of 250 nm are grown directly on CVD and HPHT diamond substrates prepared with near-surface NV^- centers at reduced temperature to aim for minimum surface roughness [102]. Fig. 3.2.1(a) displays scanning electron micrographs (SEM) of the top and the side of the GaP layer on diamond. The film appears polycrystalline with crystal diameters of ~ 50 to 100 nm. The surface roughness of the material is determined mainly by the height of the single crystals. Atomic force microscopy (AFM) measurements on the GaP films on HPHT diamond indicate a root-mean-square (RMS) surface roughness of ~ 4.0 nm, with a diamond substrate RMS roughness of ~ 0.6 nm. GaP deposited on the CVD diamond shows similar properties (2.8 nm RMS roughness).

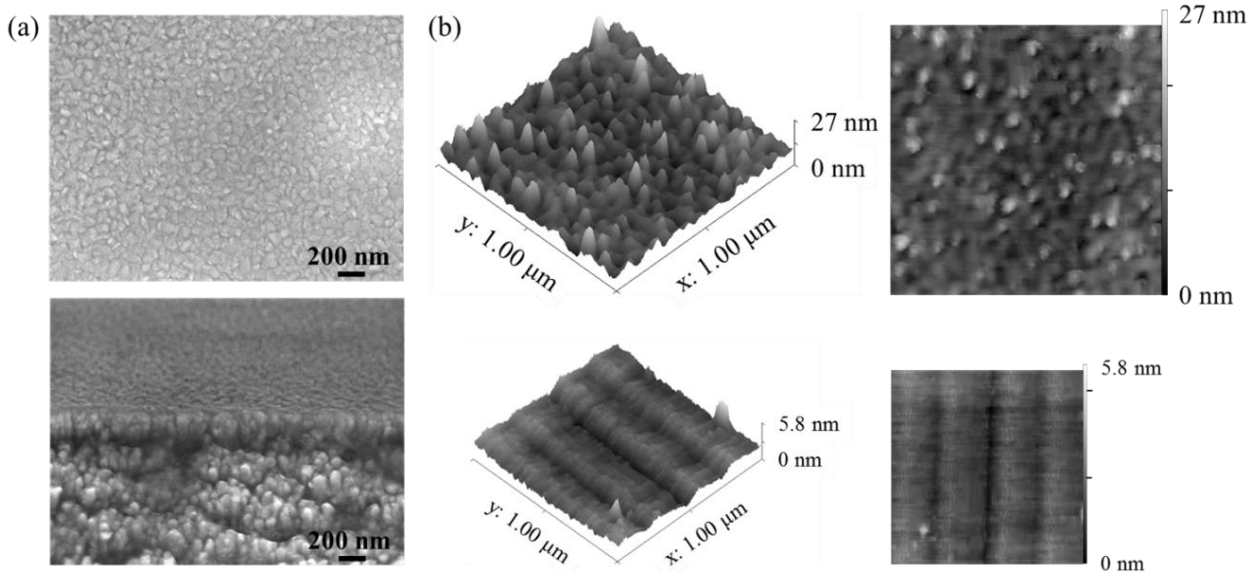

Fig. 3.2.1: GaP deposited onto diamond in an MBE system. (a) SEM images showing the nano-crystalline composition of the compound semiconductor layer with crystal sizes of 50 to 100 nm. (top: top view, bottom: side view onto edge of diamond substrate with GaP layer on top). (b) AFM imaging of GaP (top) and bare HPHT diamond (bottom) surfaces with an RMS surface roughness of 4.0 nm and 0.6 nm, respectively.

Waveguide loss measurements are utilized to both determine if the NV^- emission can be coupled into the GaP film and to quantify optical losses in the material. GaP waveguides with widths of 500 nm, 1 μm, and 2 μm are fabricated on the diamond substrate: after solvent cleaning, the samples are spin-coated with ma-N2401 electron beam resist and patterned in a 100 kV JEOL JBX-6300FS electron beam lithography (EBL) system. Etching of the GaP waveguiding layer is accomplished in an Oxford Plasmatherm 100 inductively-coupled plasma reactive ion etching (ICP-RIE) system using a chlorine (Cl_2) / argon (Ar) chemistry. After resist stripping, the waveguide structures are extended into the diamond substrate for enhanced confinement of the optical mode using an oxygen (O_2) dry etch. A SEM image of the fabricated structures is displayed in Fig.3.2.2. The top image shows two arrays of the waveguides with

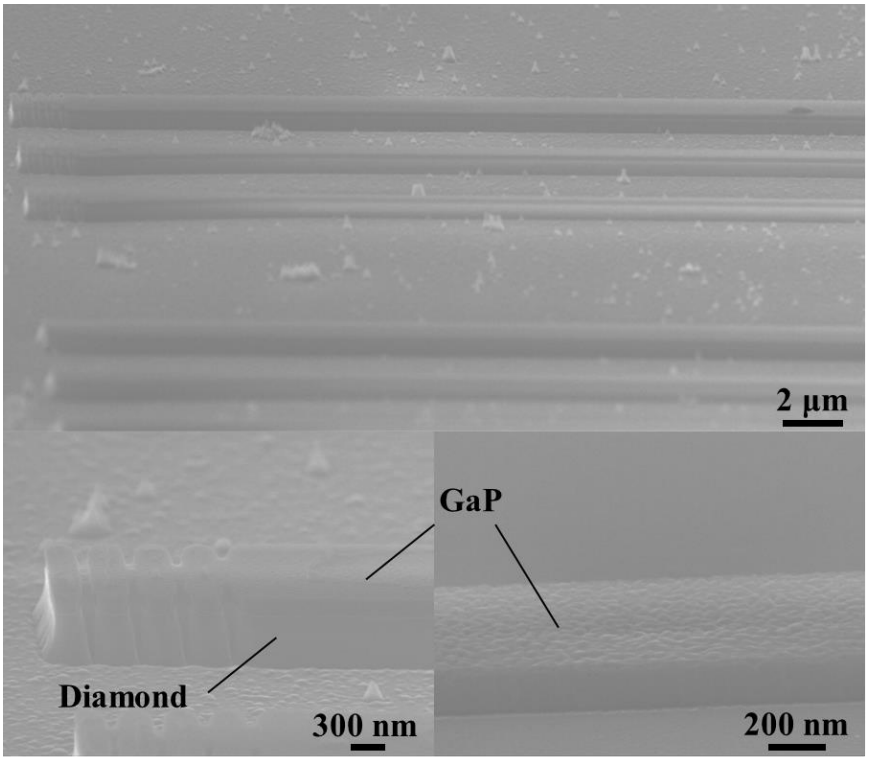

Fig. 3.2.2: Molecular beam deposited GaP waveguides fabricated on an HPHT diamond substrate prepared with NV centers for waveguide loss measurements. The top panel shows an SEM image of a group of 0.5 μm, 1 μm, and 2 μm wide waveguides. The bottoms panels display detailed views of a grating structures for coupling of the excitation into the waveguide (left) and the structure of the GaP waveguide top surface (right).

various widths. The bottom left panel shows the grating structures used to diffract the probe light into the waveguides. A magnified view of the waveguide top surface is shown in the bottom right image.

The optical loss is in the GaP waveguides is measured by launching 632 nm excitation light into the waveguide and collecting the NV^- PL excited by the waveguide mode. Fig. 3.2.3 schematically illustrates the measurements setup. 632 nm continuous-wave (cw) laser light is focused on the end of the waveguide structures. The NV^- PSB PL along the length of the waveguide is recorded with an imaging camera (AVT Guppy F-033B). The ability to perform this measurement indicates that the optical mode of the waveguide is in fact coupling to the near-surface NV centers.

The attenuation coefficient - or 1/e decay constant - α relates to the measured intensity *I* as:

$$I = I_0 \exp(-\alpha x) + I_{bg} \qquad \text{Eq. 3.1}$$

where I_0 is the initial intensity at distance 0, *x* the distance from the initial intensity, and I_{bg} the background intensity. The bright excitation spot is disregarded for extraction of the attenuation coefficient. With α known, the optical loss and the maximum attainable quality factor *Q* can be calculated. The loss per μm is defined as:

$$dB/\mu m = 10\ \log_{10}\left(\frac{P}{P_0}\right) = 10 \log_{10}(\exp(-\alpha \cdot 1\ \mu m)) \qquad \text{Eq. 3.2}$$

where P_0 and *P* are the incident power and power after 1 μm, respectively. Q_{max} can be determined by:

$$Q_{max} = \frac{2\pi n_{GaP}}{\alpha \lambda_{ZPL}} \qquad \text{Eq. 3.3}$$

where n_{GaP} is the index of refraction of GaP at the ZPL wavelength λ_{ZPL} (3.31 at 637 nm).

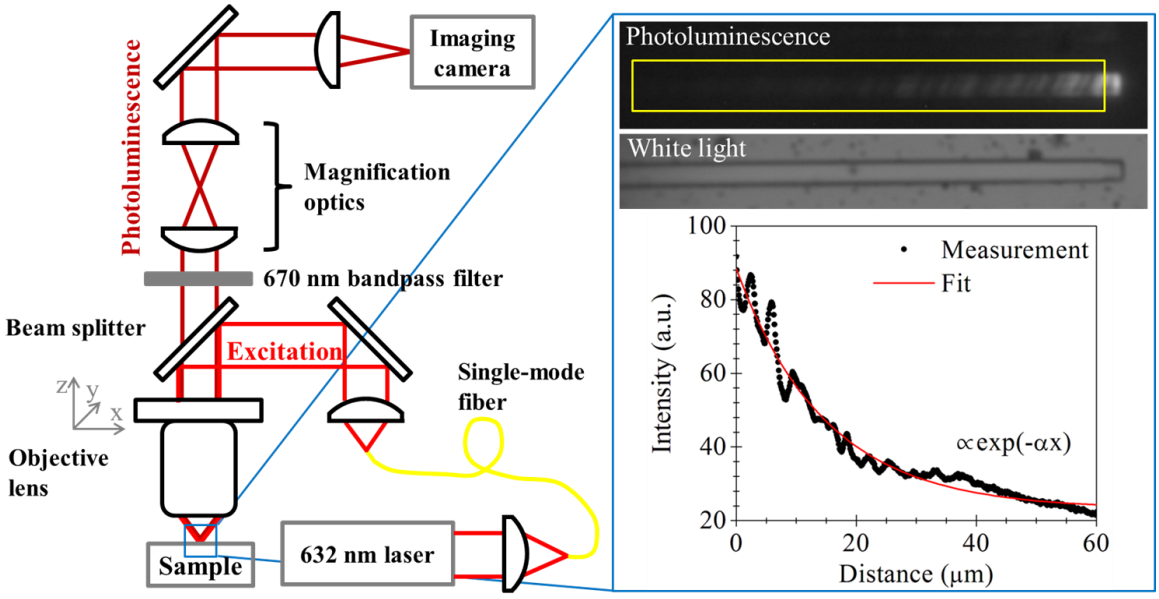

Fig. 3.2.3: Waveguide loss measurements utilizing PL intensity of NV centers underneath GaP waveguides as indicator for the decay of the coupled light as function of distance traveled. 632 nm cw laser light is coupled into the waveguide facet, and excites the near-surface defects in diamond. The emission into the PSB is recorded with a CCD camera. The panel on the right shows the PL intensity distribution along the length of a 2 μm wide waveguide, and a white light image of the device. The decay follows an exponential dependency from which the attenuation coefficient α can be extracted.

The attenuation constants and the respective calculated loss and quality factors for the 500 nm, 1 μm and 2 μm wide waveguides are summarized in Table 3.1. At least 4 devices of each width were evaluated.

The attenuation coefficients show a 1/e decay length of only few μm for all the devices, corresponding to losses > 0.4 dB/μm. Hence, the quality factors for resonators fabricated from the as-is material will be low, and are therefore not suited for the realization of devices for the Purcell enhancement of the NV^- ZPL. Optical losses can generally be caused by scattering at rough interfaces or defects within the waveguide, absorption in the bulk material or radiation losses in bent waveguides. Losses due to sidewall roughness are expected to be more pronounced for smaller waveguide widths. While the 500 nm wide waveguides show indeed shorter decay

Table 3.1: Attenuation coefficients, loss and quality factors and their respective standard deviations for nano-crystalline GaP waveguides with 0.5 μm, 1 μm, and 2 μm width on HPHT diamond. At least 4 devices are measured to extract the parameters for the respective waveguide widths.

Waveguide width (μm)	α (μm^{-1})	Loss (-dB/μm)	Q_{max}
0.5	0.15 ± 0.01	0.65 ± 0.04	218 ± 14
1	0.09 ± 0.01	0.40 ± 0.04	360 ± 35
2	0.10 ± 0.02	0.43 ± 0.1	340 ± 70

lengths, losses in the wider waveguides are similar. This may point toward scattering within the GaP bulk or at the GaP top surface, or absorption in the material being dominant loss mechanisms. Determining the major loss mechanism, and engineering the properties of the GaP films accordingly, may provide a route toward the facile integration of a high quality GaP device layer on diamond.

3.3 Molecular beam deposited GaP on SiO_2\Si substrates

To explore the causes of optical losses in GaP films deposited on diamond in a MBE system, 250 nm thick GaP layers are deposited at two different temperatures (180°C (LT) and 250°C (HT)) on more readily available 1 μm thick thermal SiO_2 layers on Si substrates. With GaAs layers deposited at lower temperatures having previously been shown to exhibit improved surface roughness [102], the growth of GaP at a reduced temperature of 180°C is explored as a possible route toward low-loss, high-refractive index waveguiding layers for the visible wavelength range. Post-deposition, the HT GaP layer on SiO_2 appears red-green, while the LT film appears silver. This could point toward non-stoichiometric nature of the LT GaP material. Reports on sputter-deposited GaP indicate prevalence of the metallic GaP phase in films for deposition temperatures below 200°C [90].

Fig. 3.3.1 displays SEM images of the respective top surface and cross-sections for both films. The LT sample appears smooth with no discernible features. In contrast, the HT GaP appears polycrystalline, with crystal sizes similar to the ones observed for the GaP on diamond layers. The cross-sectional view further reveals crystal boundaries, voids and a rough top surface.

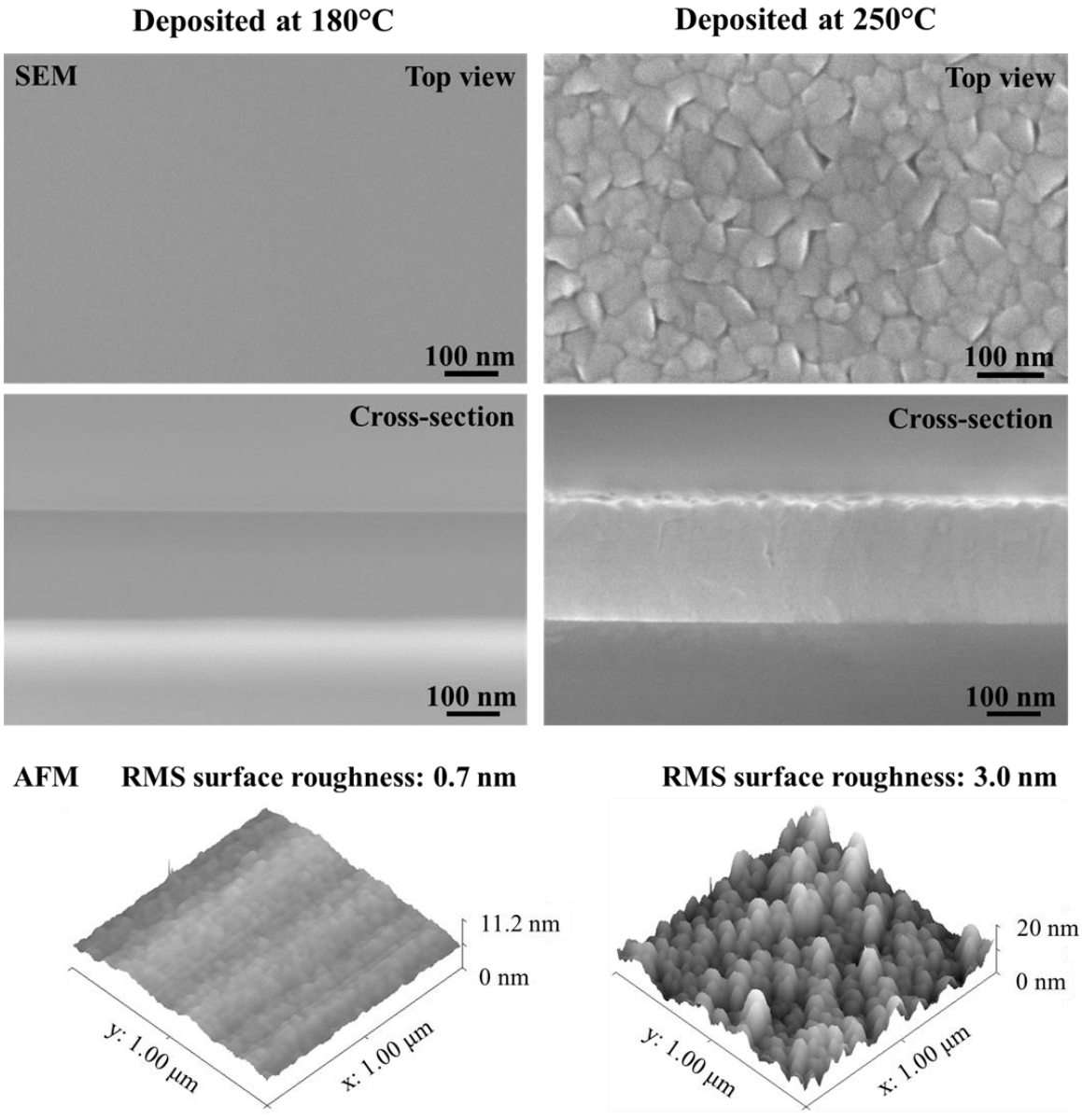

Fig. 3.3.1: GaP layers deposited onto diamond in an MBE system at 180°C (left panel) and 250°C (right panel), respectively. SEM and AFM images show uniform, smooth layer for deposition at lower temperature. In contrast, the layer deposited at 250°C appears nano-crystalline with voids and significant surface roughness.

These observations are in line with reflection high-energy electron diffraction (RHEED) measurements carried out during the deposition: while measurements during the HT growth indicate formation of a polycrystalline film, the LT growth is expected to result in an amorphous GaP layer. AFM measurements on both substrates confirm the presence of a smooth film for the LT sample (RMS roughness ~ 0.7 nm) and significantly more surface roughness for the HT sample (RMS roughness ~ 3.0 nm) (Fig. 3.3.1, bottom panel). Variable angle ellipsometry measurements (Woollam M-2000 Spectroscopic Ellipsometer) are carried out to determine the refractive index *n* and the extinction coefficient *k* for the visible wavelength range (Fig. 3.3.2). Comparing the measurements for both samples, the transparent range extends toward smaller wavelengths for the HT sample. The refractive index of the GaP layer at 637 nm extracted from the measurements is 4.19 for the LT and 3.41 for the HT substrate. The refractive index of the HT GaP film is in line with previously reported values [26], [79], [106]. While higher refractive indices are desirable for more efficient waveguiding, the significantly higher index extracted for the LT sample further points toward the non-stoichiometric nature of the deposited layer. This material also exhibits a high extinction coefficient of 0.34 at 637 nm. The extinction coefficient relates to the absorption coefficient α_{abs} via:

$$\alpha_{abs} = \frac{4\pi k}{\lambda_0} \qquad \text{Eq. 3.4}$$

with λ_0 the wavelength for which *k* was determined. Hence, with an absorption coefficient of 6.68 μm^{-1} and Eq. 3.3, a maximum quality factor of ~ 6 for 637 nm light can be estimated. In contrast, the extinction coefficient extracted for the HT GaP is about an order of magnitude lower (~ 0.04 at 637 nm). This value is similar to previously reported extinction coefficients for GaP films on sapphire [106] and silica after a high-temperature anneal [89] as determined by ellipsometry measurements. This corresponds to a maximum *Q* of ~ 42, which is also lower than

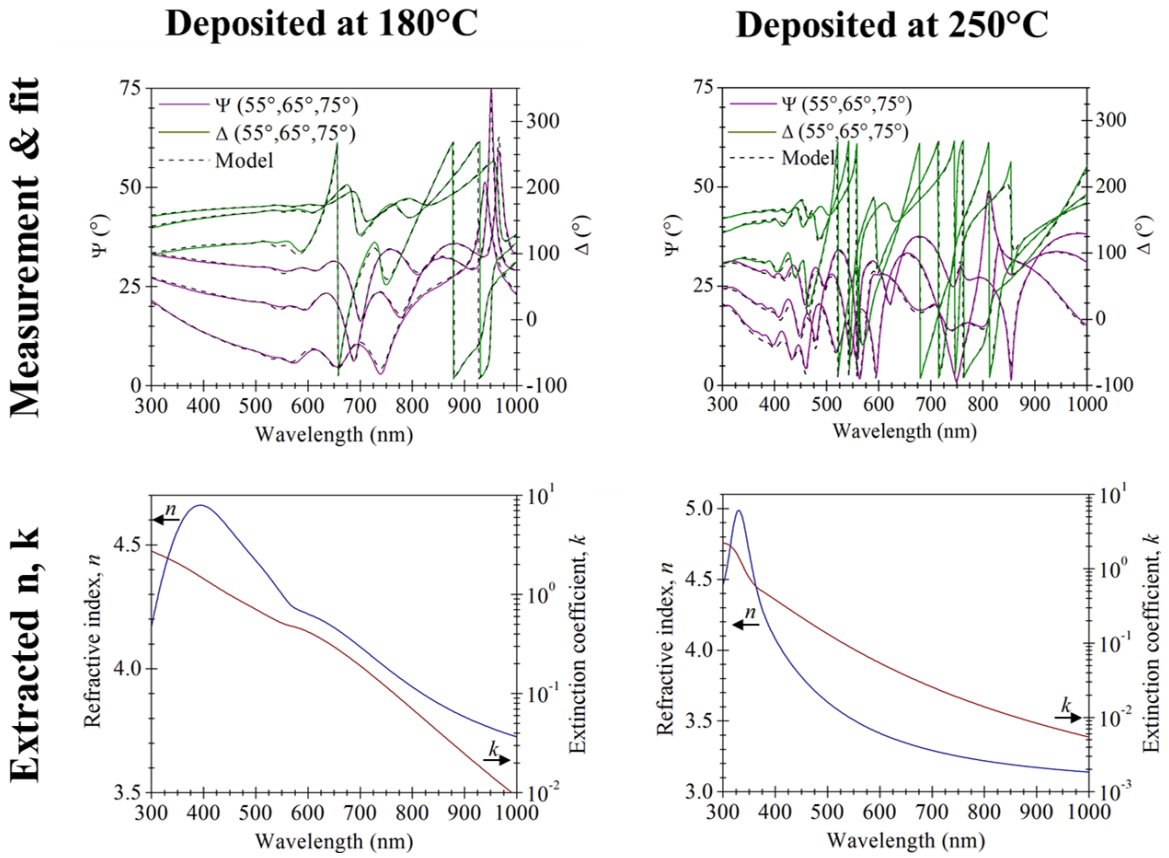

Fig. 3.3.2: Spectroscopic ellipsometry data, extracted refractive index and extinction coefficients for 180°C (left) and 250°C (right) GaP on SiO_2, respectively. The data is fit with a generic oscillator model (MSE, 180°C ~ 16.8, MSE, 250°C ~ 19.3). A surface roughness layer was included for both materials. [107] The transparent range extends further toward smaller wavelengths for the high-temperature sample. The extinction coefficient at 637 nm is about an order of magnitude higher in the sample grown at lower temperature.

expected if compared to the GaP\diamond films (for comparison, we seek to design devices with quality factors exceeding 10^4). The morphology of the two films deposited at 250°C appears similar, and the measured surface roughness for the GaP\SiO_2 sample is lower. However, the extinction coefficient is measured by ellipsometry whereas the attenuation coefficient for the GaP on diamond layer was determined from waveguide loss measurement. This difference may be explained by the different measurement geometries probed by the two methods. Ellipsometry samples the GaP through the rough top surface, whereas the waveguide loss measurements primarily sample the bulk of the material (Fig. 3.3.3).

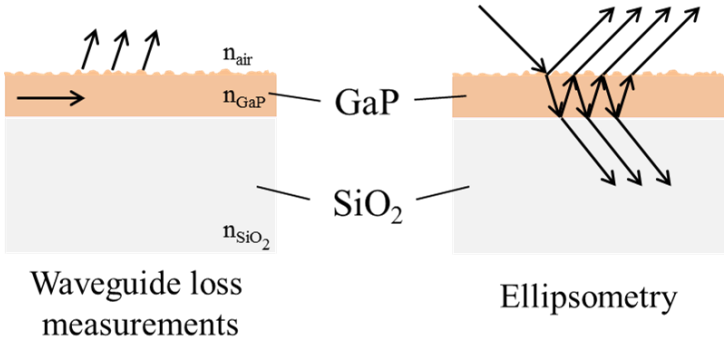

Fig. 3.3.3: Schematic measurement setup for waveguide loss measurement (left) and ellipsometry (right), respectively. Edge-coupling into GaP waveguide is expected to primarily probe the bulk of the dielectric layer, with the propagating modes mostly confined in this layer. Ellipsometry samples the layer of interest through the top surface.

To address this discrepancy, waveguides were fabricated in a similar fashion as described in section 3.2. The waveguide widths range from 500 nm to 20 μm. Fig. 3.3.4 shows SEM images of waveguides fabricated from both the LT (left) and HT (right) GaP material on SiO_2. The LT structures show straight, relatively smooth sidewalls. In contrast, the sidewalls of the HT waveguides appear rough. This roughness can be caused by the line edge roughness (LER) of the resist due to the non-uniform top surface or possibly preferential etching of the grain boundaries. The sample preparation is finalized by spin-coating of PMMA 495K/A2.5 resist as photoluminescent indicator of guiding in the waveguides. The samples are cleaved to allow for edge coupling of the probe light into the structures.

Fig. 3.3.5 displays a schematic of the setup for measurement of the waveguide losses. 638 nm light from a high-power laser diode is polarized and focused on the cleaved facets for edge-coupling. The light coupled into the waveguides evanescently excites the PL of the PMMA cladding. The PL signal is filtered and recorded on a CCD imaging camera (Andor iXon3). Optical losses for quasi-TE and TM are extracted in a similar fashion as described in section 3.2.

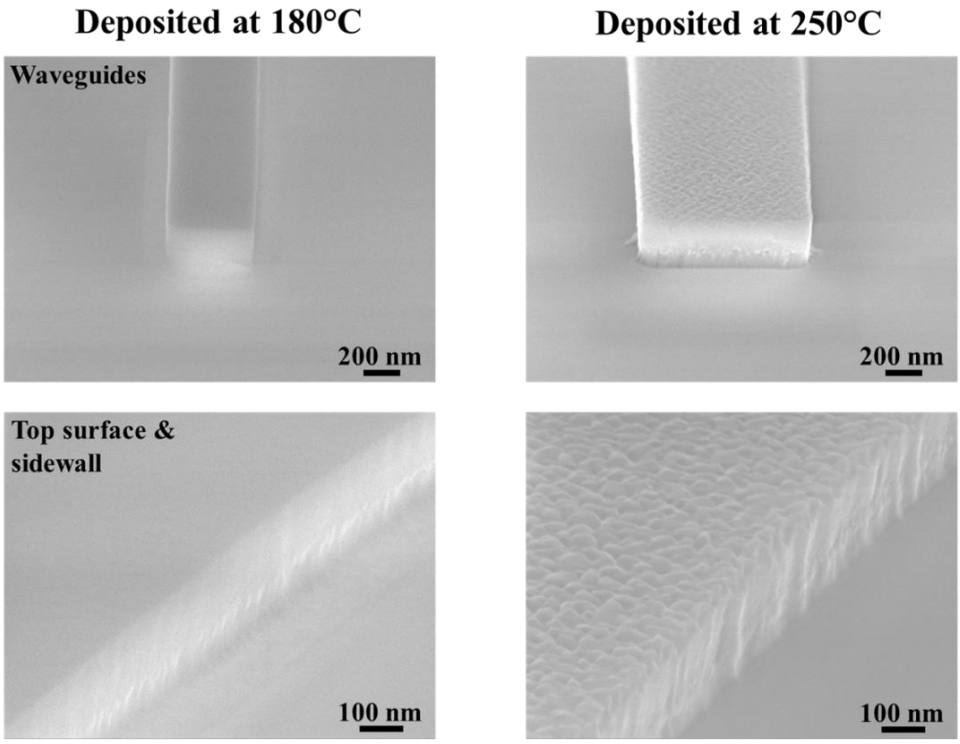

Fig. 3.3.4: GaP waveguides on SiO_2\Si fabricated from MBD layers deposited at the two different temperatures. The LT waveguides appear significantly smoother than the HT structures.

Table 3.2 summarizes the extracted losses for the fundamental TE mode, as measured for the HT GaP layer. The loss decreases for increasing waveguide widths, indicating a considerable loss component introduced by the sidewalls of the waveguides. Simulations with an in-house mode solver of TE modes in waveguides with the same height and different widths (carried out by M. Gould) indicate that there is a significant contribution from the rough top surface or possibly absorption in the GaP layer in addition to this sidewall loss. Fig. 3.3.6 displays the loss as function of the distance the guided mode travels in the waveguide for two 4 μm wide structures. The loss appears to beat, which is indicative of multi-mode propagation in the waveguides. The bottom panel in Fig. 3.3.6 shows the simulated x-component of the electric field for various phase differences between the main contributing TE_{00} and TE_{02} modes.

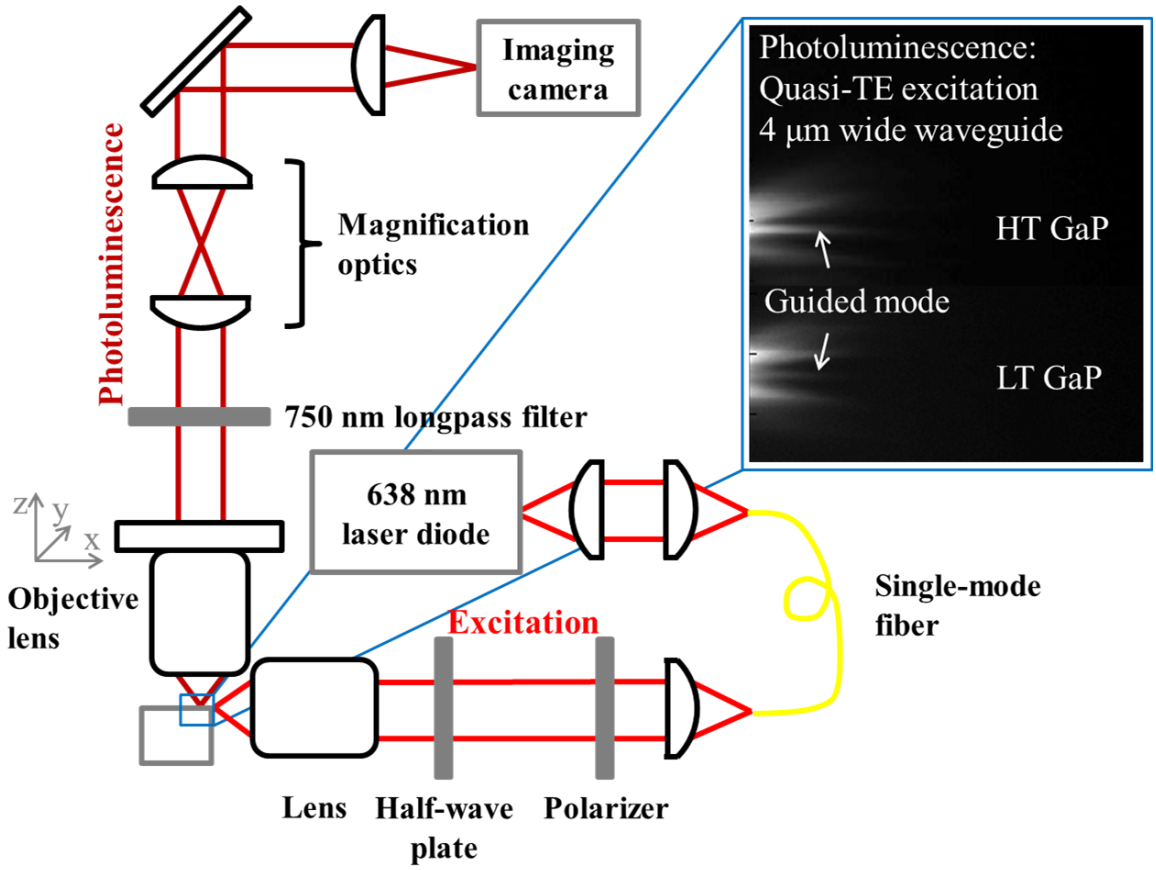

Fig. 3.3.5: Waveguide loss measurements in GaP waveguides on SiO_2\Si. The cleaved waveguide edges were excited from the side with a 638 nm laser diode. The PL of the PMMA layer was recorded as function of distance for both quasi-TE and TM excitation. The inset shows the PMMA PL excited by the guided mode in the center of the 4 μm waveguides, for both HT and LT GaP.

Table 3.2: Optical loss of the fundamental mode, attenuation coefficients and quality factors for HT GaP waveguides on SiO_2\Si, excited with quasi-TE 638 nm light. 5 devices were measured for each data point.

Waveguide width (μm)	Loss of the fundamental mode (-dB/μm)	α (μm^{-1})	Q_{max}
1	1.43	0.329	99
2	0.31	0.071	460
3	0.20	0.046	710
4	0.17	0.039	830
5	0.16	0.037	880

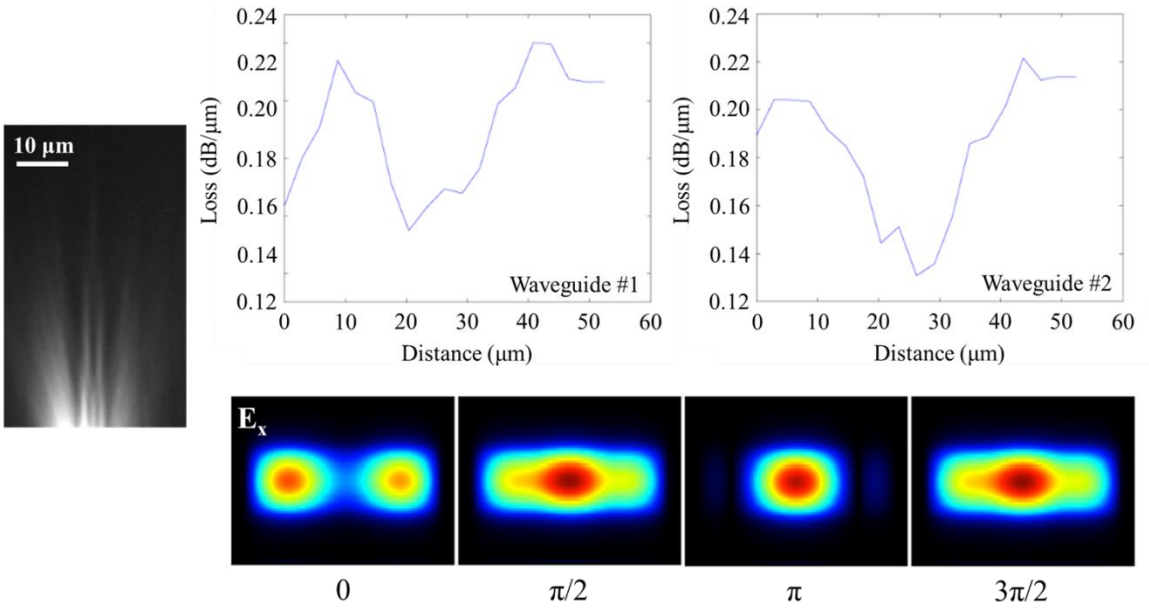

Fig. 3.3.6: Waveguide loss measurements for GaP waveguides on SiO_2\Si. The optical micrograph shows PL of the PMMA excited by a guided mode in the GaP waveguide, which exhibits beating. The graphs show the loss extracted for two different 4 µm wide devices. Beating of the loss indicates multi-mode propagation. The bottom panel displays the simulated electric field distribution (x-component) for several phase differences between the main guided TE_{00} and TE_{02} modes. Simulations are carried out by M. Gould.

TM polarized light can only be coupled to ≥ 2 µm wide waveguides, with a loss of > 0.5 dB/µm. This may further indicate polarization dependent absorption in the GaP film or significant losses due to the rough top surface.

A loss of > 0.45 dB/µm is found for coupling of TE polarized light to the LT GaP waveguides, corresponding to an attenuation coefficient of ~ 0.10 μm^{-1}. No coupling can be observed for TM excitation in these structures.

The attenuation constants extracted from the waveguide loss measurements are significantly smaller than the values extracted from the ellipsometry measurements (~ 0.78 μm^{-1}) for waveguides with widths > 3 µm and TE excitation. In contrast, waveguides with smaller waveguide widths show significantly higher attenuation constants, which is in line with an expected larger impact of sidewall scattering for small devices. The attenuation coefficients for

the smallest width waveguides are similar or even higher than the value extracted from the ellipsometry data.

To further explore the effect of the top surface, a hydrochloric acid (HCl) etch is employed to test for the presence of native GaP oxide. Fig. 3.3.7 shows high-magnification SEM of the GaP film before (left) and after (right) a 10 min HCl etch (diluted 10:1 in DI H_2O). No significant removal of any surface layer could be observed; the film remains rough. Cross-sectional transmission electron microscopy (TEM) of the as-deposited 250°C layer (Fig. 3.3.8) confirms that the GaP grains extend to the surface, and the variations in the height of the crystals of ~ 20 nm cause the surface to appear rough. This is in line with the AFM measurements presented above. No other material or morphology is apparent from these images.

The contribution of intrinsic absorption loss can ideally be determined by waveguide loss measurements at different wavelengths. The ellipsometry data in Fig. 3.3.2 indicates that the extinction coefficient increases significantly with decreasing wavelengths. The band gap of single-crystalline GaP is 2.26 eV at room temperature, corresponding to ~ 550 nm [108], [109]. Hence, waveguide loss measurements with longer wavelengths may be useful to determine

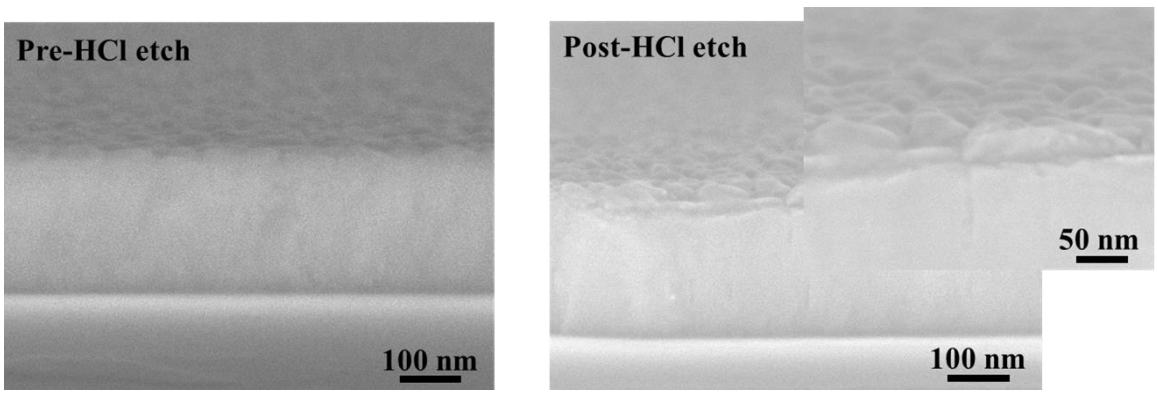

Fig. 3.3.7: Exploration of presence of high-loss surface layer on GaP grown at 250°C. Cross-sections of as grown samples were imaged before (left) and after (right) a 10 min etch in diluted HCl. The inset in the right panel shows the top surface after etching at higher magnification.

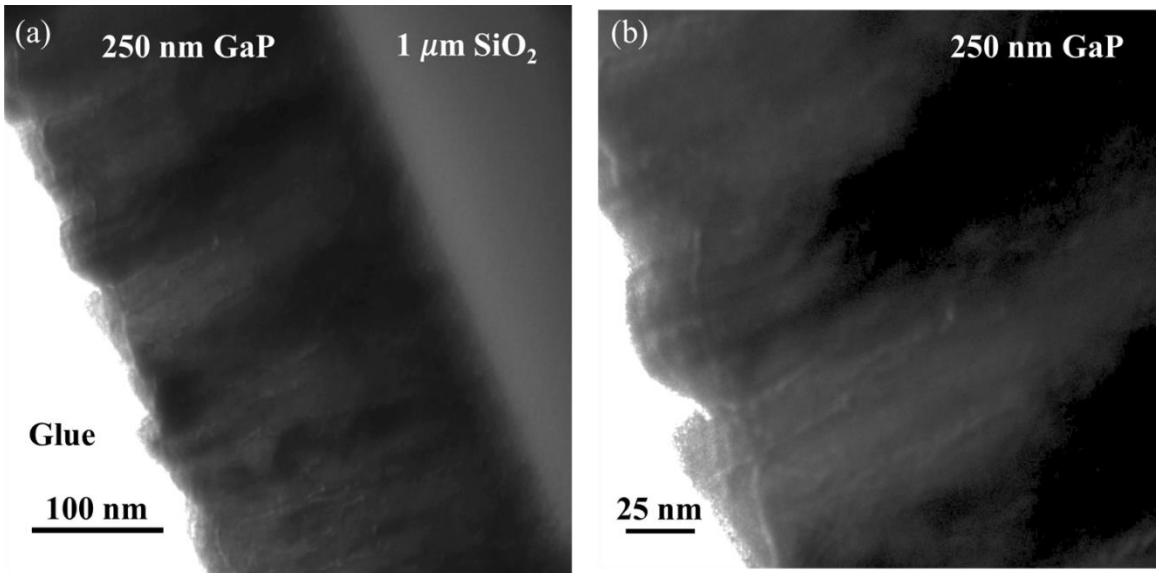

Fig. 3.3.8: Cross-sectional TEM imaging of GaP layer grown at 250°C. (a) Cross-section of 250 nm GaP on SiO_2 showing GaP crystals. (b) The high-resolution image of GaP top surface does not show any other materials or morphologies present on the GaP. (Courtesy of J. Faucher and M. L. Lee (Yale University).)

the contribution of material absorption to the overall loss. Longer wavelength excitation is attempted; however, the photoluminescence spectrum of the PMMA limits the usable excitation wavelength to < 700 nm [110]. Doping of the PMMA with QDs emitting at 800 nm (Invitrogen Qdot 800 ITK, carboxyl QDs) is employed to extend this wavelength range. However, no satisfactory QD concentration could be achieved for reliable measurement of the guided modes. It should, however, be possible to perform measurements with excitation wavelengths between 550-600 nm. Obtaining a wavelength dependence of loss may potentially point to absorption or scattering as the dominant loss mechanism.

3.4 Outlook for GaP layers deposited directly on diamond

Deposition of GaP directly on diamond with NV^- defect centers is appealing as a straight-forward avenue toward the realization of hybrid GaP\diamond optical devices. However, while coupling of the guided waveguide mode to near-surface NV^- centers in the diamond substrate can

be observed for the as-deposited GaP layers on HPHT diamond, high optical losses limit the potential quality factors of GaP resonator structures on diamond.

Hence, the as-deposited GaP layers are currently not a viable option for the realization of large-scale GaP photonic networks on diamond: low-temperature deposition (< 200°C) results in GaP layers that may contain a metallic phase and therefore exhibit extremely limited waveguiding capabilities. Waveguide-loss measurements for polycrystalline GaP deposited at 250°C indicate that the observed losses may be caused by scattering at the rough top surface, sidewalls or grain boundaries, or bulk absorption. Similar losses can be measured for layers deposited on single-crystalline diamond and amorphous SiO_2.

Despite the observed poor performance of the molecular beam deposited GaP for waveguiding layers at 637 nm, there are further techniques that could be employed in future studies to mitigate the observed loss. A reduction in the losses of polycrystalline materials has previously been demonstrated using high-temperature annealing, for example due to strain-relief in poly-Si [111] or oxidation of GaP films at 700°C [89]. However, annealing of GaP\diamond in air is limited due to the unstable nature of diamond at these temperatures. A promising next step may be an improvement of the surface roughness by chemical or chemical-mechanical polishing (CMP). CMP of III-V materials to RMS surface roughness < 0.5 nm has been achieved [112]. A reduction in surface roughness may also improve the sidewall loss in polycrystalline materials due to an enhancement in the resist LER. Even though this may be a promising route to explore, engineering of a CMP process that accounts for the mm^2-size and quadratic shape of currently available diamond substrates will be challenging.

Chapter 4:
Single-crystalline GaP resonator arrays on diamond

The currently limited performance of polycrystalline GaP layers deposited directly on diamond necessitates a different approach toward the integration of the two materials. Single high-*Q* GaP disk resonators have been fabricated on diamond from single-crystalline GaP material [29], [30]. However, the fabrication approach utilized does not allow for the integration of coupled GaP waveguide-cavity structures. Transfer of large-area single-crystalline GaP onto the diamond substrate and subsequent device fabrication, however, emerges as a viable route toward the realization of hybrid coupled photonic device structures.

Various physical transfer and bonding methods for substrates with different crystal structures or lattice constants exist, e.g., waferbonding and etch back or smart-cut [113]–[115], stamping of pre-released substrates [116]–[118], or self-assembly [119], [120]. Typically, these methods rely on additional interface layers or plasma treatment to promote adhesion [114], [118], [121], [122], ion implantation processes [114], [115], [123], or surface patterning and surface functionalization [119], [120], respectively. However, the hybrid GaP\diamond material system poses the following challenges:

- Coupling of the NV^- emission from the diamond substrate into the GaP waveguiding layer requires a pristine GaP\diamond interface.
- Properties of near-surface NV^- can deteriorate in partially graphitized diamond substrates or substrates with chemical surface treatment.
- Diamond is chemically inert.

- Small physical size of the currently available CVD and HPHT diamond substrates (2 mm x 2 mm) for diamond photonics applications.

Hence, commonly utilized technologies for layer transfer and bonding cannot be used for an integration of NV^- defects with a hybrid GaP\diamond photonic network.

Instead, a new transfer method is developed that relies on the lift-off of a GaP device layer from a secondary substrate and van der Waals bonding of this sheet on diamond. Coupling of the NV^- PSB emission to an array of single-crystalline GaP resonators fabricated using this epitaxial lift-off method is demonstrated.

4.1 Performance of single-crystalline GaP disk resonators

Before the development of transfer processes for the integration of single-crystalline GaP with diamond, the device characteristics of micrometer-sized disk resonators fabricated from commercially available single-crystalline GaP on $Al_{0.8}Ga_{0.2}P$ (IQE) are measured to show the potential of the MBE grown material for the realization of high-quality GaP device structures on diamond. The sample consists of a ~ 200 nm thick layer of GaP on an 800 nm sacrificial AlGaP layer on a GaP substrate. The epitaxial GaP layer show an RMS surface roughness of only ~ 1.2 nm, compared to an RMS roughness of ~ 3.8 nm for polycrystalline GaP, which is not expected to significantly decrease the device performance.

The resonators are fabricated similarly to the process described in section 3.2. The structures are defined in negative ma-N2403 electron beam resist and etched in a Cl_2/Ar plasma (Fig. 4.1.1). Resist removal is achieved in hot 1165 resist remover, with a final O_2 plasma strip. To increase the refractive index contrast, the AlGaP underneath the GaP disks is partially removed with a diluted hydrofluoric acid etch (1% HF (49%) in deionized water (DI H_2O)). The SEM image in Fig. 4.1.1 shows a 1.25 μm diameter GaP disk resonator on the AlGaP pedestal.

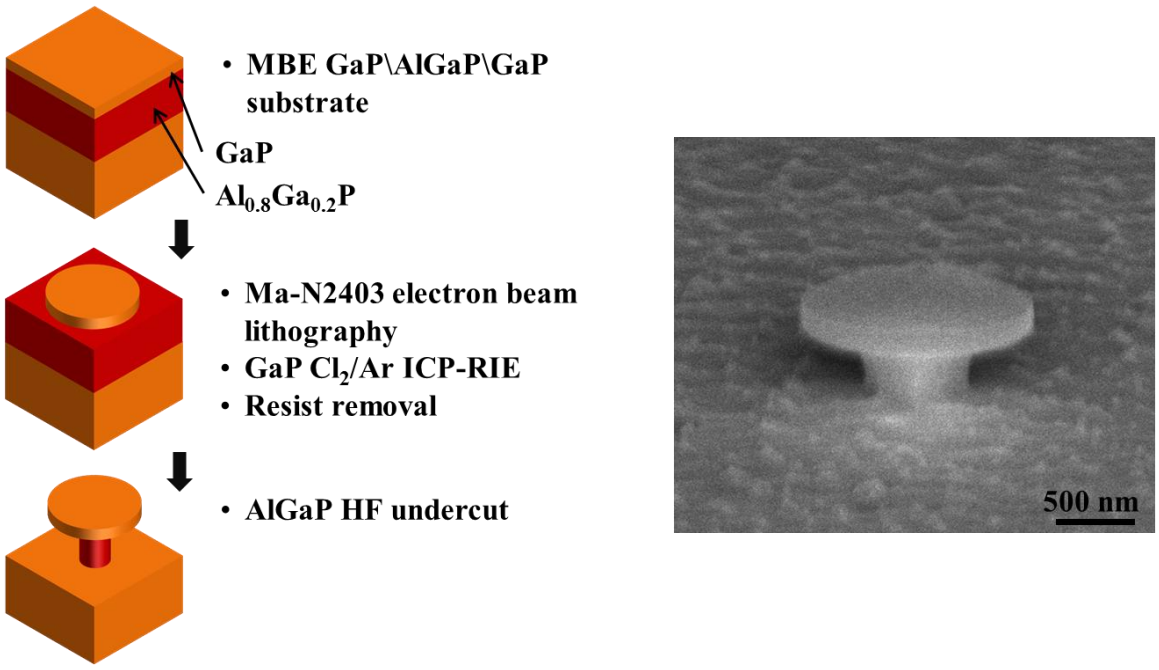

Fig. 4.1.1: Free-standing single-crystalline GaP disk for evaluation of MBE grown GaP\AlGaP\GaP layers for photonic device applications. The disk resonator devices were fabricated via electron beam lithography using negative ma-N2403 resist for patterning of the GaP device layer and a subsequent ICP-RIE step. Undercutting of the underlying AlGaP layer with BOE provides for a high-index contrast between GaP (n=3.31) and air necessary for for the emergence of whispering-gallery-modes. A SEM micrograph of a 1.25 μm diameter, 200 nm high GaP resonator is shown on the right.

Cadmium selenide/zinc sulfide quantum dots (CdSe/ZnS QDs, Ocean NanoTech QSP-635) are deposited on the disks from an isopropyl alcohol (IPA) solution. The QDs provide a broadband photon source with a peak wavelength of 636 nm for excitation of the whispering-gallery-modes in the optical resonators. Figure 4.1.2 displays a schematic of the measurement setup for the quality factor measurements as well as white light and PL images of the GaP devices. The CdSe QDs are excited with 532 nm cw laser light (diode-pumped solid-state laser, Laserglow Technologies LCS-0532-TFG). The QD PL is coupled into the disk, and subsequently scattered from the disk edge, where it is collected through a pinhole that is positioned 90° off the excitation spot to prevent collection of Fabry-Perot modes. The filtered spectra are captured either on a camera for visual inspection or via a McPherson spectrometer. The PL spectrum

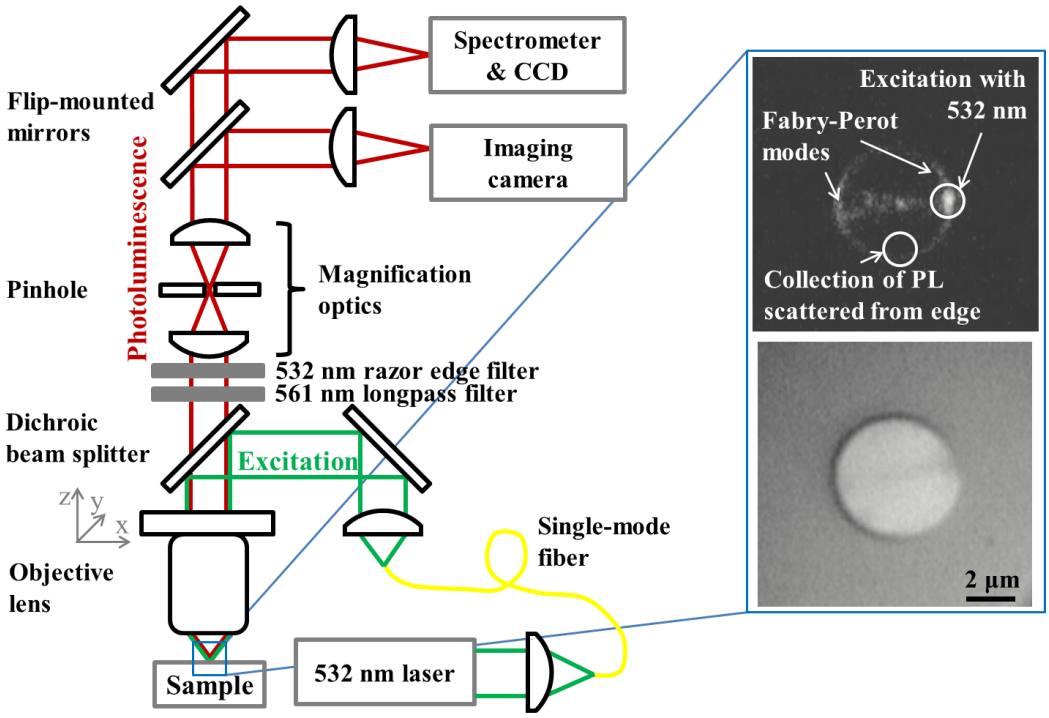

Fig. 4.1.2: Measurement setup for *Q*-factor measurements on free-standing single-crystalline GaP disk resonators. CdSe/ZnS QDs deposited on the edge of the resonators were excited with 532 nm cw laser light. The QD PL emitted into the disk and scattered of the edge of the resonator is recorded with a spectrometer.

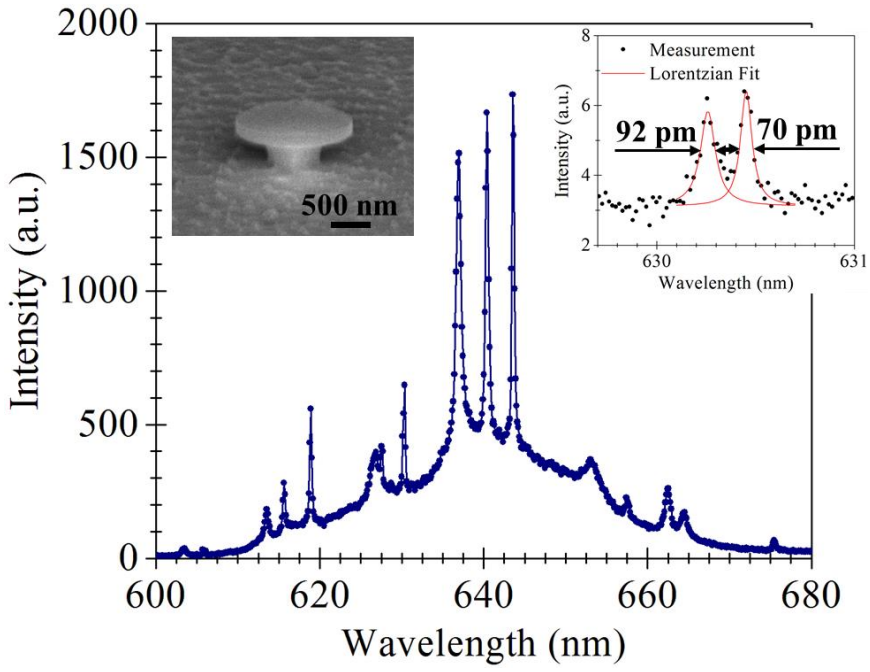

Fig. 4.1.3: Photoluminescence spectrum for 1.25 µm GaP disk. The CdSe/Zn QDs are excited with 1 mW 532 nm laser light. The maximum measured quality factor at 630.5 nm is ~ 9,000. Measurements are carried out at room temperature.

recorded for a 1.25 μm diameter GaP disk resonator is presented in Fig. 4.1.3. Both the broad-band QD PL background and sharp resonance modes are visible. The quality factor can be extracted by a Lorenztian line fit, which determines the resonance wavelength λ_{res} and *FWHM* (Eq. 2.13). The maximum *Q*-factor for this device is ~9,000. Comparing this to a maximally achievable quality factor < 500 for polycrystalline GaP devices, epitaxial single-crystalline GaP layers show significantly more promise for the implementation of integrated hybrid optical circuits on diamond. This motivates the development of a transfer process for the integration of single-crystalline GaP with diamond substrates.

4.2 Transfer of sub-micrometer thick GaP layers onto diamond

Transfer and bonding of large-area GaP layers to diamond are complicated by the processing limitations introduced above. Since no adhesion layers or surface functionalization can be employed nor can intermixing at the interface occur, adhesion between the transferred layers and the diamond substrate has to rely on van der Waals bonding. Fortunately, this is facilitated by the large area-to-height ratios of the device layers. Challenges remain, however, for the release the GaP layer from its original substrate, and the physical transfer of the sub-micrometer thick, fragile GaP sheets after release.

Two transfer processes are explored to enable integration of the two materials: The first attempt is based on removal of the backside GaP substrate to open etch windows through the GaP bulk to the AlGaP sacrificial layer. The AlGaP is then selectively removed in an HF vapor etch, thereby releasing the patterned device layer on the front of the substrate directly onto the diamond (Fig. 4.2.1). However, this approach results in GaP transfer with low yield and is therefore not suited for the realization of waveguide-integrated resonator structures. The final,

high-yield approach featuring epitaxial lift-off of the GaP device layers, is discussed in the second part of this section.

4.2.1 Transfer of GaP thin films onto diamond using backside etch and vapor release

While this initial transfer process is found inefficient, the process flow is included in this thesis to aid other researchers attempting hybrid material integration: The process starts with the deposition of PECVD SiO_2 on the front of the solvent cleaned substrate. Subsequently, a titanium (Ti) layer is deposited via electron beam evaporation, followed by photoresist layer. These films act as protective layers during the following lapping and back side etch processes. The back side of the samples is lapped from 450 μm to 120 μm thickness (3 μm aluminum oxide (Al_2O_3) slurry), and polished (0.3 μm Al_2O_3 slurry). The photoresist is then removed in acetone. Now, another layer of PECVD SiO_2 is deposited on the front side, followed by the deposition of PECVD SiO_2 as hard mask on the back of the sample. The back side SiO_2 is patterned by a positive photoresist in a direct write system, and dry etched in CF_4/CHF_3 plasma. After removal of the photoresist by sonication in acetone, the GaP bulk windows are etched in a specifically developed wet etching solution of potassium ferricyanide and potassium hydroxide (0.33 M $K_3Fe(CN)_6$ and 1 M KOH, heated to 80°C). The samples remain in solution until ~ 10 μm GaP is left on top of the AlGaP layer. Thereafter, the SiO_2 and Ti protective layers are removed in a buffered oxide etch (BOE). Now, the front side is patterned to define the areas to be released during the final AlGaP etch. The resist is exposed in a direct write system. Alignment between the front side pattern and back side etch windows is achieved visually through the now thin and transparent GaP substrate. The most critical step is the selective dry etch of both the GaP front side device layer and the GaP bulk with respect to the AlGaP. An SF_6/BCl_3 ICP-RIE etch is employed to first etch the front GaP layer [124]. After photoresist removal from the front of the

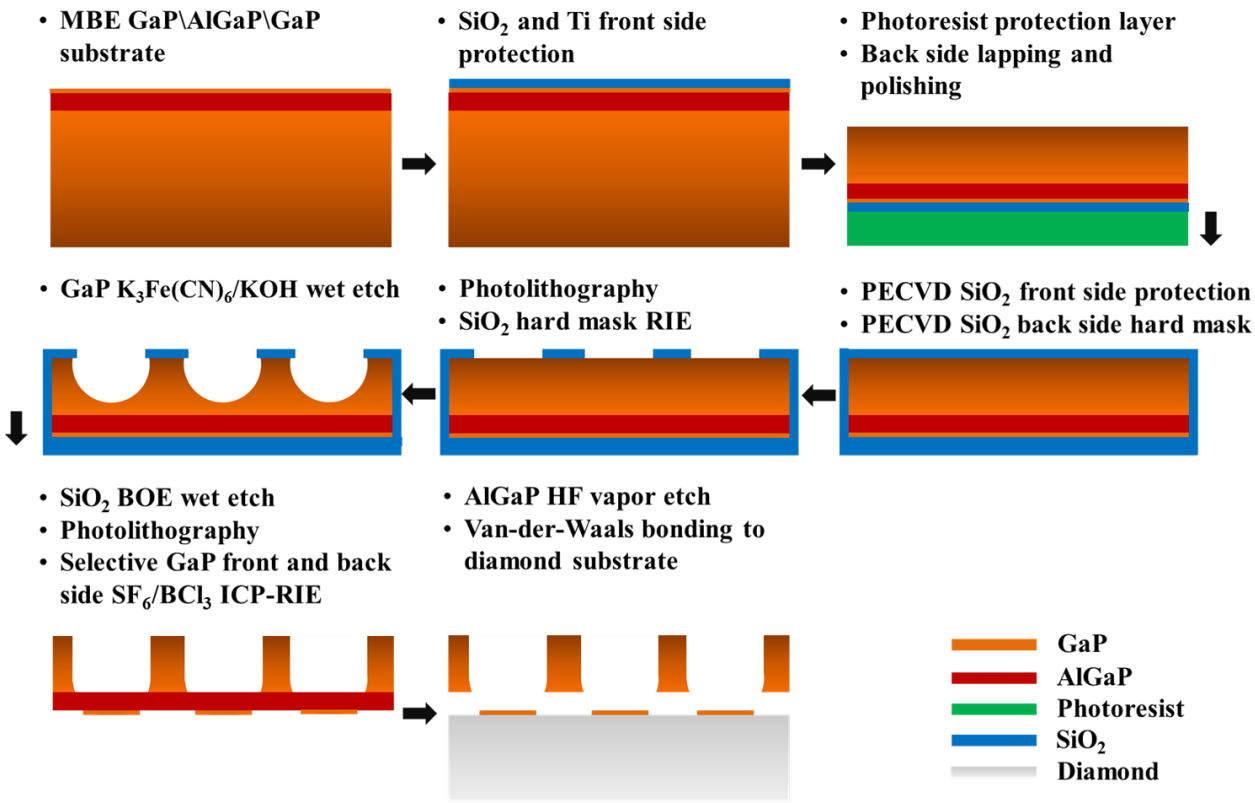

Fig. 4.2.1: Schematic process for flow for transfer of single-crystalline GaP onto diamond using a back etch and release approach. Protective SiO_2 and Ti layers were deposited on the sample front, followed by photoresist. The substrate was thinned from ~ 460 µm to ~ 120 µm thickness. The photoresist protective layer was then removed, and the sample was covered with a PECVD SiO_2 layer to act as both additional front side protection and back side hard mask. The back side SiO_2 was then patterned and dry etched. A wet etch was used to drive the back side windows into the GaP bulk until ~ 10 µm GaP remained on top of the AlGaP layer. SiO_2 and Ti were then removed from the sample with a BOE wet etch. A selective SF_6/BCl_3 ICP-RIE etch developed at HP labs allowed for a dry etch of the patterned front surface and subsequently the remaining GaP bulk material with AlGaP as etch stop layer. After positioning of the GaP piece on the cleaned diamond substrate, the AlGaP layer was removed with an HF vapor etch, and the GaP squares thereby released on the diamond surface.

sample, the back side windows are extended through to the AlGaP with the same etch. The final step is the release of the patterned GaP pieces. The diamond substrate is prepared for transfer by a wet chemical cleaning in Piranha solution. The GaP substrate is then positioned on top of the diamond substrate and exposed to full-strength HF vapor. HF selectively removes the AlGaP layer and releases the patterned GaP pieces onto the underlying substrate. A heating step to drive out any moisture between the GaP and diamond concludes the transfer. The substrates

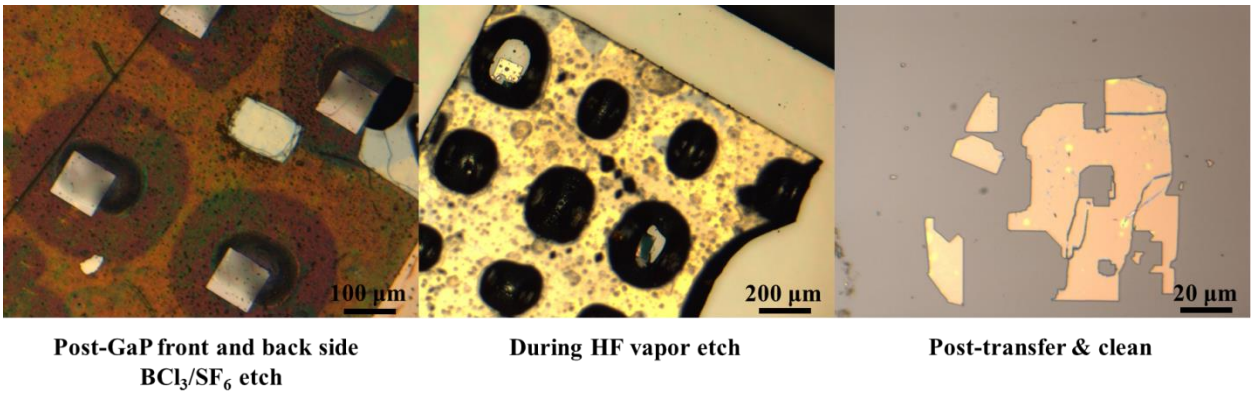

Fig. 4.2.2: Optical micrographs showing GaP substrate during different stages of processing. The left panel shows a sample after the back side GaP wet etch and the selective front side GaP dry etch, with the GaP squares to be transferred aligned to the back side windows. The next image displays the GaP substrate placed on the diamond sample mid-HF release. As can be seen, only few windows are etched completely through to the front surface. The image on the right shows a typical piece of GaP after transfer to diamond and solvent clean, with cracks and missing pieces.

undergo a final BOE dip to remove residual AlGaP, and a solvent clean.

Figure 4.2.2 displays optical micrographs of the GaP substrate at the final stages of processing, which also demonstrate some of the challenges of this process: the left panel shows the patterned GaP device layer and its alignment with the back side etch windows. While visual alignment is possible, inherent misalignment of the direct write system hinders the overall centering of the front side pattern to the back side windows. In the center panel, the GaP piece is placed on the diamond substrate and the AlGaP has been partially removed in vapor HF. As apparent, only a limited number of windows can be successfully opened. The $K_3Fe(CN)_6$/KOH etch chemistry preferentially etches the GaP (100) and (111) planes [125]. Hence, larger windows can be etched into more effectively. However, this requires the vias to be placed further apart and thereby limits the amount of GaP that can be transferred during a single run. Larger etch windows also result in larger AlGaP only membranes, with small thicknesses and limited mechanical stability. The transferred GaP pieces (Fig. 4.2.2, right panel) usually show cracks and

missing areas which further limits the efficiency of this transfer process. In addition, the fabrication scheme is extremely complex, with each step having the potential to decrease the overall yield.

4.2.2 Transfer of mm^2-sized GaP thin films using epitaxial lift-off approach

The initial fabrication scheme described above offers only limited yield in the transfer of single-crystalline GaP onto diamond. Inconsistencies in each single process step decrease its overall effectiveness due to the complexity and variety of processes used. Therefore, a simplified procedure is developed for transfer with high yield. The three-layer structure of the substrate lends itself to a different approach, i.e. lift-off of the top GaP device layer by removal of the sacrificial AlGaP layer only. This so-called epitaxial lift-off approach was first introduced by Konagai et al. for the fabrication of GaAs thin film solar cells [126], and has since been employed for the fabrication of GaAs photodiodes, LEDs, lasers, and, field effect transistors [127]–[132]. However, similar approaches for GaP have previously been unsuccessful [133].

This modified approach utilizes etch vias for the effective removal of the sacrificial substrate and release of the GaP device layer, combined with standard processing techniques. All processing is carried out on the front of the GaP pieces. The general procedure is as follows: After an initial solvent clean, the sample is patterned via standard photolithography and a Cl_2/Ar dry etch (Fig. 4.2.3 (b)). The optical micrograph at the top of Fig. 4.2.3 shows a typical substrate after the plasma etch step, with the resist layer in red/green and the GaP bulk appearing white. The photoresist defines both the outline of the GaP sheet to transfer and the 10 μm by 80 μm etch vias. After the dry etch, the GaP is released in diluted HF (Fig. 4.2.3(c)). The photoresist now aids as mechanical support of the released layer. The GaP sheet is transferred for a rinse in DI H_2O. Before bonding, the diamond substrate is cleaned in hot Piranha. The GaP sheet is then

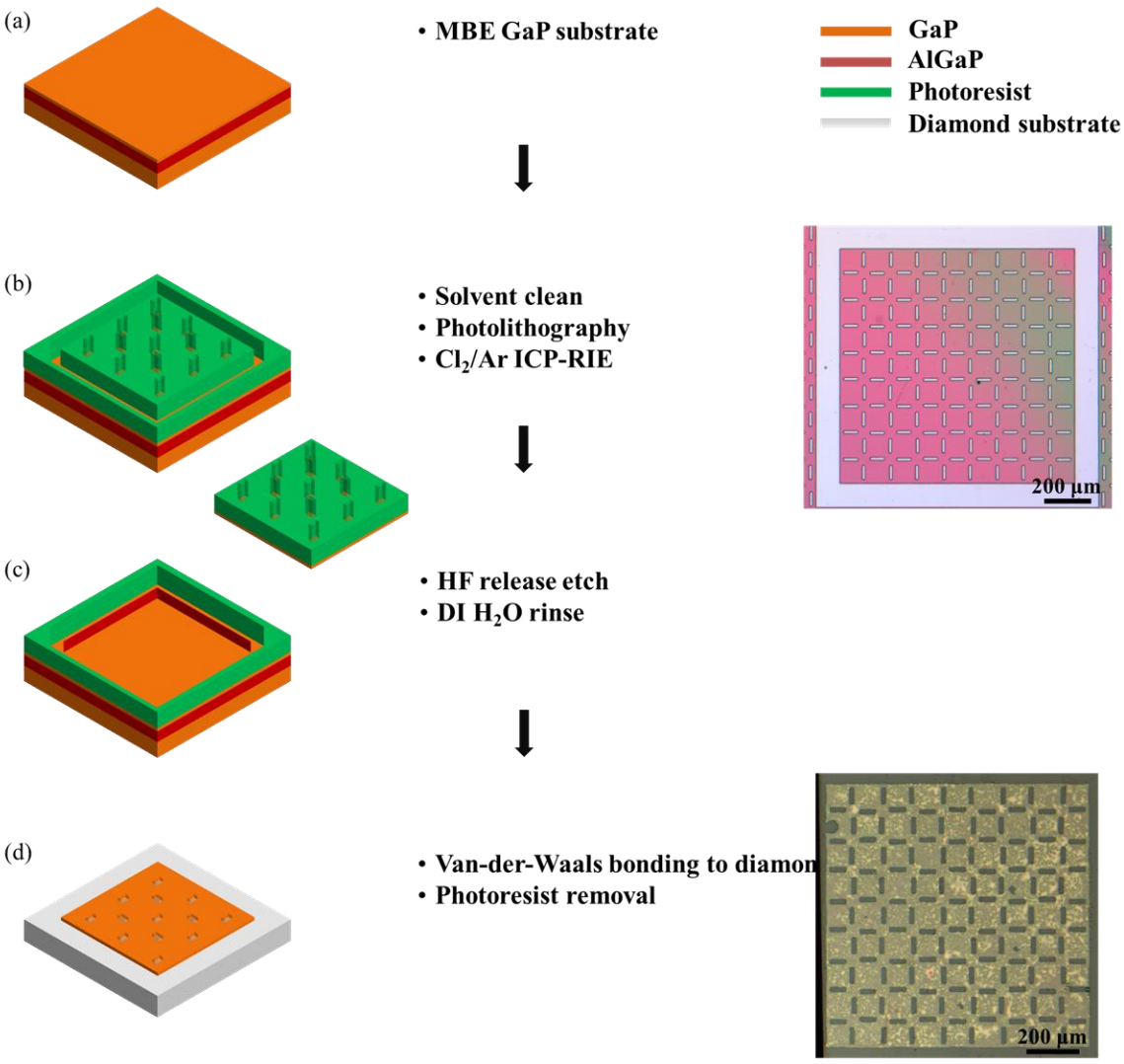

Fig. 4.2.3: Schematic process flow for transfer of submicrometer thick single-crystalline GaP device layer onto diamond utilizing an epitaxial lift-off approach. (a) The GaP substrate was prepared via MBE growth of a GaP buffer layer, an 800 nm thick $Al_{0.8}Ga_{0.2}P$ sacrificial layer, and GaP device layer. Before processing, the samples were cleaned by sonication in acetone and IPA. (b) A photoresist layer was spun, exposed and developed. This resist layer acts both as etch mask for the subsequent dry etch as well as mechanical support of the released GaP. The pattern is then transferred into the GaP\AlGaP\GaP substrate by a Cl_2/Ar ICP-RIE step. The optical micrograph shows the GaP device layer patterned for transfer with the resist after the etch. The total area of the transferred GaP sheets is 1 mm by 1 mm. (c) Subsequently, the GaP sheet with the resist layer is released from the substrate by the removal of the sacrificial AlGaP layer in diluted HF. (d) After a DI H_2O rinse, the GaP sheet is transferred onto the diamond substrate where it binds via van der Waals forces. Removal of the photoresist concludes the transfer process. A 1 mm by 1 mm sheet of GaP transferred to a mechanical-grade diamond substrate is displayed in the optical micrograph (bottom panel).

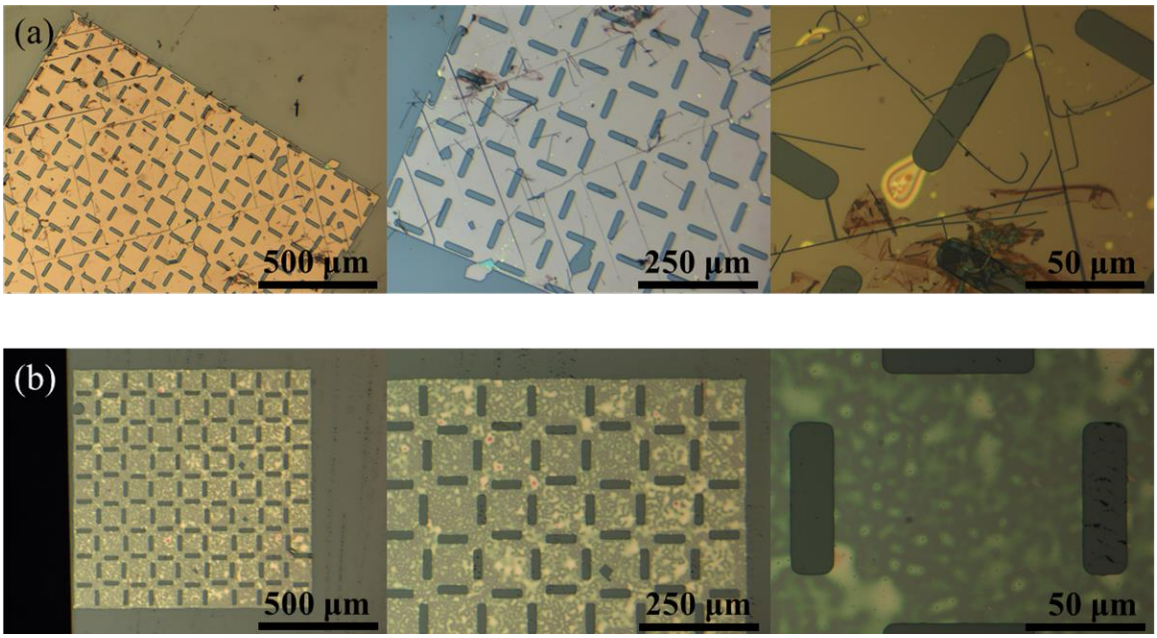

Fig. 4.2.4: Adaption of process conditions for high-yield GaP epitaxial lift-off and transfer. (a) Optical micrographs of initial transfer results showing numerous cracks in the transferred layer, photoresist residue even after extensive cleaning, and possibly etch residues along the etch vias. (b) Engineering of various process parameters results in high-yield transfer of mm^2-sized single-crystalline GaP sheets onto diamond. Photoresist thickness, dry etch parameters, HF concentration and post-transfer baking procedures were adapted. The initial transfer tests are carried out with CVD diamond ((a)), whereas the optical micrographs for panel (b) are obtained for mechanical-grade diamond substrate with µm-sized surface defects.

physically moved onto the diamond where it sticks via van der Waals forces. Removal of the photoresist concludes the transfer process. The optical micrograph at the bottom of Fig. 4.2.3 shows a 1 mm by 1 mm GaP sheet on diamond after removal of the resist.

The initial results of this approach are displayed in Fig. 4.2.4(a). While complete sheets are transferred, some areas are missing, there are long cracks running through the layers, and etch and resist residues along the etch vias are visible. Fig. 4.2.5 illustrates the impact of sample geometry and etch chemistry on the release etch [131]. Tension in the top layer curls the released sheet with a radius of curvature R. The speed of the horizontal etch v is limited by the out-diffusion of H_2 gas, $-D\nabla n$ with D the diffusion constant of H_2 gas and n its molar concentration.

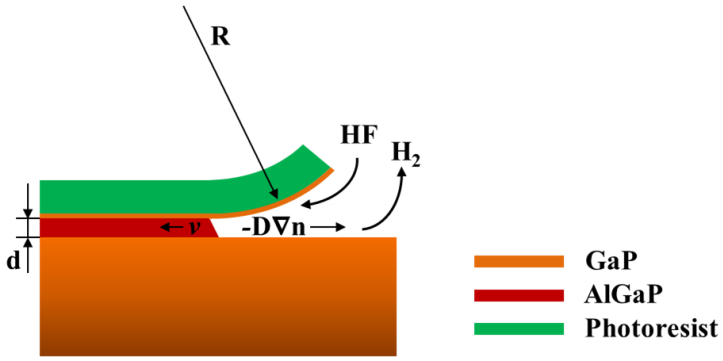

Fig. 4.2.5: Impact of layer geometry on HF AlGaP etch characteristics. Mass-flow of the reactants and reaction products limits etch performance. Hydrogen as major etch product can form air bubbles and crack the substrate if sufficient removal from reaction site is not possible. Furthermore, intrinsic stress in the top layer determines opening for HF and H_2 transport. [131]

If too much HF is present, H_2 bubbles form whose hydrostatic pressure can crack the GaP layer. The out-diffusion of H_2 gas can be enhanced with higher tension in the top layer, which results in opening up the etch channel. However, higher tension and therefore higher curling also induce mechanical stress in the GaP sheet.

The cracks along all four corners of the released GaP sheet indicate fracturing due to high stress. The corners are released faster than the center area and are therefore exposed to larger tension. This issue can be solved by thinner resist layers. Furthermore, the orientation of the etch mask is changed. The cracks in the center of the GaP sheet, along specific lattice planes, point toward defects in the GaP lattice being preferentially etched by the HF [134], [135]. A lower HF concentration prevents this. The GaP etch and resist residue along the outlines of the etch vias could be caused by high temperatures during the Cl_2/Ar ICP-RIE. The plasma etch possibly burns the photoresist, therefore making it hard to remove in wet chemical solutions. The results of the transfer with improved process parameters are shown in Fig. 4.2.4(b). While initial transfer experiments are carried out with electronic-grade CVD diamond substrates, the bottom panel shows optical micrographs taken for transfer to a mechanical-grade diamond substrate with

Table 4.1: Process parameters for transfer of sub-micrometer thick GaP device layers.

Parameter	Initial condition	Improved process
Photoresist thickness	AZ9260, 8 μm thick	AZ1512, 1 μm thick
Alignment of GaP edge	Along <110>	Along <010>
Cl_2/Ar ICP-RIE etch time	2 min	3 x 40 s with 5 min cool-down after each etch
Wait time between ICP-RIE and HF release	None	> 3 days
HF concentration	1:13 HF (49%): DI H_2O	1:100 HF (49%): DI H_2O
Post-transfer bake	30 min at 100°C	None
Final bake	None	48 hours at 75°C

μm-sized surface defects. These defects can cause air to be trapped underneath the GaP layer, visible as lighter spots in the image. The mm^2-sized GaP sheets now appear largely intact and without cracks. The GaP etch and photoresist residues cannot be observed anymore. Table 4.1 summarizes the improved process parameters.

4.3 Coupling of near-surface NV^- emission to a GaP disk resonator array

To demonstrate the suitability of the developed transfer process for the integration of GaP photonic devices with near-surface NV^- centers, the process is utilized for the fabrication of a large array of GaP resonators on diamond. An electronic-grade CVD diamond substrate is prepared with NV^- centers via ion implantation (10^{10} cm^{-2}/10 kV) and a two-step anneal, as described in section 3.1. Single-crystalline GaP is transferred onto this substrate with the epitaxial lift-off method introduced above. A GaP resonator array, with disk diameters ranging from 1 μm to 20 μm, is fabricated by EBL with ma-N2401 resist, and a subsequent Cl_2/Ar dry etch. Removal of the electron beam resist in hot 1165 resist remover finalizes the fabrication. Fig. 4.3.1 displays an SEM image of the GaP resonator array. Since the electron beam lithography pattern is not aligned to the transferred sheet, GaP disks overlaying with the etch vias

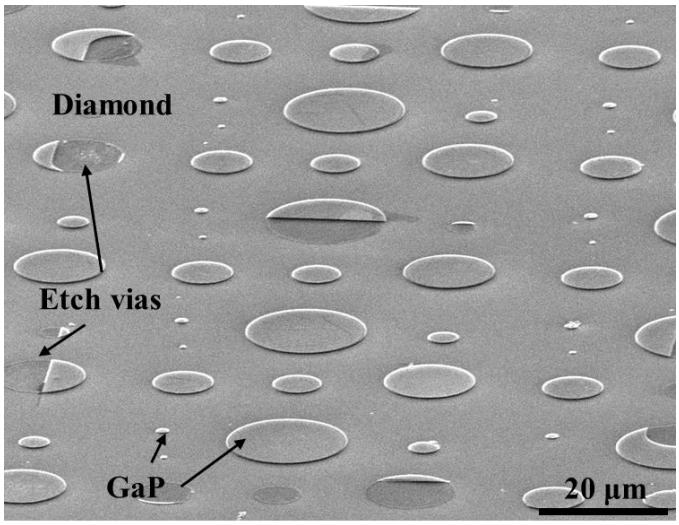

Fig. 4.3.1: SEM micrograph of single-crystalline GaP disk resonator array fabricated on an electronic-grade CVD diamond substrate prepared with near-surface NV centers. The diameters of the resonators ranged from 1 to 20 µm. Since the electron beam lithography pattern was not aligned with the transferred GaP sheet, some structures overlay with the etch vias in the GaP layer.

appear partially missing.

The GaP disk resonator array is characterized in a similar fashion as the devices in section 4.1. Instead of using QDs as broad-band photon sources near the edges of the resonators, however, coupling of the PSB emission of NV^- centers into the disks is observed. NV^- centers in the diamond substrate, close to the edge of the GaP disks, are excited with 532 nm cw laser light. The PL emission coupled into the resonators and scattered off the edge is recorded off-angle from the excitation spot. Fig. 4.3.2 depicts PL spectra for a 5 µm and 10 µm diameter GaP disk on diamond, respectively. The PL spectrum of the 10 µm disk (Fig.4.3.2(a)) shows sharp resonance modes on top of low-frequency Fabry-Perot interference modes and NV^- background PL. The wavelength range of interest covers the NV^- ZPL and PSB. Resonance modes being observed over the PSB range indicates successful coupling of the NV^- emission into the disk, with the PSB emission exciting the respective whispering-gallery-modes. Fig. 4.3.2(b) shows the characteristic PL spectra for the highest quality factor for a 5 µm GaP disk. The Lorentzian line

fit at ~ 630.0 nm reveals a *FWHM* of ~ 58 pm, corresponding to a *Q* of ~ $1 \cdot 10^4$. These device characteristics are promising for the implementation of coupled waveguide-resonator structures fabricated from GaP sheets transferred onto the diamond using the epitaxial lift-off approach. However, cavities with smaller diameters, and therefore smaller mode volumes, will be necessary for efficient Purcell enhancement. Due to the low refractive index contrast between diamond and GaP no resonance modes are expected for GaP disk diameters < 1.5 µm, as discussed in the next chapter.

Successful coupling of the NV^- emission to an array of GaP disk resonators constitutes the first demonstration of GaP device structures fabricated in a deterministic fashion on diamond and integrated with the near-surface optical defects. This indicates that epitaxial lift-off and van der Waals bonding of the released GaP layer to diamond is a viable solution for the integration of the two materials.

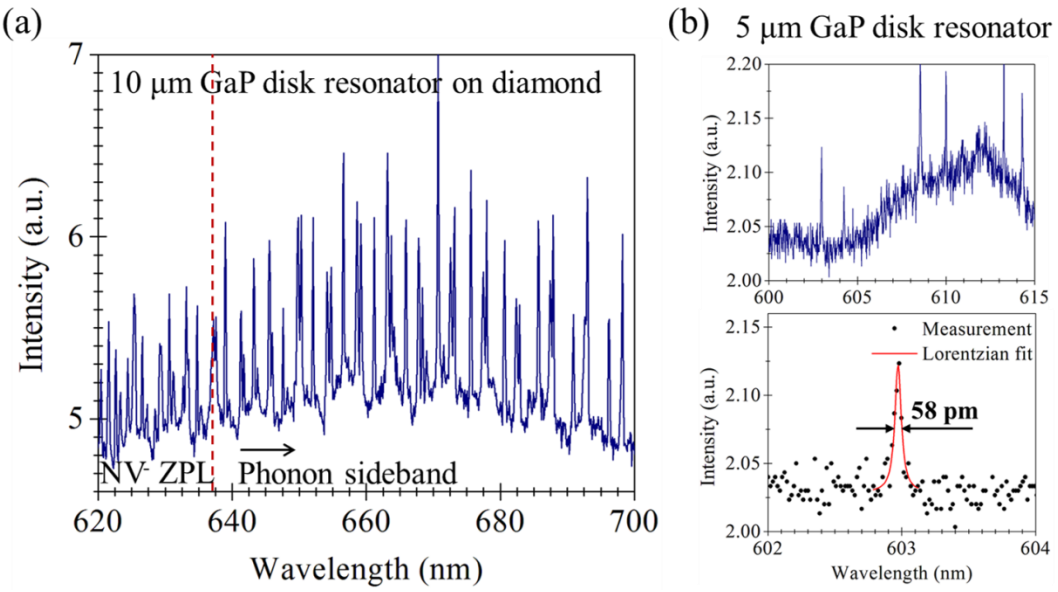

Fig. 4.3.2: Photoluminescence spectra measured for (a) 10 µm and (b) 5 µm diameter GaP disk resonators on CVD diamond with near-surface NV centers. Optical defects near the edge of the GaP disks were excited with 150 µW 532 nm cw laser light. The spectra were recorded with the collection spot located 90° off the excitation spot. (a) The 10 µm disk spectra shows resonant whispering-gallery modes excited through the NV emission coupled into the GaP resonator. (b) A maximum *Q* of ~ $1 \cdot 10^4$ was measured for a 5 µm disk.

Chapter 5:
Waveguide-integrated single-crystalline GaP resonators on diamond

With the demonstration of hybrid GaP\diamond disk resonator arrays coupled to nitrogen-vacancy (NV^-) centers in diamond, an avenue toward the integration of coupled GaP photonic device structures for the collection, enhancement and off-chip routing of the NV^- emission is opened. The next, critical step toward large-scale optical networks on diamond with inherent linear electro-optic (EO) functionalities is the demonstration of waveguide-coupled GaP resonators on diamond. To reach this goal, GaP disk resonators integrated with waveguides are realized from a single-crystalline GaP layer transferred onto a mechanical-grade diamond substrate using the epitaxial lift-off technique described in the previous chapter (Fig. 5.0.1).

Engineering of the coupling characteristics of waveguide-integrated resonators requires optimization of device dimensions and placement. Furthermore, fabrication processes have to be adapted to enable the realization of narrow resonator-waveguide coupling regions and off-chip grating couplers for device testing. Finally, the fabricated devices must be characterized with regard to potential coupling efficiencies of NV^- zero-phonon-line (ZPL) photons collected from the diamond with the GaP resonators and routed into the waveguides.

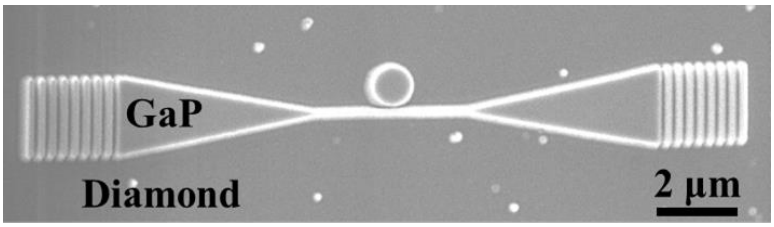

Fig. 5.0.1: Top down SEM image of hybrid GaP/diamond photonic circuit with 1 µm diameter GaP disk resonator coupled to waveguide and out-off-plane grating couplers.

In section 5.1, the design of the resonator-waveguide coupling regions using finite-difference time-domain (FDTD) simulations is discussed. The simulations indicate that ≤ 100 nm gaps are required for efficient coupling. In section 5.2, the optimization of the fabrication processes for the implementation of sub-100 nm gaps between resonators and adjacent waveguides is presented. Section 5.3 describes the final fabrication flow for the devices. Transmission measurements performed to extract the device characteristics are presented in section 5.4. The measured device characteristics enable us to quantitatively evaluate the potential coupling efficiencies in the GaP devices for photons emitted by NV^- centers in the diamond substrate. The device properties are found promising for an efficient collection and routing of NV^- ZPL photons in the hybrid platform. This is the first demonstration of coupled photonic devices fabricated from a linear EO material integrated with diamond.

5.1 Design considerations for waveguide-coupled GaP resonators on diamond

High-fidelity entanglement generation in an integrated optical network will largely depend on the adequate collection of the NV^- ZPL photons in on-chip cavities and routing to integrated bus waveguides. These features critically depend on the following parameters:

- Coupling of the NV^- ZPL to the GaP cavity.
- Effective coupling between the GaP resonator and a bus waveguide for on-chip photon routing.
- Efficient detection of the NV^- ZPL photons for entanglement generation.

Ideally, the detection of ZPL^- photons would be performed on-chip. Technologies for on-chip single photon detection are an active area of research [86], [87]. In this work, however, out-of-plane grating couplers are utilized to couple probe light to the GaP waveguides for a first proof-of-principle demonstration of waveguide-resonator coupling in a hybrid GaP\diamond network.

The design of the GaP grating structures and taper regions on diamond, which is not a focus of this thesis, is presented in Appendix B for the interested reader.

Efficient coupling of the NV^- ZPL to a GaP resonator on diamond is a function of both the NV^- location and orientation in the diamond lattice as well as the optical parameters of the cavity structures. A strong enhancement of the spontaneous emission rates of NV^- ZPL photons in a resonant cavity is desirable for high-fidelity entanglement generation. In bulk diamond, only 3% of the NV^- emission is typically emitted into the ZPL [43], [44]. As discussed in section 2.4.2, a cavity can be used to enhance the NV^- emission into the ZPL line. This enhancement is proportional to Q/V, in which Q is the cavity quality factor and V is the cavity mode volume:

$$F_{ZPL} \propto {}^{Q}/_{V} \qquad \text{Eq. 5.1}$$

Therefore, a large enhancement requires high-Q devices with small mode volumes. Measurements of the quality factors of 1.25 μm GaP disk resonators in air indicate an upper bound of ~ 10^4 for the intrinsic cavity quality factor Q_i, either due to material limitations in our GaP or fabrication imperfections. Thus, for our devices the highest Purcell enhancements will be achieved by fabricating devices with as small of diameter as possible while still maintaining Q_i ~ 10^4.

The overall quality factor of a cavity integrated with a waveguide is further determined by the coupling characteristics between the two structures. This is the loaded quality factor Q_l:

$$\frac{1}{Q_l} = \frac{1}{Q_i} + \frac{1}{Q_c} \qquad \text{Eq. 5.2}$$

where Q_c is the coupling quality factor. The coupling characteristics can be optimized by finding the ideal waveguide-resonator spacing and waveguide width for a resonator with a known Q_i. From Q_i, the round trip loss in a cavity can be estimated. For critical coupling, i.e. Q_i=Q_c, this

round trip loss should be compensated by the field coupled from the bus waveguide to the resonator for each cycle. We use this critical coupling condition to dimension our initial device structures. A rigorous analysis presented in section 5.5 confirms that optimally designed devices operate near critically coupling. 3-dimensional (3-D) FDTD simulations are carried out to estimate the single-pass coupling characteristics for different waveguide and resonator geometries. The MIT Electromagnetic Equation Propagation (*Meep*) FDTD package (Version 1.1.1/1.2/1.2.1) [136], [137] is used for simulations, which are run on either an Intel Core i5-2540M/4 GB RAM platform or an MPI cluster on Amazon Elastic Cloud (the parallel computing interface was developed by K. Jorissen and J. Rehr, University of Washington).

An illustration of the electric fields in a 2 μm diameter, 120 nm wide ring waveguide coupled to an adjacent 100 nm wide straight waveguide located 100 nm away is shown in Fig. 5.1.1(a). The GaP layer is 200 nm thick, and the GaP structures sit on 600 nm high diamond pedestals. As will be discussed in section 5.4, etching of the diamond substrate enhances confinement of the

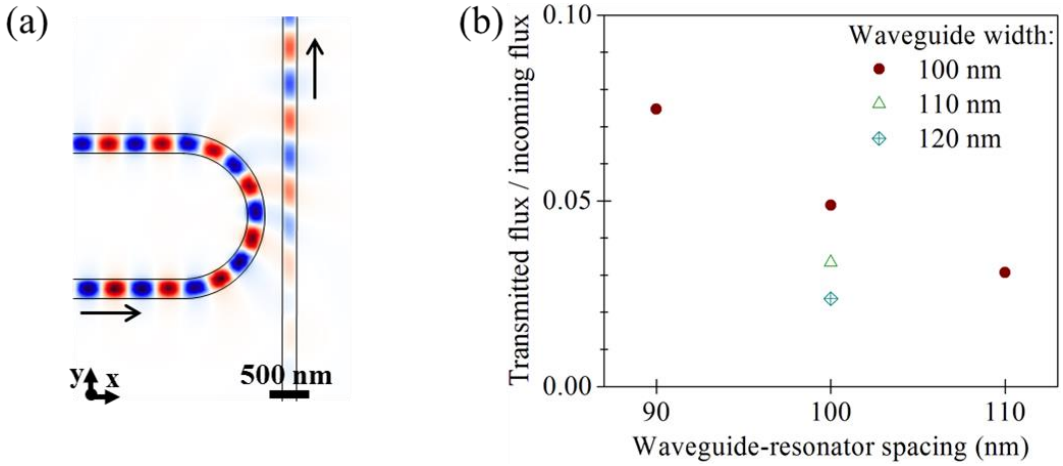

Fig. 5.1.1: 3-D FDTD simulation to determine transmission characteristics between 120 nm wide, 200 nm high GaP ring waveguide (2 μm diameter) and adjacent waveguides with different widths placed on a diamond substrate. (a) Top view onto electric field distribution in coupled waveguide structures (H_z). The width of the straight waveguide is 100 nm, the separation between the two structures is 100 nm. The ring waveguide was excited with a Gaussian source (centered at 637 nm) placed into the lower arm of the structure. The cut plane is in the center of the GaP device layer. (b) Ratio of flux transmitted into the straight waveguide vs. incoming flux in ring waveguide as function of the waveguide-resonator spacing for different waveguide widths.

whispering-gallery-modes in the GaP layer, thereby improving the device characteristics. In these simulations, a source is placed a in the ring waveguide and the flux coupled into the straight waveguide is measured. The ring waveguide is excited with a quasi-TE polarized Gaussian pulse centered at 637 nm. Fig. 5.1.1(b) shows the fraction of flux coupled from the ring resonator to the straight waveguide for different waveguide widths and various waveguide-resonator spacings. The fraction of the transmitted flux increases for smaller resonator-waveguide spacings and smaller waveguide widths. Smaller gaps allow for larger spatial overlap of the resonator and waveguide modes. Smaller waveguide widths allow for better matching of the spatial period between the curved and the straight waveguide due to their reduced effective index and, hence, longer mode wavelength [138]; for waveguide widths above 140 nm, coupling of higher-order modes is observed. For a 2 μm disk resonator with an intrinsic, realistic quality factor Q_i of 10^4, corresponding to a round trip loss of ~ 2%, critical coupling can be achieved with a resonator-waveguide spacing of 100 nm and a waveguide width of 120 nm. Critical coupling can also be achieved with a smaller (larger) waveguide width and larger (smaller) separation.

5.2 Adaption of EBL and dry etch processes for fabrication of GaP coupled photonic structures on diamond

3-D FDTD simulations indicate the best coupling characteristics for waveguide-resonator spacings of 100 nm or less. Furthermore, the GaP grating structures for out-of-plane coupling require narrow trenches (~ 150 nm wide) for efficient operation (see Appendix B). When attempting to realize these structures utilizing the fabrication process developed for the resonator arrays, several challenges emerged: (i) small features appeared undercut after the ICP-RIE, and the lithography process was hindered by (ii) the resist properties as well as by (iii) the small size

of the diamond substrates. Hence, extensive engineering of the etch and EBL processes was necessary for the realization of coupled GaP resonators and waveguides on diamond.

The etch parameters that were utilized for the fabrication of the free-standing structures in the previous chapters caused severe undercutting during etching of narrow GaP trenches. Fig. 5.2.1(a) shows etch results for a 100 nm period test structure (left) and a GaP disk next to a waveguide (right), both etched in GaP bulk material. The ICP-RIE employs Cl_2 as the chemical etch component and Ar as the mechanical agent for sputtering of the GaP material (Fig. 5.2.1(b)) [139]–[141]. Undercutting in the narrow trenches indicates reduced mass-flow of the unreacted Cl_2 species, which can then react with the remaining GaP. Since a reduction of the Cl_2 flow is not possible due to instrument limitations, the ICP power is reduced to limit the density of the Cl_2 species while still ensuring etching of the GaP substrate. Additionally, the Ar flow rate and radio-frequency (RF) power are increased to ensure more anisotropic etching of the trenches, and the chuck is cooled below room temperature. Test structures etched with the improved parameters are shown in Fig. 5.2.2. The 100 nm periodic grating structures show anisotropic sidewalls with an outward slope of ~ 85° (left panel). The gaps between the waveguide and resonator structures displayed in the right panel of Fig. 5.2.2 appear uniformly etched with the etch rate in the trenches only slightly lower than the etch rate in the free-standing GaP areas. This is important to prevent resist degradation due to physical sputtering, which becomes more pronounced for longer etch times.

Hydrogen silsesquioxane (HSQ) is employed as electron beam resist due to its improved line edge roughness (LER) and higher etch resistivity compared to polymer resists [142], [143]. HSQ is a negative tone resist that turns into silica upon exposure to electron radiation, and it can be further densified by thermal treatment [144], [145]. However, its adhesion to substrates other

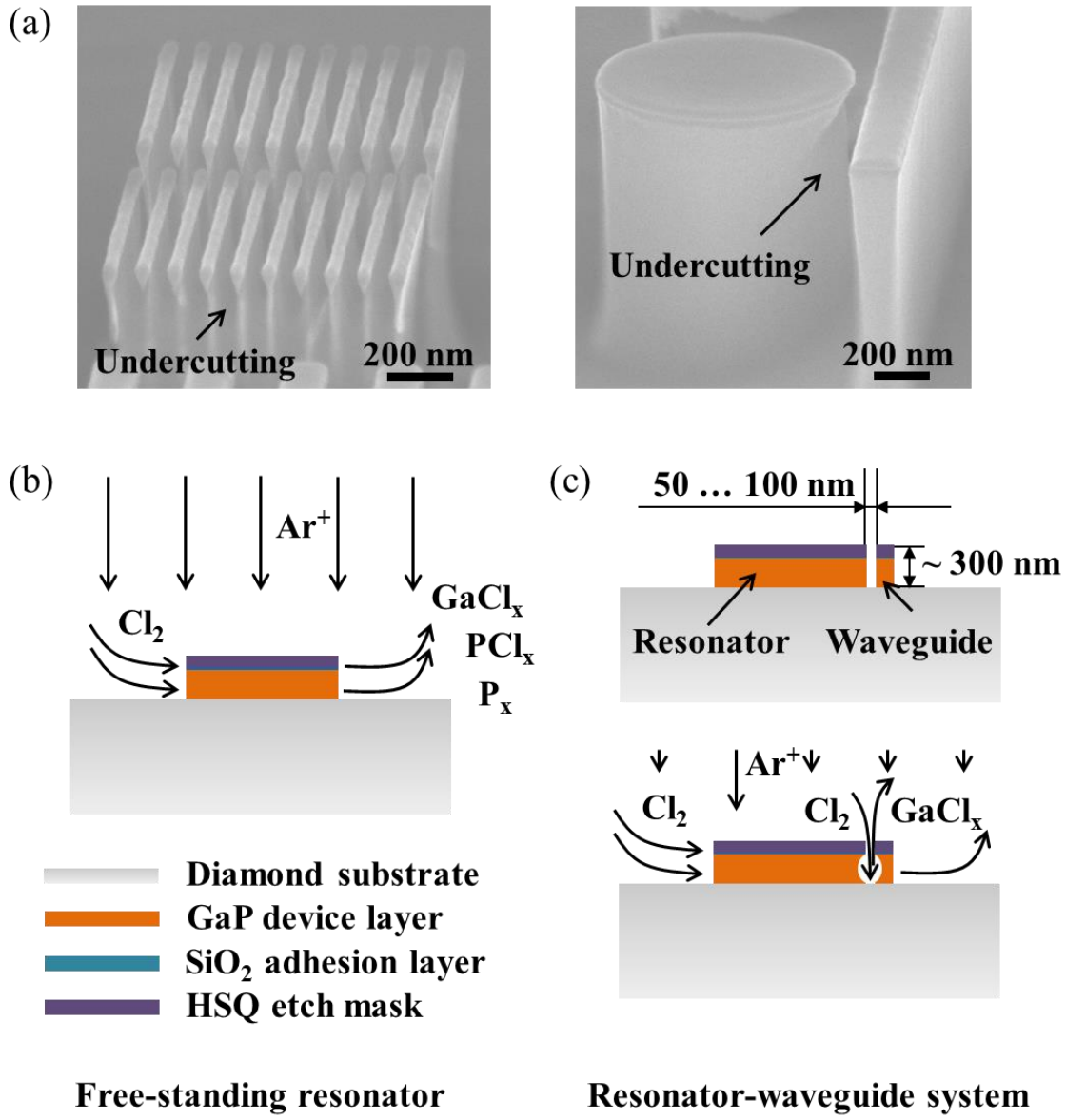

Fig. 5.2.1: ICP-RIE etching of narrow structures on bulk GaP. (a) SEM micrographs showing severe undercutting in regions with narrow device structures after the Cl_2/Ar dry etch. (b) Schematic of etch process for free-standing GaP disk resonator. While Ar provides for physical etching of the compound layer, Cl_2 chemically etches the dielectric. (c) Etch conditions for resonator-waveguide coupled GaP structures on diamond. Isotropic etch behavior is observed in narrow device structures, indicating the chemical etching contributions to be enhanced in the trenches. With open areas exhibiting predominantly straight sidewalls, this points to a mass-flow limited chemical reaction process in the narrow trenches. An improvement of the etch characteristics is therefore expected for a reduction of the chemical etch component and increase of the physical Ar sputter etching.

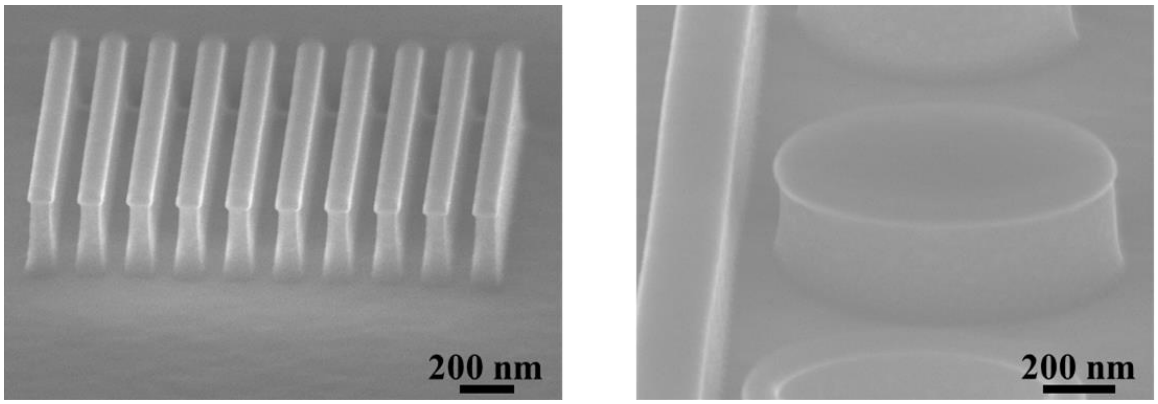

Fig. 5.2.2: Improved ICP-RIE etch conditions for fabrication of coupled GaP waveguide-resonator structures on diamond. The efficiency of the Ar sputter etching of the III-V compound is enhanced, while the chemical Cl_2 etch is limited. SEM micrographs showing results of bulk GaP dry etching for test structures with periodic 100 nm spacing (left panel) and waveguide-resonator gaps (right panel). The sidewall slope is ~ 85°.

than Si and SiO_2 is limited, and common adhesion promoters, such as hexamethyldisilazane (HMDS), are not effective. Fig. 5.2.3(a) shows a SEM of HSQ resist structures after development with failing adhesion. A 10 nm SiO_2 layer deposited on the GaP by plasma-enhanced chemical vapor deposition (PECVD) is found to be an effective adhesion layer (Fig. 5.2.3(b)). Another challenge is spinning a uniform coat of resist on the mm^2-sized square diamond substrates. While HSQ resist spins to a thickness of ~ 80 nm in the center of the

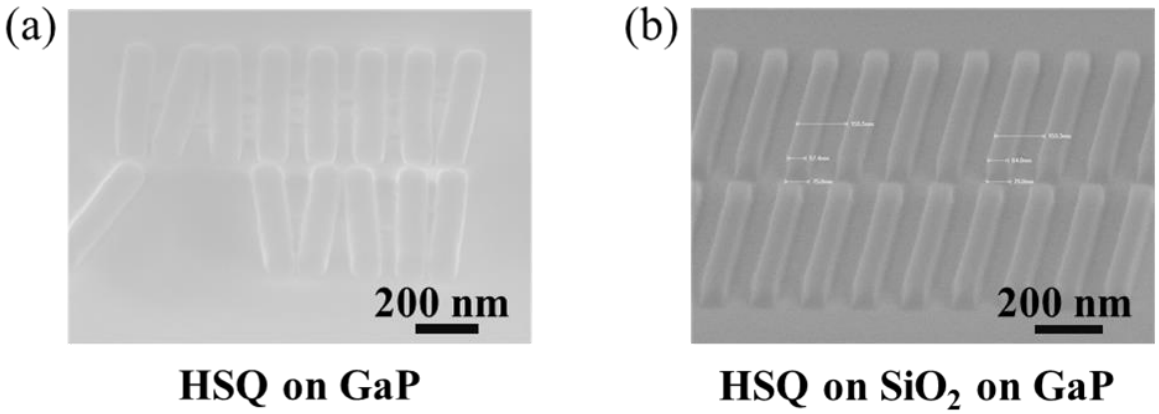

Fig. 5.2.3: Employment of PECVD SiO_2 for enhanced adhesion of HSQ to GaP. (a) HSQ test structures on GaP after development in TMAH showing limited adhesion of the resist to the substrate. (b) HSQ test structures after deposition of a 10 nm SiO_2 PECVD adhesion layer and electron beam lithography processing.

diamond substrate, a significant edge bead limits the usable area in the center of the diamond substrate to < 1 mm^2 using the processing conditions recommended by the manufacturer. While the edge bead can be limited in larger square substrates by reducing the leading edge drop, e.g. in a recessed chuck, this is not found to be effective for these substrates. Instead, the acceleration between the spread and the spin step is significantly increased to enhance the spin-off.

5.3 Final process flowfor waveguide-integrated GaP resonators on mechanical-grade diamond

Waveguide-integrated GaP resonators on diamond are fabricated from single-crystalline GaP sheets transferred via epitaxial lift-off and van der Waals bonding to diamond. A mechanical-grade CVD diamond substrate (ElementSix, N < 1 ppm) is utilized for these experiments as it provides a cost-effective alternative for a proof-of-principle demonstration of functional hybrid GaP\diamond optical networks. Electronic-grade diamond substrates will be required as host material for near-surface NV^- centers in future device generations. Fig. 5.3.1 illustrates the process flow for the implementation of the coupled devices (see Appendix A). After bonding and cleaning of the mm^2-sized GaP sheet, the SiO_2 resist adhesion layer is deposited via PECVD. HSQ resist is processed and patterned in a 100 kV JEOL JBX-6300FS EBL system. The GaP layer is etched with the improved Cl_2/Ar ICP-RIE process. After initial testing of the devices, the device structures are extended into the diamond substrate by an O_2 etch.

Ring and disk resonators with diameters of 1, 2, and 5 μm, and waveguides with both 100 and 120 nm widths are defined. The SEM image in Fig. 5.3.2 shows a device array with the different resonators next to waveguides, taper regions and grating couplers on the etched diamond substrate; with the lighter areas being the GaP devices and the darker gray the diamond substrate. The HSQ layer remains on the GaP during testing.

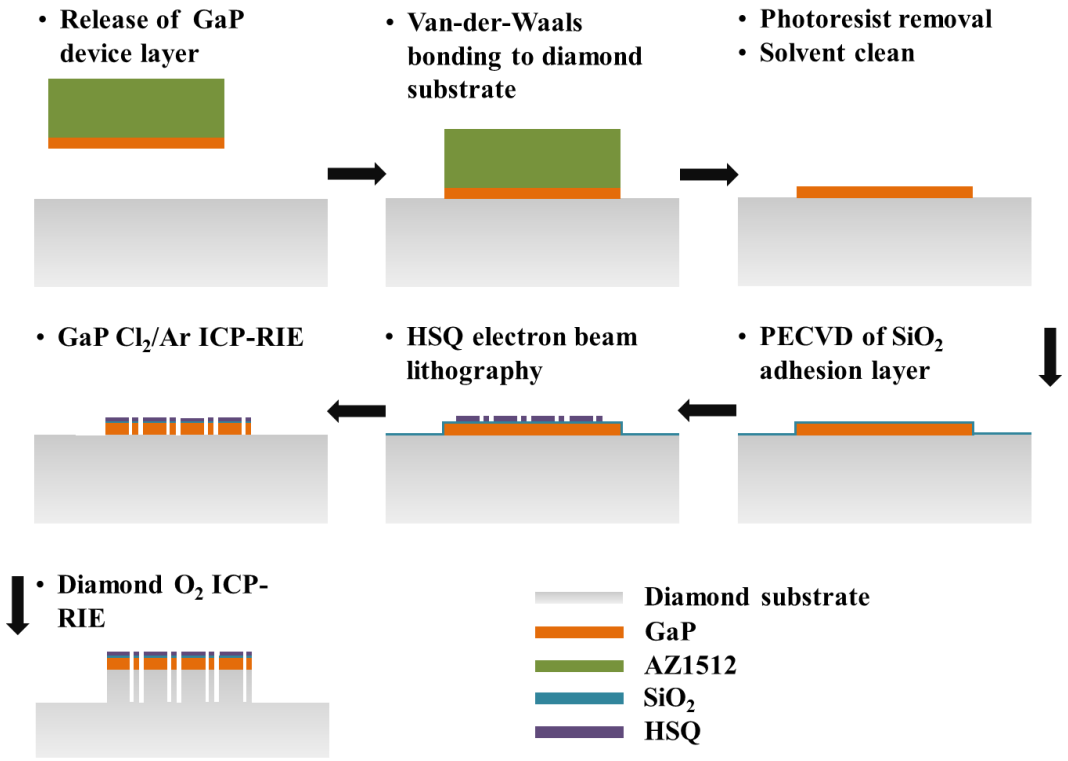

Fig. 5.3.1: Schematic process flow for fabrication of GaP photonic networks on diamond. After transfer and bonding of the GaP device layer with the photoresist as mechanical support, the resist is removed in hot 1165 resist remover, followed by a solvent clean. An SiO_2 adhesion layer is deposited vie PECVD, followed by an HSQ resist spin, electron beam exposure and resists development in 25% TMAH. The patterned GaP is then dry etched in a Cl_2/Ar atmosphere. An O_2 dry etch of the diamond substrate finalizes the processing. The HSQ remains on the devices during test. SEM inspection and profilometry were carried out after electron beam lithography, and each etch step to determine resist thickness and etch depths, respectively.

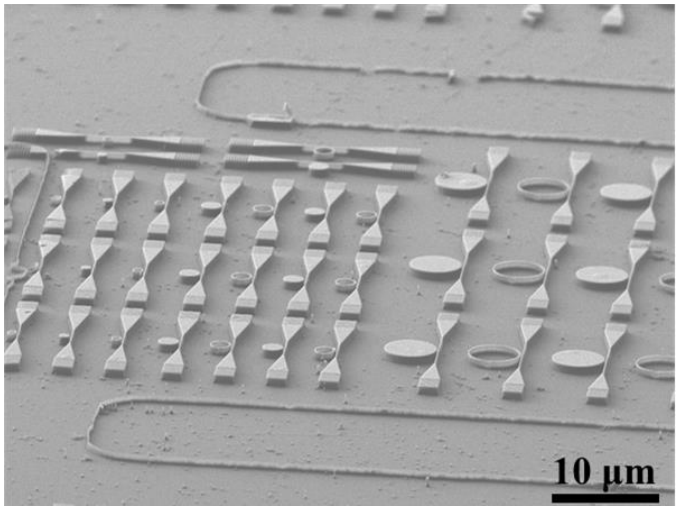

Fig. 5.3.2: Fabricated GaP device array on diamond with 1 µm, 2 µm and 5 µm ring and disk resonators adjacent to GaP waveguides with integrated tapers and out-off-plane grating couplers.

5.4 Waveguide-coupled single-crystalline GaP disk resonators on mechanical-grade diamond

As will be discussed in the section 5.5, the potential photon coupling efficiencies in integrated GaP\diamond networks are determined by the intrinsic quality factors and coupling characteristics between a resonator and an adjacent waveguide. To evaluate the performance of the fabricated structures, passive broadband transmission measurements are carried out to extract their loaded quality factors. Coupling between the resonators and waveguides becomes apparent through dips in the transmission spectra at the respective resonance wavelengths of the devices; this indicates the presence of whispering-gallery-modes in the resonators. The center wavelength and the *FWHM* of these transmission dips determine the loaded quality factor, Q_l. The depth, or contrast, of the transmission dip offers further information about the coupling behavior: a contrast of 100% indicates critical coupling between the waveguide and the resonator, i.e. $Q_i=Q_c$.

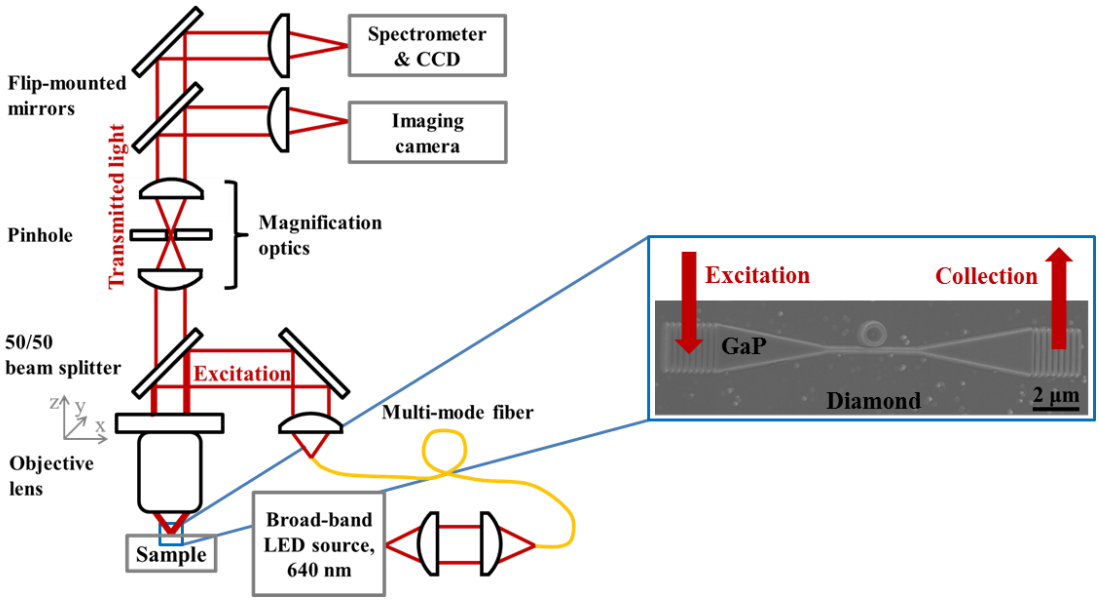

Fig. 5.4.1: Transmission measurements on hybrid GaP/diamond waveguide-coupled resonator structures. A broad-band LED light source is focused on the grating structure. The light transmitted through the waveguide is collected through the pinhole aligned to the second grating coupler. The transmission spectrum is recorded with a spectrometer.

The structures are excited through the out-of-plane grating couplers (Fig. 5.3.3): a broad-band LED source (centered at 640 nm) is fiber-coupled and focused on one of the gratings, the transmitted signal is collected through the same lens at the second, output grating and guided to either a CCD camera for visual inspection or a spectrometer for analysis of the coupling characteristics.

Initial measurements on devices on the pristine diamond substrate show resonance modes in disks with diameters ≥ 2 μm. A 2 μm disk resonator device is shown in Fig. 5.3.4, with its respective broad-band transmission spectrum displayed in Fig. 5.3.5. The top panel displays the spectrum recorded with a 300 grooves/mm grating. Transmission dips are visible at 618.5 nm, 636.4 nm, and 655.8 nm. With an expected *FSR* of ~ 19 nm, this confirms the appearance of whispering-gallery-modes in this device. The low-frequency oscillations visible in the spectrum are caused by Fabry-Perot interference along the waveguide.

The loaded quality factors Q_l are extracted from higher-resolution spectra collected with a 1800 grooves/mm grating (bottom panel, Fig. 5.4.3). A Lorentzian line-fit is employed to determine resonance wavelength and *FWHM* of the transmission dips. A $Q_{l,max}$ of ~ 3,700 can be

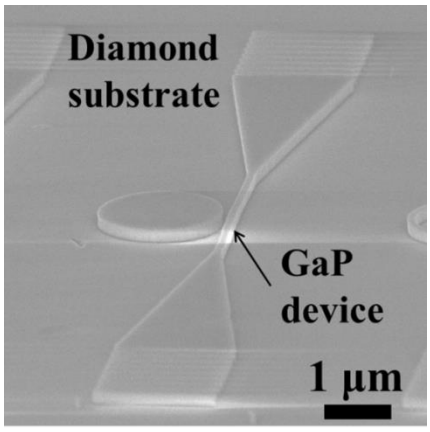

Fig. 5.4.2: Scanning electron micrograph of 2 μm GaP disk resonator on diamond integrated with a 100 nm wide waveguide and out-of-plane grating coupler structure.

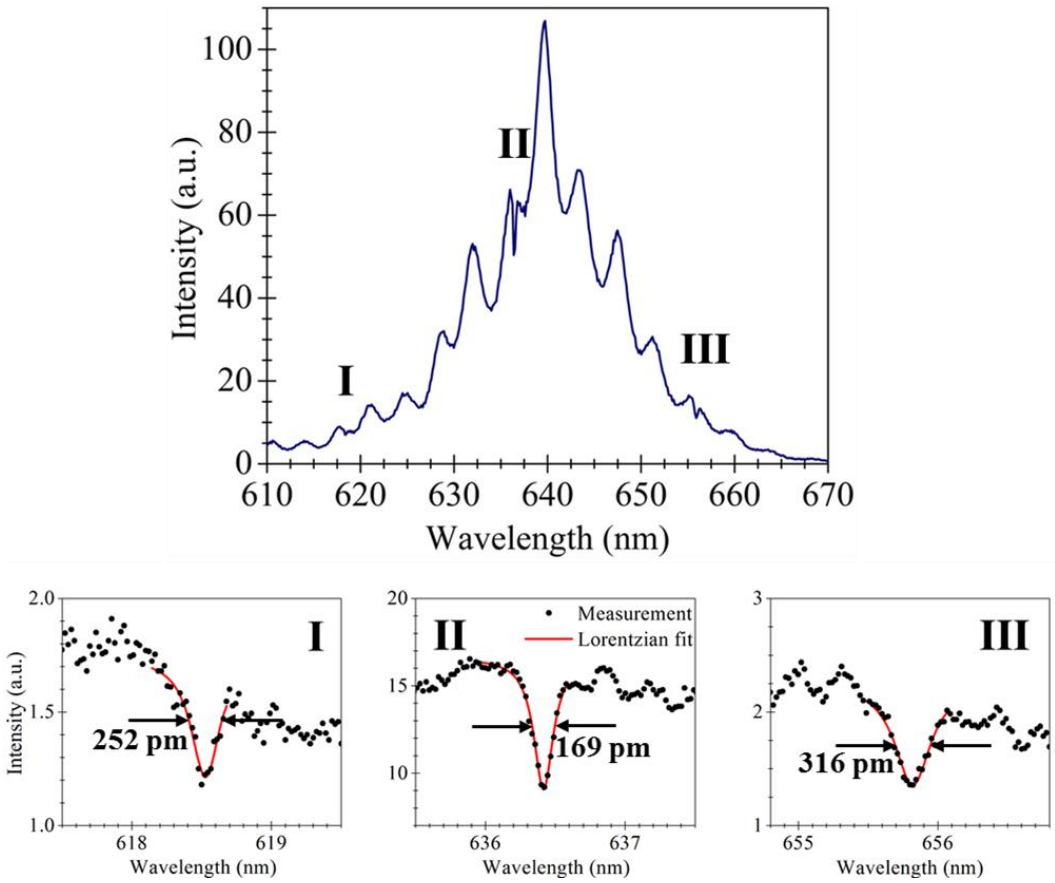

Fig. 5.4.3: Transmission spectrum measured for the device shown in Fig. 5.4.2. The spectrum in the top graph was recorded using a 300 grooves/mm grating. The spectrum shows 3 transmission dips with a *FSR* of ~ 19 nm. The low-frequency oscillations are caused by Fabry-Perot interferences along the length of the GaP waveguide. The bottom graphs, recorded with a 1800 grooves/mm grating, show the transmission dips with their respective Lorentzian line- fits to extract the *FWHM* and loaded quality factor Q_l. The maximum Q_l is 3,700.

extracted for the resonance at 636.4 nm. The corresponding dip is ~ 40%. The simulated Q_i of a 2 μm disk resonator device on diamond is ~ 6,650 for a TE resonance at 640.2 nm (Fig. 5.4.4, left). With the $Q_{l,max} > ½\ Q_{i,simulated}$, the devices are under-coupled.

Quasi-2-D cylindrical FDTD simulations of devices with the sidewalls extended 600 nm into the diamond substrate show significantly enhanced theoretical $Q_i > 2 \cdot 10^{10}$ (Fig. 5.4.4, right panel). Partial removal of the relatively high-index substrate results in better confinement of the optical mode in the GaP device layer [29], [30]. FDTD simulations of 1 μm diameter GaP

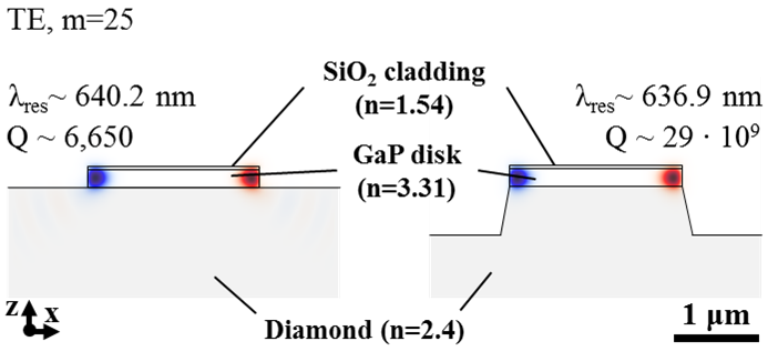

Fig. 5.4.4: Quasi-2-D FDTD simulation of 2 µm GaP disk resonator TE resonance on intrinsic (left) and 600 nm etched (right) diamond substrate. The intrinsic quality factor of the device increases significantly on the etched substrate due to better confinement of the optical mode in the disk resonator. The simulated structures are replicated from actual device structures, with a 40 nm thick HSQ layer remaining after fabrication.

devices also indicate resonance modes to appear if placed on etched diamond pedestals. Hence, the diamond substrate is etched with the resonators, waveguides and grating couplers forming the etch mask. Fig. 5.4.5 displays a SEM image of a 1 µm GaP disk resonator on the 550 nm etched diamond substrate and the adjacent waveguide the device couples to. The gap between the disk and the waveguide is ~ 75 nm. The broad-band transmission spectrum for this device is shown in Fig. 5.4.5 with a single transmission dip visible at 643.5 nm. The FSR for a 1 µm device is ~ 40

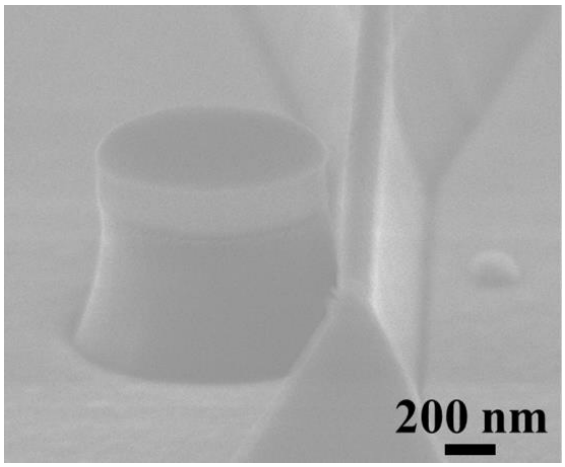

Fig. 5.4.5: SEM micrograph of 1 µm GaP disk resonator next to GaP waveguide on 550 nm deep etched diamond substrate. The resonator-waveguide spacing is ~ 75 nm.

nm; hence, only one resonance can be observed within the bandwidth of the light source. The high-resolution spectrum (Fig. 5.4.5, top right) reveals the doublet structure of the resonance. This can be caused by surface roughness or fabrication imperfections, thus resulting in non-degenerate modes [146], [147]. The loaded $Q_{l,max}$ of the device, extracted with a dual- peak Lorentzian fit, is ~ 3,800, again with a dip of ~ 40%. A quasi-2-D FDTD simulation of a 1 μm diameter disk on 550 nm etched diamond with sloped sidewalls shows a $Q_i > 3 \cdot 10^6$ for a TE resonance (Fig. 5.4.6, bottom right). The same disk on the pristine, non-etched diamond substrate only shows a Q_i of ~ 200.

The measured Q_l are significantly lower than the simulated intrinsic Q_i. This points to over-coupling of the resonator structures as well as a limitation of the real intrinsic quality factor due

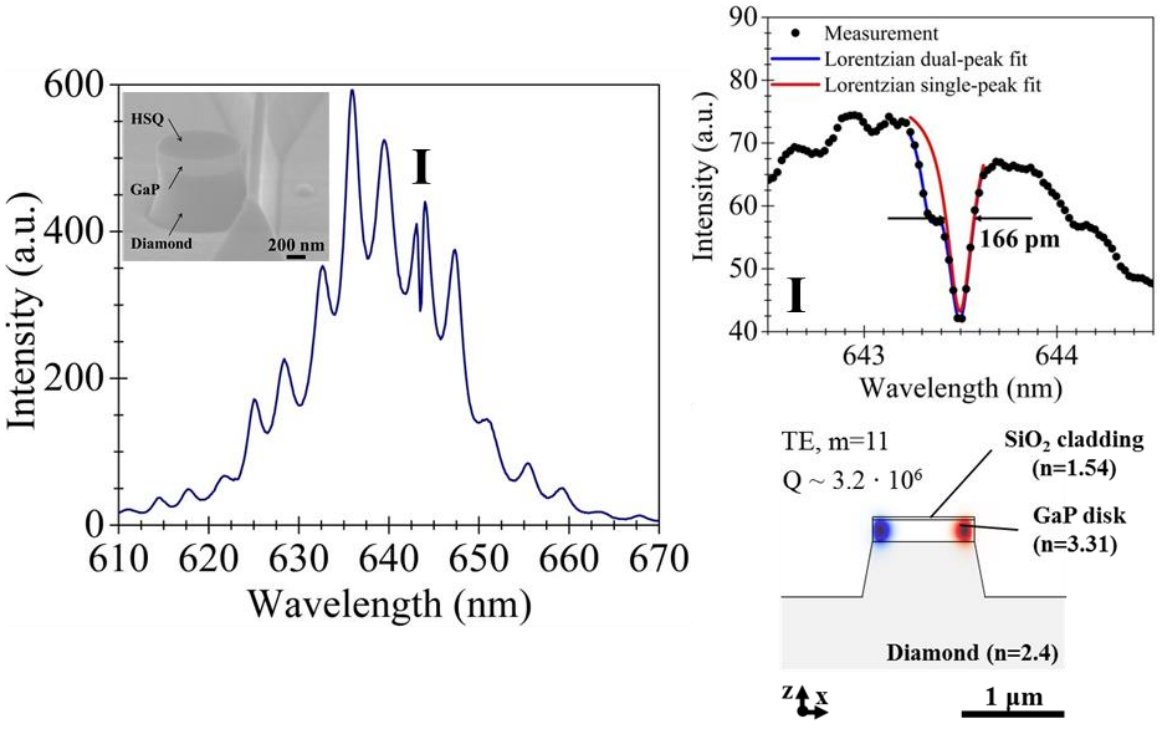

Fig. 5.4.6: Transmission spectrum measured for a waveguide-coupled 1 μm GaP disk resonator on diamond. A resonance at 643.5 nm is observed. The broad-band spectrum in the left panel is recorded using a 300 grooves/mm grating. The loaded quality factor of the devices is ~ 3,800, measured with a 1800 grooves/mm grating (upper right graph). The quasi-2D FDTD simulation show the electric field distribution for a device geometry similar to the one observed in Fig. 5.4.5, with a theoretical Q_i of > $3 \cdot 10^6$.

to fabrication and material imperfections, which can cause absorption and rough sidewalls, thereby scattering losses and lower Q_i [71], [147]. The coupling behavior of this device is studied by 3-D FDTD simulations of the loaded quality factor Q_l. The simulations suggest a coupling Q_c of ~ 6,000 for the 1 μm disk placed next to a 120 nm waveguide with a 75 nm gap between them. This indicates that the device is indeed over-coupled, and possesses an estimated intrinsic $Q_{i,min}$ of ~ 10^4.

5.5 Evaluation of device performance with respect to a future integration with near-surface NV^- centers in diamond

To evaluate the performance of the fabricated structures for collection and on-chip routing of NV^- ZPL photons in a hybrid GaP\diamond network, we introduce a benchmark based on the efficiency of each coupling step in a coupled GaP waveguide-resonator system integrated with NV^- defects in diamond for the assessment of the overall photon coupling efficiency. The probability of entanglement generation rate between two NV^- electron spins scales with η^2, η being the NV^- ZPL detection efficiency. Efficient collection of the NV^- ZPL in a bus waveguide requires strong Purcell enhancement in small-sized resonators with high quality factors as well as efficient coupling of the NV^- ZPL into the cavity and further into the waveguide. The overall ZPL-waveguide coupling efficiency $\eta_{NV\text{-}WG}$ can be described by:

$$\eta_{NV-WG} = \eta_{ZPL} \cdot \beta_{ZPL} \cdot \eta_{CAV-WG} \qquad \text{Eq. 5.3}$$

where η_{ZPL} is the fraction of NV^- ZPL emission over the total NV^- emission, β_{ZPL} the fraction of the NV^- ZPL coupled into the cavity, and $\eta_{CAV\text{-}WG}$ the fraction of the resonator field coupled to the waveguide. η_{ZPL} is defined by:

$$\eta_{ZPL} = \frac{\gamma_{ZPL}(F_{ZPL}+1)}{\gamma_{PSB}+\gamma_{ZPL}(F_{ZPL}+1)} \qquad \text{Eq. 5.4}$$

where γ_{ZPL} and γ_{PSB} are the spontaneous emission rates into the ZPL and the phonon sideband (PSB), respectively. In bulk diamond, γ_{ZPL}/γ_{NV} ~ 3% [43], [44], i.e. only a small fraction of the total NV^- emission γ_{NV} is into the ZPL. If the defect is located in the field of an optical cavity, however, the total emission rate into the ZPL can be enhanced by the Purcell factor F_{ZPL} [19]. Under weak coupling, the enhancement of the ZPL emission rate in the field of a hybrid GaP/diamond resonator coupled to a waveguide is given by [30]:

$$F_{ZPL} = \frac{3}{4\pi^2}\left(\frac{\lambda_{ZPL}}{n_{GaP}}\right)^3 \frac{n_{GaP}}{n_{diamond}} \frac{Q_l}{V}\left(\frac{|\hat{\mu}\cdot \boldsymbol{E}_{NV}|}{|\boldsymbol{E}_{max}|}\right)^2 \quad \text{Eq. 5.5}$$

where $\hat{\mu}$ is the NV^- dipole unit vector, $\boldsymbol{E}_{NV}$ the local electric field at the NV^- site, and $\boldsymbol{E}_{max}$ the maximum cavity field.

The fraction of the ZPL coupled into the cavity is further determined by the Purcell factor:

$$\beta_{ZPL} = \frac{F_{ZPL}}{F_{ZPL}+1} \quad \text{Eq. 5.6}$$

The coupling efficiency between the cavity and waveguide is given by:

$$\eta_{CAV-WG} = \frac{\gamma_{WG}}{\gamma_{total}} = \frac{Q_l}{Q_c} = \frac{Q_i}{Q_i+Q_c} \quad \text{Eq. 5.7}$$

with γ_{WG} the decay rate into the waveguide and γ_{total} the total cavity decay rate, assuming no scattering losses in the system. The total fraction of the NV^- emission coupled as ZPL photons into the bus waveguide is then:

$$\eta_{ZPL-WG} = \frac{\gamma_{ZPL}}{\gamma_{PSB}+\gamma_{ZPL}(F_{ZPL}+1)} \cdot F_{ZPL} \cdot \frac{Q_i}{Q_i+Q_c} \quad \text{Eq. 5.8}$$

where the coupled field travels in both directions along the length of the waveguide. This expression can be employed to evaluate the performance of the current device structures for the efficient collection of near-surface NV^- ZPL photons.

The Purcell factor (Eq. 5.5) for the 1 μm diameter disk resonator device can be estimated from the measured loaded quality factor Q_l ~ 3,800 and whispering-gallery-mode volumes and electric field components extracted from 3-D FDTD measurements of the device. The simulated mode volume V is ~ 0.025 μm^3 (~ $3.5(\frac{\lambda}{n})^3$). This indicates a standing wave in the structure [71]. For a NV$^-$ center located 15 nm below the diamond surface, the ratio of the local field strength to the maximum cavity field $(|\boldsymbol{E}_{NV}|/|\boldsymbol{E}_{max}|)^2$ is ~ 0.16; SRIM simulations of a 10 kV implantation of N^+ into diamond suggest the peak distribution to be located ~ 14 nm below the surface [104]. With the assumptions of optimal alignment of the NV$^-$ dipole with the cavity electric field and the defect located in an anti-node of the quasi-TE standing wave, a Purcell enhancement factor of ~ 18 can be estimated for the NV$^-$ ZPL emission.

This theoretical factor represents an upper bound, and is currently hindered by limited control over the spatial orientation of the NV$^-$ in the diamond lattice. Ion implantation processes can create defects in defined locations and at closely defined depths in the diamond substrate [50], [52], [55], [104]. Incorporation of the optical defects during diamond CVD growth also allows for control over the NV$^-$ depth [54], [55], and recently progress has been made toward the integration of defects with preferential alignment in the diamond lattice [57], [148]–[150]. While research is underway to control the lateral placement of NV$^-$ defects introduced in the substrate during the CVD growth [56], a single defect – with optimal dipole alignment, coupling to the cavity and Stark-tuned onto the cavity resonance – could also be selected from the large number of NV$^-$ present after CVD treatment [151]–[153].

The overall potential ZPL collection efficiency in the waveguide coupled to the 1 μm diameter disk resonator is estimated from Eq. 5.8. With γ_{ZPL}/γ_{NV} ~ 3%, F_{ZPL} ~ 18, Q_i ~ 10^4, and Q_c ~ 6,000, $\eta_{ZPL\text{-}WG}$ ~ 22%, which corresponds to 11% coupling in each direction of the

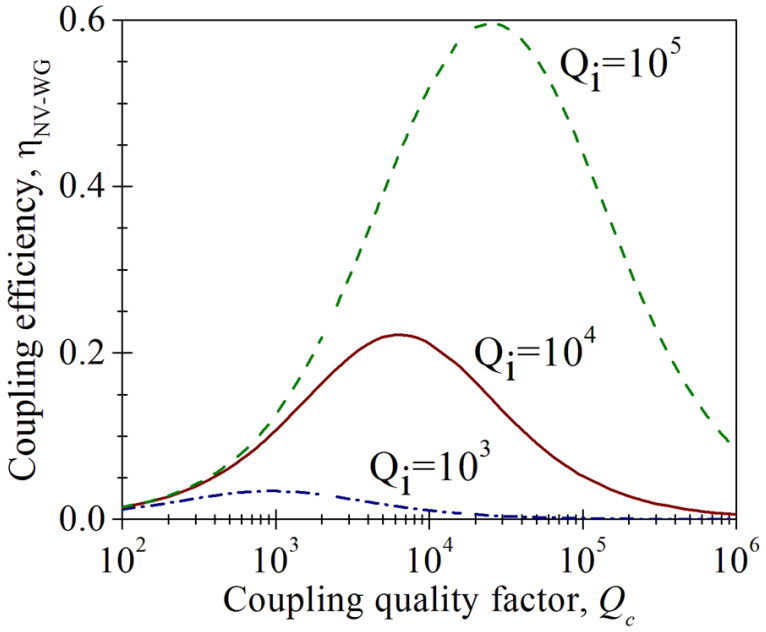

Fig. 5.5.1: Efficiency of NV^- ZPL photon collection in GaP waveguide coupled to disk resonator as function of intrinsic and coupling quality factor. While the maximum collection efficiency for devices with low intrinsic quality factors can be obtained close to critical coupling, devices with higher Q_i exhibit maximum efficiencies in the over-coupled regime.

waveguide. The theoretical collection efficiencies for the NV^- ZPL emission coupled into a 1 μm GaP disk resonators and adjacent waveguide as function of both the resonator intrinsic quality factor Q_i and coupling quality factor Q_c are plotted in Fig. 5.5.1. For $Q_i \sim 10^4$, the maximum expected coupling efficiency is 22%. Hence, the device performs with the maximum collection efficiency attainable for its intrinsic quality factor.

The waveguide collection efficiencies are improved for devices with higher intrinsic quality factors. For a Q_i of $\sim 10^5$, the maximum ZPL coupling efficiency is ~ 60%. Devices with lower Q_i show more efficient photon collection close to critical coupling. In contrast, high-Q_i devices operate with maximum efficiencies in the over-coupled regime. A balance must be met between Q_c limiting either the Purcell enhancement of the ZPL emission or the efficiency of the resonator-waveguide coupling. This coupling quality factor Q_c is determined

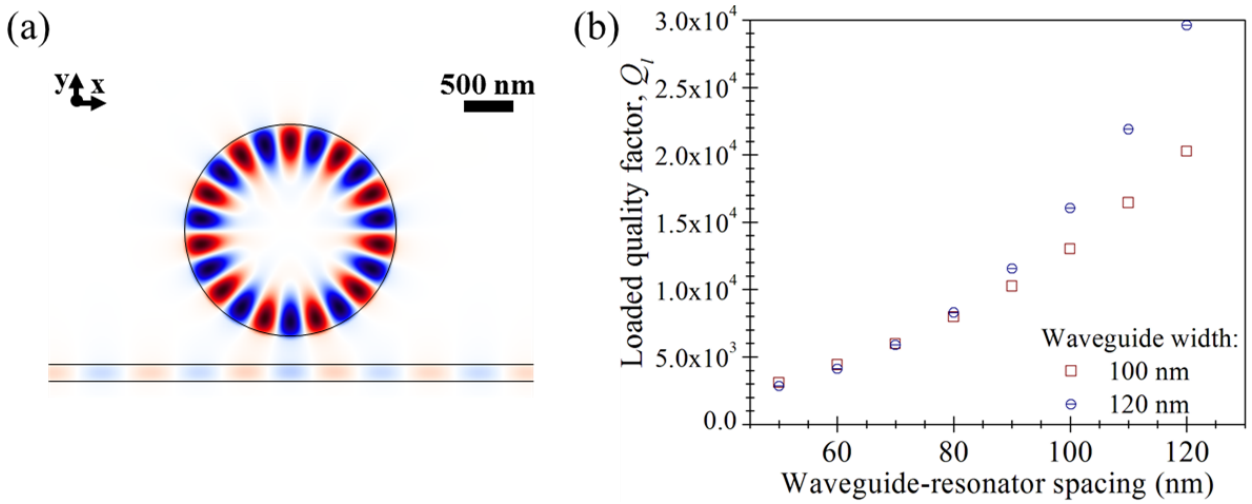

Fig. 5.5.2: Coupling characteristics between GaP waveguide and 1 μm GaP disk resonator. (a) Cross-sectional electric field distribution (H_z) for device with 100 nm wide waveguide and 100 nm waveguide-resonator separation showing phase-matched coupling between both structures for quasi-TE excitation. (b) 3-D FDTD simulation output of Q_l vs. waveguide-resonator spacing for different waveguide widths. With $Q_i > 3 \cdot 10^6$, the loaded quality factor is mainly determined by Q_c.

by the waveguide-resonator spacing and the waveguide width. A $\eta_{ZPL\text{-}WG} > 18$ % can theoretically be achieved by a Q_c ranging between 2,500 to $1.6 \cdot 10^4$. Within this range, the optical circuit is appreciable over- and under-coupled.

3-D FDTD simulations are employed to explore the impact of fabrication tolerances on the ZPL collection efficiencies. The loaded quality factors Q_l are determined for a 1 μm diameter GaP disk resonator when coupled to waveguides with 100 nm and 120 nm widths, respectively, separated from the resonators by 50 nm to 120 nm. Fig. 5.5.2(a) illustrates the phase-matched coupling of the 637 nm excitation over a gap of 100 nm to a 100 nm wide waveguide. Fig. 5.5.2(b) displays the simulated loaded quality factors for both waveguide widths as function of the separation between the resonator and waveguides. The resonator shows a Q_i of $3 \cdot 10^6$; hence, Q_l is mainly determined by Q_c. With the Q_l from Fig. 5.5.2(b), the overall NV- photon collection efficiency remains above 18% for resonator-waveguide gaps between 50 nm and 100 nm, for

either waveguide width. Therefore, small fabrication non-uniformities for the waveguide widths and gaps between the structures are not expected to greatly affect their overall performance.

5.6 Outlook for large-scale single-crystalline GaP optical networks integrated with NV^- centers in diamond

This chapter discusses novel single-crystalline GaP resonators integrated with waveguides and grating couplers on a mechanical-grade diamond substrate. The devices are fabricated from epitaxial GaP sheets transferred onto the diamond substrate using the epitaxial lift-off approached introduced in chapter 4. This is the first demonstration of hybrid coupled optical devices on diamond with linear EO properties which, in the future, could enable the integration of active functional device capabilities.

The properties of the fabricated devices lend themselves toward an efficient collection and coupling of NV^- ZPL photons from the diamond substrate to a bus waveguide. With the currently achieved quality factors, a theoretical maximum of 22% of the photons emitted by an NV^- and coupled to a resonator can be collected as ZPL emission in an adjacent waveguide. This is a significant increase over the 0.3% collection efficiency achievable with solid immersion lenses [62], [63]. The collection efficiencies are expected to be enhanced further with an increase in the intrinsic cavity quality factor Q_i. This can be achieved by improved fabrication conditions. 4 μm diameter MBE GaP disks in air with $Q_i > 28 \cdot 10^4$, for example, have been demonstrated using a resist reflow approach [154]. While a reflow approach may not be suitable for the narrowly defined device dimensions for efficient waveguide-resonator coupling, a further reduction of the resist LER [144], [155] or utilization of a hard mask to prevent mask degradation for improved sidewall roughness and therefore less scattering loss may be possible. If integrated in large networks, simulations suggest that small variations in the waveguide-resonator spacing or waveguide width should not critically affect the collection efficiencies for different devices.

Single-crystalline waveguide-integrated GaP resonators on mechanical-grade diamond show promising qualities for the efficient routing of NV^- photons in an integrated hybrid network. Hence, in the next chapter we present the results of integrating these networks with near-surface NV^- centers in diamond to explore the possibility of coupling between the defects and a hybrid GaP\diamond network.

Chapter 6:

Off-chip coupling of the NV^- ZPL in a hybrid GaP\diamond photonic network

One outstanding challenge in the integration of NV^- defects with hybrid GaP\diamond optical networks is the collection of the NV^- ZPL emission in a resonator structure and subsequent coupling to waveguides for on-chip routing. Thus far, Purcell enhancement of the NV^- emission in single GaP\diamond resonators fabricated by an probabilistic drop-down approach, resulting in devices being randomly located on the diamond substrate, has been accomplished [30]. Coupling of the NV^- PSB emission to an array of GaP disk resonators fabricated in a deterministic fashion was demonstrated in section 4.3. Waveguide-integrated single-crystalline GaP resonators on diamond were presented in chapter 5.

In this chapter, near-surface NV^- defect centers in diamond are now integrated with single-crystalline GaP disk resonators coupled to waveguides and out-of-plane grating couplers. The exact resonance wavelength of integrated cavities cannot be controlled deterministically due to fabrication tolerances; hence, a resonance tuning technique is employed to overlap the cavity mode frequency with the NV^- spectral line. This enables collection of the ZPL emission in the cavity, further coupling to an adjacent waveguide for routing to a grating coupler, and final off-chip detection. The performance of the hybrid GaP\diamond network is analyzed and finally, challenges in the future implementation of large-scale hybrid GaP\diamond networks integrated with near-surface NV^- centers are discussed.

6.1 Integrating near-surface NV^- centers with hybrid GaP\diamond device structures

For the integration with near-surface NV^- centers, the hybrid GaP\diamond resonator devices coupled to waveguides and grating couplers are fabricated on a diamond substrate prepared with the near-surface defects: the NV^-s are created in an electronic-grade CVD diamond substrate (Element6) using the low-energy ion implantation (10^{10} cm^{-2},10 kV) and annealing process described in section 3.1. The GaP substrates (provided by Y. Song and M. L. Lee, Yale University, CT) are prepared using molecular beam heteroepitaxy from solid P_2 and Ga sources: a 800 nm aluminum gallium phosphide ($Al_{0.8}Ga_{0.2}P$) sacrificial layer and 150 nm GaP device layer are grown on pieces cleaved from a single-crystalline (001) GaP wafer (Crystec). The epitaxial lift-off process described in section 4.2.2 is utilized to transfer the 150 nm thick GaP sheet onto the diamond substrate prepared with the near-surface NV^- centers.

Waveguide-integrated disk resonators are fabricated as outlined in section 5.3. Resonators with diameters of 0.8, 1, 1.5 and 2 μm diameter are implemented, placed between 70 and 110 nm apart from 120 nm wide waveguides. The devices are not imaged in a SEM since exposure of the NV^- to electron irradiation may lead to a conversion of the NV^- charge state [20], [48].

6.2 Off-chip collection of the NV^- ZPL through a hybrid GaP\diamond optical network

The realization of GaP device structures coupled to NV^- centers in diamond provides an added challenge in that coupling of the NV^- ZPL emission to an optical cavity can only occur if:

- The NV^- is spatially located within the cavity electric field.
- The NV^- dipole is aligned at least partially with the cavity electric field vector.
- The cavity mode frequency overlaps with the NV^- spectral line.

Creation of the NV^- centers in diamond by ion implantation of the entire diamond substrate does not allow for control over the specific lateral location (only the depth) of a defect in the diamond lattice. While this approach is not expected to be effective for the realization of large-scale

entanglement networks, it provides an easy means for a proof-of-principle demonstration of NV^- coupling in single devices. A second element we cannot currently control is the NV^- dipole orientation. The NV^- symmetry axis will be one of 4 possible orientations in the diamond lattice, with two orthogonal dipole moments perpendicular to the symmetry axis. The use of blanket implantation, however, enhances the probability of locating an optimally aligned NV center: For an implantation dose of 10^{10} cm^{-2}, and an NV^- conversion rate of between 1 and 10%, we expect ~ 1 to 10 NV^- centers in a 1 μm^2 area.

In addition, control over the specific cavity resonance frequency of a single resonator is currently limited. The resonances can vary due to fabrication tolerances or material imperfections (see Appendix D). Hence, transmission measurements, as described in chapter 5, are employed to screen a large device array for resonators with suitable resonance wavelengths. Furthermore, the loaded quality factor Q_l is measured for each device to estimate its potential performance for a well-positioned NV^- center. Only devices with reasonably high Q_l are investigated further.

Off-chip coupling of the NV^- ZPL is demonstrated for a 1 μm disk with a designed waveguide-resonator spacing of 90 nm. Fig. 6.2.1(a) displays the room-temperature transmission spectrum showing resonance dips at ~ 634.5 nm and 639.9 nm. The cavity mode at the higher wavelength is the one relevant for collection of the NV^- emission as discussed below. The Q_l of the resonance at 639.9 nm is 1,600, with a contrast of ~ 85% (Fig. 6.2.1(b)). This indicates that the device operates close to critical coupling. The inset in Fig. 6.2.1(b) shows the temperature dependence of two resonance modes, as measured between 25 K (the temperature relevant for gas tuning of the cavity resonances) and 300 K. The change in resonance wavelength with temperature is mainly attributed to the temperature dependence of the GaP refractive index. The

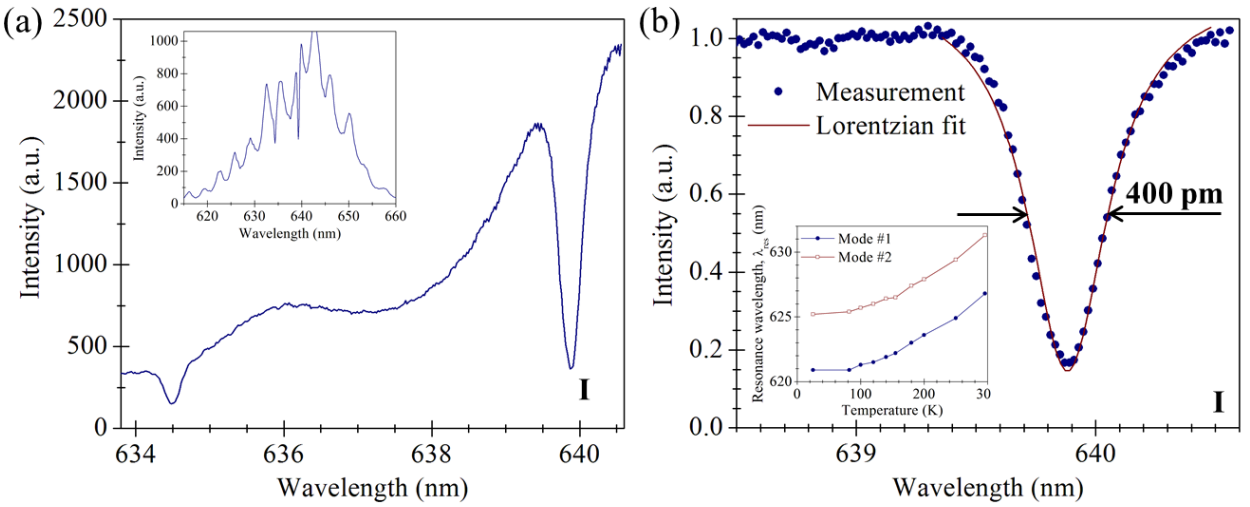

Fig. 6.2.1: Transmission measurement for 1 μm diameter GaP disk resonator to determine the loaded quality factor Q_l. (a) Transmission spectrum showing two cavity modes at 634.5 nm and 639.9 nm, respectively. The inset is a low-resolution spectrum (300 grooves/mm grating). (b) High-resolution spectrum of cavity mode at 639.9 nm. With a resonance wavelength of 639.9 nm and a fitted *FWHM* of ~ 400 pm, Q_l is ~ 1,600. The high-resolution spectra are collected at room temperature with an 1800 grooves/mm grating. The inset in (b) shows the temperature dependence of two cavity modes recorded between 25 K and room temperature.

temperature dependence of the refractive index shifts the resonance mode of this cavity from 639.9 nm at room temperature to ~ 635 nm at 25 K, 2 nm blue-detuned from the NV^- ZPL.

To demonstrate coupling of the NV^- ZPL emission from the diamond substrate into the

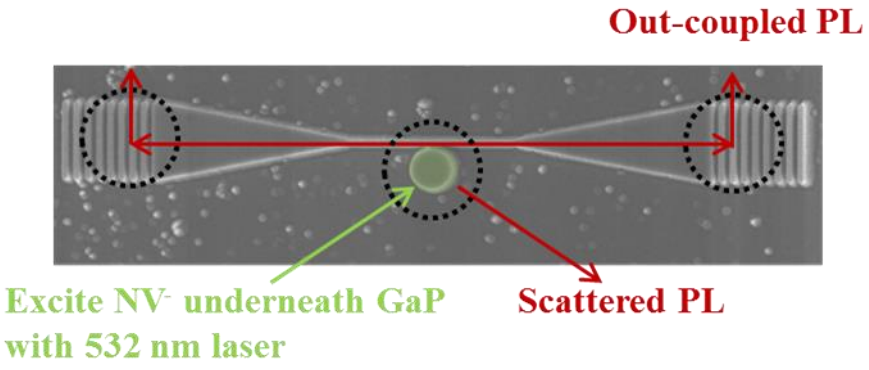

Fig. 6.2.2: Schematic of measurement setup for NV^- PL collection through grating couplers and on top of disk resonator. NV^- defect centers in the diamond substrate underneath the GaP disk are excited with 532 nm laser light. The NV^- emission coupled to the GaP resonator can either be collected as scattered PL on top of the disk or PL coupled to the waveguide and grating couplers. The SEM image is of a similar device on the mechanical-grade diamond substrate.

optical devices, the sample is mounted in a Janis ST-500 helium-flow cryostat which is cooled down to ~ 25 K. The PL of the NV^- centers is excited with green (532 nm) laser light as shown in Fig. 6.2.2. The diameter of the excitation spot size is $\lesssim 1$ μm. A PL spectrum of the cavity modes and NV^- can be collected as scattered light on top of the disk. Alternatively, the resonance modes can be coupled to the waveguide and coupled off-chip through the grating.

Fig. 6.2.3 displays the PL spectrum of the light scattered from the disk upon excitation of the device (blue line). The resonance mode is now visible at ~ 634.5 nm. Three distinct NV^- ZPLs at ~ 637.1 nm, 637.3 nm and 637.7 nm are visible. The inhomogeneous broadening of the ZPLs is

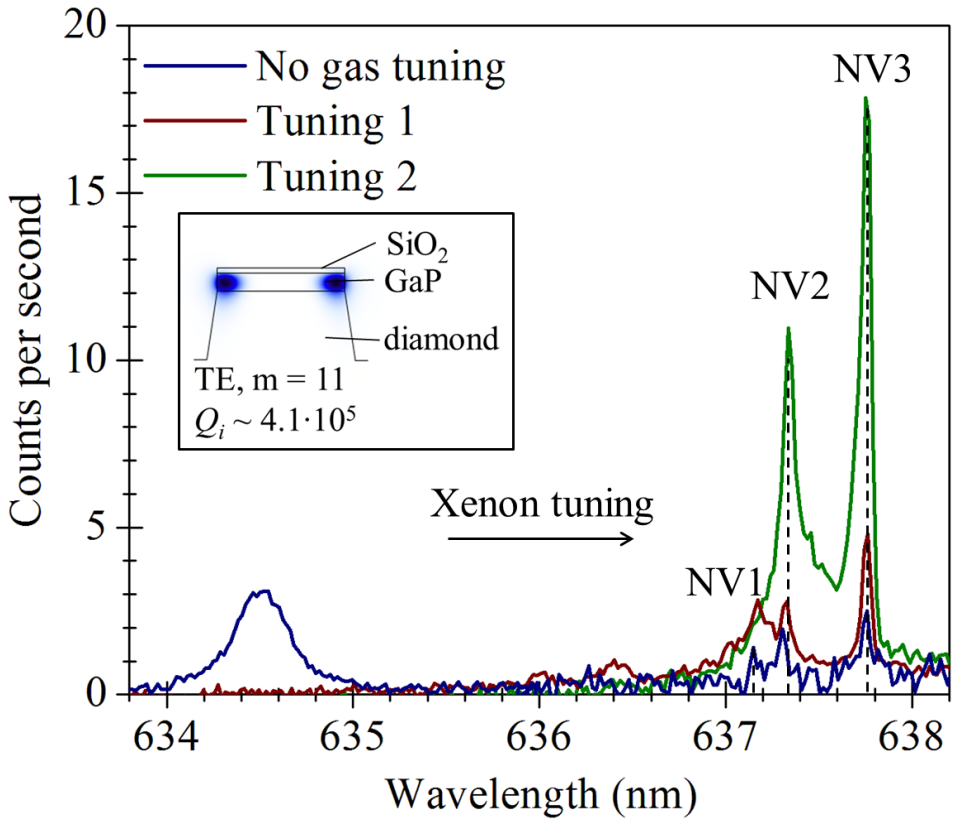

Fig. 6.2.3: PL spectra collected on top of the 1 μm diameter GaP disk resonator. The blue line shows the initial position of the cavity mode at ~ 634.5 nm, and three individual NV^- spectral lines at ~ 637.1 nm, 637.3 nm, and 637.7 nm. The red and blue lines show the PL signal collected after gas tuning the cavity resonance onto the NV^- ZPL, indicating a possible enhancement of the emission of NV2 and NV3. Measurements are taken at 25 K in a Janis ST-500 helium flow cryostat. The disk is excited with a 2.5 mW, 532 nm cw laser. The PL is collected using a 1800 grooves/mm grating. The inset shows the simulated TE mode for an uncoupled 1 μm diameter device on a 550 nm diamond pedestal.

typically caused by strain in the diamond substrate due to the implantation process. Each line is most likely due to a single NV center.

To enable the collection of the NV^- emission with resonators the cavity wavelength must be tuned to the NV^- ZPL. A gas tuning technique is employed to shift the cavity resonance [156], [157]. At low temperatures, xenon (Xe) gas injected into the cryostat condenses onto the resonators, lowers the index contrast between GaP and the surrounding environment, and thereby red-shifts the resonance wavelength. Quasi-2-D simulations of 1 μm devices in a Xe atmosphere (n_{xenon}=1.45 [158], [159]) indicate a maximum available tuning range of ~ 6 nm. A maximum tuning range of ~ 4.5 nm is observed experimentally for these devices.

If the NV^- PL is coupled to the resonator, a spectral line at the NV^- ZPL wavelength is expected in the PL spectra collected on the grating. Enhancement of the ZPL spontaneous emission rate will also result in an enhancement in the scattered PL collected directly from the disk. In the subsequent measurements, both of these indicators of Purcell enhancement are observed. However, we note that additional lifetime measurements are necessary to confirm and quantify the enhancement of the spontaneous emission into the ZPL.

Tuning of the resonator mode onto the NV^- ZPL is displayed in Fig. 6.2.3 for two different tuned resonator frequencies (red and green lines), as collected from the top of the disk. While there is no apparent enhancement of the NV^- emission at 637.1 nm, the ZPLs at 637.3 nm and 637.7 nm appear brighter if the cavity mode overlaps with these spectral lines. This indicates coupling of the NV^- to the cavity structure.

Fig. 6.2.4 displays the full tuning curve of the resonance mode coupled off-chip through the grating. The cavity mode red-shifts with the injection of Xe into the cryostat. Each tuning cycle corresponds to an arbitrary amount of Xe gas that is allowed to enter the cryostat. A second

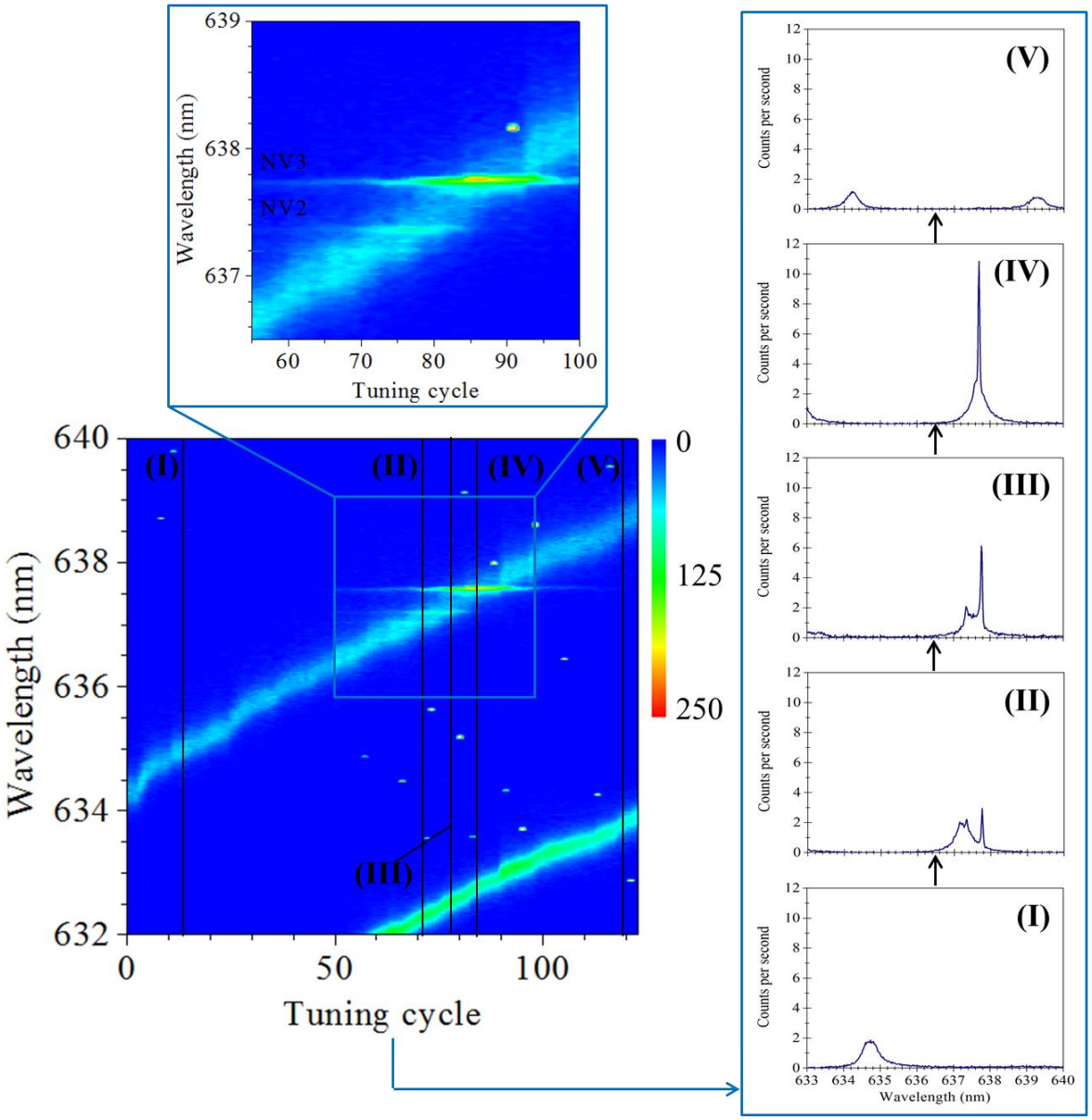

Fig. 6.2.4: Off-chip coupling of NV^- ZPL in a hybrid GaP\diamond optical network. The tuning curve shows the shift in the cavity mode resonance wavelength with increasing Xe condensation in the cryostat. A second cavity mode becomes visible at tuning cycle #60. When the resonance mode approaches the NV^- ZPL, the NV- emission coupled into the disk and routed toward the grating coupler can be collected through the grating. This emission is visible as horizontal lines in the tuning curve, which remain constant. PL spectra for selected tuning cycles (right panel) showing coupling of NV^- at ~ 637.3 nm and ~ 637.7 nm. Measurements are carried out at 25 K. The integration time for each point in the tuning curve is 25 s.

resonance mode becomes visible at tuning cycle #60.

When the cavity resonance approaches the spectral NV^- lines at ~ 637.3 nm and 637.7 nm, the respective ZPLs can be collected through the grating. These spectral lines become visible as horizontal strips in the tuning curve at the respective wavelengths, which do not change in wavelength with Xe injection. The ZPL at 637.7 nm appears to be coupled most efficiently, with a significantly higher intensity recorded. This again indicates that the ZPL emission of these NV^- centers is coupled to the cavity mode and further to the bus waveguide, where it is routed toward the grating coupler and scattered off-chip. To our knowledge, this is the first demonstration of NV^- ZPL routing in a hybrid GaP\diamond network.

6.3 Estimated coupling efficiencies for the NV^- ZPL photons in a hybrid GaP\diamond optical network

6.3.1 Estimation of theoretical possible NV^- ZPL count rates in GaP bus waveguide for current device performance and comparison to free-space coupling

For high-fidelity quantum operations, entanglement between distant NV^- centers should ideally be created within their electron spin coherence time. Hence, in a future integrated entanglement network ZPL photons have to be collected and routed toward an on-chip entanglement unit within that timeframe. Here, we estimate the rate of ZPL photons collected from a single NV^- center coupled to a GaP resonator with the coupled quality factor measured above.

The expected number of ZPL photons coupled off-chip through the gratings is calculated using Eq. 5.8. This calculation assumes that the NV^- center emits one photon every 12 ns, the NV^- radiative lifetime [160]. Q_i and Q_c are estimated from coupled mode theory using the measured Q_l and the contrast of the transmission curve in Fig. 6.2.1(b) [161]–[163]. Q_i is ~ 2,900 and Q_c is ~ 3,200, i.e. the resonator appears almost critically coupled. We next note that the thinner GaP layer leads to an increase in $(|\boldsymbol{E}_{NV}|/|\boldsymbol{E}_{max}|)^2$ (~0.21) when compared to the 200 nm

thick devices in chapter 5 ($(|\boldsymbol{E}_{NV}|/|\boldsymbol{E}_{max}|)^2$ ~ 0.16). Finally, the simulated mode volume V of a 1 μm diameter, 150 nm thick disk is ~ 0.022 μm^3. With Eq. 5.5, the expected theoretical enhancement of the spontaneous emission rate is then ~ 11. The total fraction of the NV^- emission coupled into the waveguide as ZPL photons is therefore ~ 12%. This again assumes the NV^- being located in an anti-node of the cavity mode and for ideal alignment of the NV^- dipole with the cavity field.

Assuming a total NV^- photon emission rate of $8.3 \cdot 10^4$ ms^{-1} (i.e. one NV^- photon emitted every 12 ns, the NV^- radiative lifetime) and 50% of the NV^- photon routed into each waveguide direction, ~ 4,900 ZPL photons should be coupled into each direction of the waveguide per ms, respectively. We can compare this rate to the expected number of ZPL photons that can be collected by a 0.9 (0.7) numerical aperture (NA) objective in free space. Assuming spatially uniform emission of the NV^- photons into the environment and a transmission efficiency of ~ 83% at the diamond-air interface, for an NV^- center located 15 nm below the diamond surface about 3% (1.8%) of the total photons can be coupled from the diamond substrate to air and collected by the objective lens. With 3% of the NV^- photons emitted in the ZPL, this corresponds to ~ 75 (45) ZPL photons collected per ms. Hence, under ideal conditions, we expect an increase > 60 in the ZPL collection efficiency compared to free-space collection.

Fig. 6.3.1 displays the expected photon counts per ms through a grating for various Purcell factors and grating coupler efficiencies, as calculated for a Q_i of 2,900 and Q_c of 3,200. The coupling efficiency of ZPL photons into the waveguide is strongly dependent on the Purcell enhancement provided by the resonator structures. The maximum enhancement of the spontaneous ZPL emission rate is expected to be lower than calculated above due to the

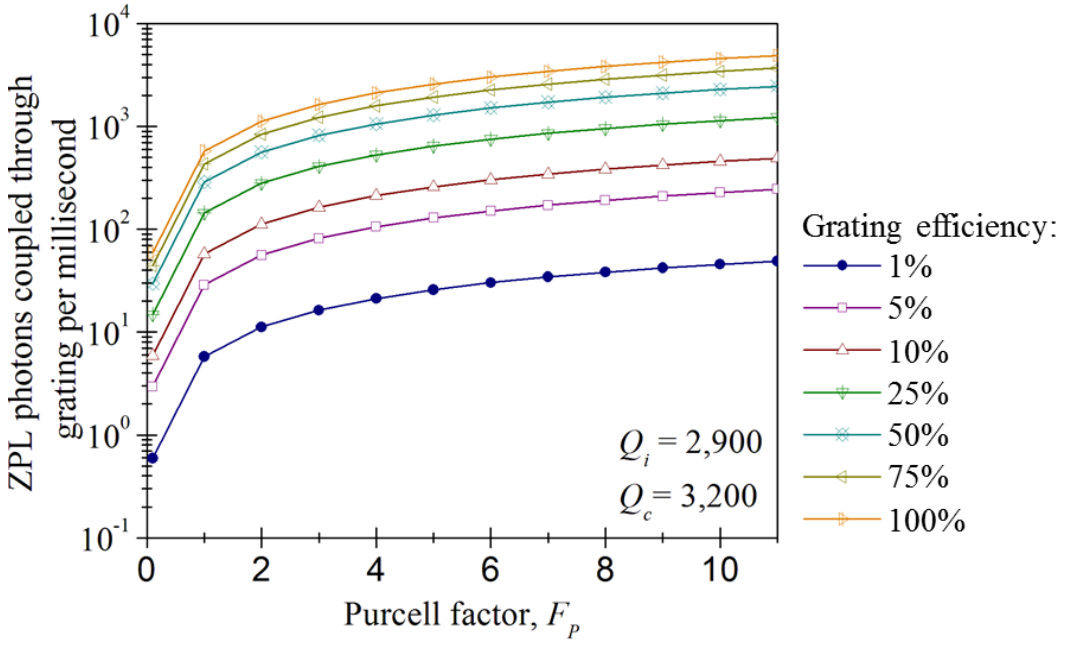

Fig. 6.3.1: Estimated rate of ZPL photons off-chip coupling for various grating coupling efficiencies and Purcell factors for 1 μm diameter disk adjacent to 120 nm waveguide with a 90 nm gap between waveguide and resonator.

orientation of the NV^- in the diamond lattice as well as non-ideal placement of the defect with regard to the cavity electric field maximum, as will be discussed in the following section.

6.3.2 Estimation of NV^- ZPL off-chip coupling efficiencies in a hybrid GaP\diamond network

Now, we attempt to estimate the actual coupling efficiencies of NV^- ZPL photons and the efficiency of the output grating coupler using the ZPL count rates obtained for maximum coupling of NV3 in Fig. 6.2.4. ~ 20 ZPL counts per second are recorded on the CCD for collection through the grating. This corresponds to ~ 830 NV^- ZPL photons collected off-chip through the grating each second, taking into account a grating efficiency of 40%, a detector efficiency of ~ 30% and a conversion factor (~ 5) utilized in the software for collection of the spectra.

In comparison, the spectrum in Fig. 6.2.3 for top collection of the device indicates ~ 5 CCD detector counts per second for each single NV^- ZPL (blue line for the case in which the NV^- are

not coupled to the cavity mode). The substrate is excited with 2.5 mW laser power, which should saturate the defects. 5 ZPL counts per second collected by the spectrometer CCD correspond to ~ 200 NV^- ZPL photons collected each second directly on top of the GaP layer from a single NV^- center. Typically, we can collect ~ 300 NV^- ZPL photons per second from single near-surface NV^- centers in diamond in our setup (0.7 NA objective lens), which corresponds to ~ 8 ZPL counts per second on the CCD detector for our 1800 grooves/mm grating. We expect the collection efficiencies of NV^- photons through the GaP layer to be ~ 25% lower compared to collection from a bare diamond substrate due to the enhanced reflection at the GaP\air interface in the diamond\GaP stack; this would correspond to ~ 230 ZPL photons s^{-1}. Hence, the lower number of total ZPL counts recorded for the uncoupled NV^- centers in the hybrid GaP\diamond platform compared to single NV^- centers in diamond can be explained by the reduced transmission through the additional GaP layer.

The collection of 300 ZPL photons per second for uncoupled NV^- in our measurement setup (0.7 NA) corresponds to a total NV^- photon emission rate of ~ $6 \cdot 10^5$ s^{-1} uniformly into space. This assumes 0.05% of the total NV^- emission collected as ZPL photons in free space as estimated above (3% of the NV^- photons are emitted into the ZPL, 1.8% of all NV^- photons can be detected with the 0.7 NA objective). The quantum efficiencies of single NV^- centers in bulk diamond are unknown. However, typical saturation count rates for the NV^- PSB found in literature are < $5 \cdot 10^4$ s^{-1} [65], [164]. In comparison, our ZPL count of 300 s^{-1} corresponds to a total count rate of ~ $1 \cdot 10^4$ s^{-1} for all emission frequencies.

830 ZPL photons per second are collected with the setup through the grating structures from NV3, when it is coupled to the GaP resonator. Hence, ~ 0.13% of the total number of emitted NV^- photons appear to be coupled off-chip as ZPL emission for this NV center. With Fig. 6.2.5,

this would correspond to a Purcell factor of ~ 1 and a grating efficiency of 5% or, alternatively, enhancement factors > 1 (≤ 1) and grating efficiencies < 5% (≥ 5%). In the next section, we will discuss parameters that currently limit the performance of these structures.

6.3.3 Loss mechanisms in the current hybrid GaP\diamond device structures

Several factors currently limit the NV^- ZPL photon collection efficiencies in these devices. These challenges include primarily the positioning and orientation of the single defect center with regard to the cavity mode volume and electric field vector as well as the output grating coupler efficiency. The efficiencies of GaP grating couplers are not an immediate concern since the better long-term solution should be on-chip photon detection. Optimal collection efficiencies are expected for on-chip detection schemes of single photons, e.g. with superconducting niobium nitride nanowires integrated on the GaP waveguides [86], [87].

Location and lattice orientation of the NV- defects, however, may provide a long-term challenge for high NV^- ZPL photon collection efficiencies. Here, the devices are fabricated on a (100) diamond substrate. NV^- centers created by ion implantation and annealing are oriented in one of four possible lattice directions ($[111]$, $[1\bar{1}\bar{1}]$, $[\bar{1}\bar{1}1]$, and $[\bar{1}1\bar{1}]$). Maximum coupling can only occur when the NV^- dipole moment (perpendicular to the NV^- axis) and the direction of the cavity electric field are aligned. Due to the inherent angle between the diamond surface and the respective NV^- orientation, the maximum fraction of the NV^- dipole field that can be coupled to the cavity is 0.5. Hence, the highest enhancement in spontaneous emission rate expected is ~ 5, if only the NV^- alignment is taken into account. This inherently limits the maximum coupling rate of ZPL photons into each waveguide direction to ~ 2,600 per ms on our diamond substrate.

A further reduction in the effective Purcell enhancement is expected due to the lateral placement of the NV^- centers. The inset in Fig. 6.2.3 displays the simulated electric field

distribution for quasi-TE excitation in the 1 μm diameter disk device. The electric field is confined toward the outer diameter of the disk. This may explain why the NV^- at 637.1 nm does not couple to the disk: the 1 μm^2 laser spot excites the majority of the disk, but only NV^- located underneath the outer areas of the device, in proximity to the maximum field of the cavity mode, couple most efficiently to the cavity mode.

While low grating coupler efficiencies can lead to reduced count rates, so does a reduced collection efficiency of NV^- ZPL photons due to fluctuations in the NV charge state. A comparison of NV^- to NV^0 ratio in the PL spectra taken on the fabricated device structures to the PL spectra recorded on diamond indicate that there may be a conversion of NV^- to NV^0 taking place, leading to reduced emission rates for NV^- photons. Fig. 6.3.2 displays low-resolution PL spectra of the NV^0 and NV^- ZPL, respectively, collected as scatter from the top of the disk. The NV^- to NV^0 ratio appears significantly decreased in this sample. Investigations of the GaP transfer or the electron beam lithography processes as cause for this conversion do not indicate them to induce a conversion of negatively charged defect centers to their neutral state (see

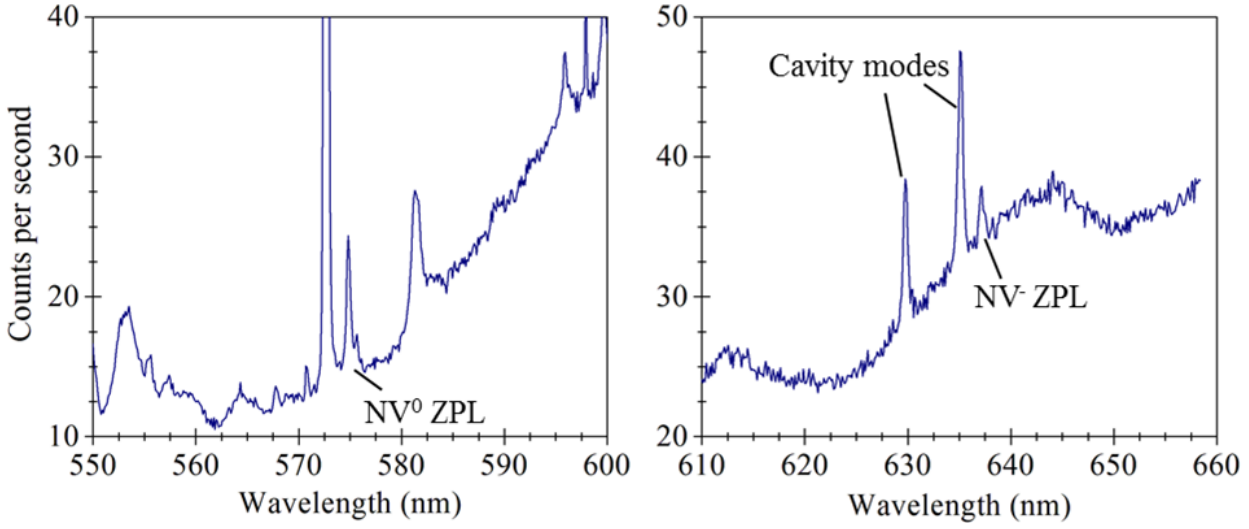

Fig. 6.3.2: PL spectra recorded on top of 1 μm diameter disk showing NV^0 (left) and NV^- (right) resonant spectral lines. Compared to Fig. 2.2.1(d), the NV^- ZPL line appears significantly weaker with respect to the NV^0 line. Data is taken at 82 K with a 300 grooves/mm grating. Excitation power is 2.5 mW.

Appendix D). Further investigations will be necessary into the cause of this apparent conversion but are outside the scope of this thesis.

6.4 Outlook for the hybrid GaP\diamond platform for large-scale optical networks

Collection of NV^- ZPL photons and routing to a bus waveguide in a hybrid optical network realized from single-crystalline GaP sheets on diamond is demonstrated for the first time. A gas tuning technique is utilized to align the cavity mode with the NV^- ZPL to allow coupling of the optical emission to the resonator structures. While this is a first critical step toward large-scale optical networks for entanglement generation between numerous, distant NV^- centers in bulk, an improvement in the device characteristics and NV^- properties will be necessary for multi-qubit QIP platforms.

As discussed in chapter 5, an increase in the intrinsic quality factor of the devices is expected to yield in higher Purcell factors and coupling rates. However, placement and orientation of the NV^- defects in the diamond lattice currently appear as the major limiting factors for strong enhancement of the spontaneous emission into the ZPL. The ion implantation process utilized for the preparation of the NV^- centers in our substrates does not provide the possibility to deterministically integrate the defects with a preferred orientation and location for optimal coupling to the cavity mode; significant research efforts in the community are currently focused on the preparation of NV^- defects with the desired properties. Optimal alignment of the NV^- dipole with the cavity field and placement of the defect close to the cavity field maximum in the diamond are critical to obtain the significant coupling rates discussed above. Furthermore, to establish the hybrid GaP\diamond platform as a viable, more functional alternative to all-diamond photonics, it will be necessary to demonstrate a linear EO device in GaP for the

integration of active device capabilities. To enable the implementation of entanglement networks, large device arrays with high quality factors and identical resonance characteristics will be essential. These cannot currently be realized due to fabrication tolerances and material imperfections. An overview over the current resonance characteristics in our device array is provided in Appendix D.

The successful demonstration of routing of NV^- ZPL photons in a hybrid optical network comprised of GaP as linear EO material and diamond as host for the defect centers, however, is considered a critical step and strong motivation for the exploration of this material platform for the realization of future large-scale entanglement networks.

Chapter 7:
Conclusion & outlook

High-fidelity entanglement generation between distant NV^- centers in large-scale integrated optical networks will likely require active optical device capabilities to select the desired physical qubits. Due to the material properties of diamond, optical switches can currently not be realized in an all-diamond platform. Hence, a hybrid material platform, which integrates NV^- centers in diamond with a linear EO waveguiding material, appears promising to provide these active optical device functionalities for diamond photonics. GaP is a linear EO material with a high refractive index, which allows for waveguiding of light in the visible range and may, in the future, enable the integration of optical switching capabilities in the diamond platform. A lack of large-area, high-quality GaP layers on diamond has, however, limited the implementation of coupled optical devices.

This work explores different approaches toward the integration of high-quality GaP device layers on diamond. Waveguide-integrated GaP resonators on diamond are demonstrated using an epitaxial lift-off process for the transfer of high-quality, single-crystalline GaP layers onto diamond substrates. Finally, collection of NV^- ZPL photons in a GaP cavity and subsequent on-chip routing of the ZPL emission in a coupled GaP bus waveguide is demonstrated.

In detail, this dissertation discusses:

- GaP layers directly deposited on diamond are explored as a straight-forward approach toward the integration of the linear EO material with the diamond platform. The high optical losses measured for this material (> -0.4 $dB\mu m^{-1}$), however, do currently not

allow for the realization of GaP cavity structures on diamond with high optical quality factors.

- An epitaxial lift-off process for the transfer of high-quality, single-crystalline GaP device layers onto diamond is developed. Coupling of the NV^- PSB emission to a GaP array fabricated in a deterministic fashion on the diamond substrate is demonstrated, indicating the suitability of the fabrication approach for integration with near-surface NV^- centers.
- The first hybrid GaP waveguide-coupled resonator structures on diamond are demonstrated. The devices are fabricated from single-crystalline GaP sheets transferred onto a mechanical-grade diamond substrate using the epitaxial lift-off approach. The measured device characteristics for 1 μm diameter disk resonators promise high collection and coupling efficiencies for NV^- ZPL photons if integrated with near-surface NV^- centers. 22% of the NV^- emission is theoretically expected to be coupled from the diamond substrate into a bus waveguide as ZPL photons.
- Finally, near-surface NV^- centers prepared in a diamond substrate are coupled to a hybrid GaP\diamond network. Collection and on-chip routing of the NV^- ZPL in waveguide-integrated GaP resonators on diamond is demonstrated. The cavity resonances are tuned into the NV^- ZPL using a gas condensation technique. This enables collection of NV^- photons in the GaP resonators and further coupling to adjacent GaP waveguides.

The successful collection and routing of NV^- photons in a hybrid GaP\diamond material platform now motivates the demonstration of an EO device in GaP to establish the hybrid approach as a more functional alternative to all-diamond networks.

The integration of distant NV^- as physical qubits in integrated optical entanglement networks will require other long-term technological issues to be resolved before such large-scale networks can be realized. However; these issues are not limited to the hybrid GaP\diamond platform. These challenges include: (i) the deterministic placement and orientation of the NV^- defects in the diamond lattice for efficient coupling to cavities, (ii) variations in the resonance wavelengths typically observed in large device arrays, (iii) the currently limited quality factors of the devices, as well as (iv) digital tuning of the cavity resonances to overlap with the NV^- spectral lines and (v) dynamic stabilization of the emission frequency of individual NV^- centers coupled to cavities, and Stark tuning of ZPL center wavelength of numerous defects to a single system frequency.

Finally, the transfer technique developed in this thesis for single-crystalline GaP and applied toward the realization of coupled hybrid photonic device structures on diamond may also find applications, either classical or quantum, on other substrates where efficient waveguiding of light within the visible wavelength range in a high-index waveguiding layer is desired.

References

[1] R. P. Feynman, “Simulating Physics with Computers,” *Int. J. Theor. Phys.*, vol. 21, no. 6–7, pp. 467–488, 1982.

[2] I. M. Georgescu, S. Ashhab, and F. Nori, “Quantum simulation,” *Rev. Mod. Phys.*, vol. 86, no. 1, pp. 153–185, Mar. 2014.

[3] P. W. Shor, “Polynomial-Time Algorithms for Prime Factorization and Discrete Logarithms on a Quantum Computer,” *SIAM J. Comput.*, vol. 26, no. 5, pp. 1484–1509, Oct. 1997.

[4] N. Gisin, G. Ribordy, W. Tittel, and H. Zbinden, “Quantum cryptography,” *Rev. Mod. Phys.*, vol. 74, no. 1, pp. 145–195, Mar. 2002.

[5] H.-K. Lo, M. Curty, and K. Tamaki, “Secure quantum key distribution,” *Nat. Photonics*, vol. 8, no. 8, pp. 595–604, Jul. 2014.

[6] L. K. Grover, “A fast quantum mechanical algorithm for database search,” in *Proceedings of the twenty-eighth annual ACM symposium on Theory of computing - STOC ’96*, 1996, pp. 212–219.

[7] R. Raussendorf and H. J. Briegel, “A One-Way Quantum Computer,” *Phys. Rev. Lett.*, vol. 86, no. 22, pp. 5188–5191, May 2001.

[8] H. J. Briegel, D. E. Browne, W. Dür, R. Raussendorf, and M. Van den Nest, “Measurement-based quantum computation,” *Nat. Phys.*, vol. 5, no. 1, pp. 19–26, Jan. 2009.

[9] S. C. Benjamin, B. W. Lovett, and J. M. Smith, “Prospects for measurement-based quantum computing with solid state spins,” *Laser Photonics Rev.*, vol. 3, no. 6, pp. 556–574, Nov. 2009.

[10] R. Blatt and D. Wineland, “Entangled states of trapped atomic ions.,” *Nature*, vol. 453, no. 7198, pp. 1008–15, Jun. 2008.

[11] L. Dicarlo, M. D. Reed, L. Sun, B. R. Johnson, J. M. Chow, J. M. Gambetta, L. Frunzio, S. M. Girvin, M. H. Devoret, and R. J. Schoelkopf, “Preparation and measurement of three-qubit entanglement in a superconducting circuit.,” *Nature*, vol. 467, no. 7315, pp. 574–8, Sep. 2010.

[12] M. Neeley, R. C. Bialczak, M. Lenander, E. Lucero, M. Mariantoni, A. D. O’Connell, D. Sank, H. Wang, M. Weides, J. Wenner, Y. Yin, T. Yamamoto, A. N. Cleland, and J. M.

Martinis, “Generation of three-qubit entangled states using superconducting phase qubits,” *Nature*, vol. 467, no. 7315, pp. 570–3, Sep. 2010.

[13] S. Ritter, C. Nölleke, C. Hahn, A. Reiserer, A. Neuzner, M. Uphoff, M. Mücke, E. Figueroa, J. Bochmann, and G. Rempe, “An elementary quantum network of single atoms in optical cavities.,” *Nature*, vol. 484, no. 7393, pp. 195–200, Apr. 2012.

[14] M. D. Shulman, O. E. Dial, S. P. Harvey, H. Bluhm, V. Umansky, and A. Yacoby, “Demonstration of entanglement of electrostatically coupled singlet-triplet qubits,” *Science*, vol. 336, no. 6078, pp. 202–5, Apr. 2012.

[15] A. Gruber, A. Dräbenstedt, C. Tietz, L. Fleury, J. Wrachtrup, and C. von Borczyskowski, “Scanning Confocal Optical Microscopy and Magnetic Resonance on Single Defect Centers,” *Science*, vol. 276, no. 5321, pp. 2012–2014, Jun. 1997.

[16] M. W. Doherty, N. B. Manson, P. Delaney, F. Jelezko, J. Wrachtrup, and L. C. L. Hollenberg, “The nitrogen-vacancy colour centre in diamond,” *Phys. Rep.*, vol. 528, no. 1, pp. 1–45, Jul. 2013.

[17] V. Acosta and P. Hemmer, “Nitrogen-vacancy centers: Physics and applications,” *MRS Bull.*, vol. 38, no. 02, pp. 127–130, Feb. 2013.

[18] H. Bernien, B. Hensen, W. Pfaff, G. Koolstra, M. S. Blok, L. Robledo, T. H. Taminiau, M. Markham, D. J. Twitchen, L. Childress, and R. Hanson, “Heralded entanglement between solid-state qubits separated by three metres.,” *Nature*, vol. 497, no. 7447, pp. 86–90, May 2013.

[19] E. M. Purcell, “Spontaneous Emission Probabilities at Radio Frequencies,” *Phys. Rev.*, vol. 69, p. 839, 1946.

[20] A. Faraon, P. E. Barclay, C. Santori, K. C. Fu, and R. G. Beausoleil, “Resonant enhancement of the zero-phonon emission from a colour centre in a diamond cavity,” *Nat. Photonics*, vol. 5, no. 5, pp. 301–305, Apr. 2011.

[21] B. J. M. Hausmann, B. Shields, Q. Quan, P. Maletinsky, M. McCutcheon, J. T. Choy, T. M. Babinec, A. Kubanek, A. Yacoby, M. D. Lukin, and M. Loncar, “Integrated diamond networks for quantum nanophotonics.,” *Nano Lett.*, vol. 12, no. 3, pp. 1578–82, Mar. 2012.

[22] A. Faraon, C. Santori, Z. Huang, K.-M. C. Fu, V. M. Acosta, D. Fattal, and R. G. Beausoleil, “Quantum photonic devices in single-crystal diamond,” *New J. Phys.*, vol. 15, no. 2, p. 025010, Feb. 2013.

[23] M. Lončar and A. Faraon, “Quantum photonic networks in diamond,” *MRS Bull.*, vol. 38, no. 02, pp. 144–148, Feb. 2013.

[24] Z. Huang, A. Faraon, C. Santori, V. Acosta, and R. G. Beausoleil, “Microring resonator-based diamond optothermal switch: a building block for a quantum computing network,” *Proc. SPIE, Advances in Photonics of Quantum Computing, Memory, and Communication IV*, 2013, vol. 8635, p. 86350E.

[25] B. J. M. Hausmann, I. Bulu, V. Venkataraman, P. Deotare, and M. Lončar, “Diamond nonlinear photonics,” *Nat. Photonics*, vol. 8, no. 5, pp. 369–374, Apr. 2014.

[26] D. F. Nelson, “Electro-optic and Piezoelectric Coefficients and Refractive Index of Gallium Phosphide,” *J. Appl. Phys.*, vol. 39, no. 7, p. 3337, 1968.

[27] D. Aspnes and A. Studna, “Dielectric functions and optical parameters of Si, Ge, GaP, GaAs, GaSb, InP, InAs, and InSb from 1.5 to 6.0 eV,” *Phys. Rev. B*, vol. 27, no. 2, pp. 985–1009, Jan. 1983.

[28] C. Xiong, W. H. P. Pernice, and H. X. Tang, “Low-loss, silicon integrated, aluminum nitride photonic circuits and their use for electro-optic signal processing.,” *Nano Lett.*, vol. 12, no. 7, pp. 3562–8, Jul. 2012.

[29] P. E. Barclay, K.-M. C. Fu, C. Santori, and R. G. Beausoleil, “Chip-based microcavities coupled to nitrogen-vacancy centers in single crystal diamond,” *Appl. Phys. Lett.*, vol. 95, no. 19, p. 191115, 2009.

[30] P. E. Barclay, K.-M. C. Fu, C. Santori, A. Faraon, and R. G. Beausoleil, “Hybrid Nanocavity Resonant Enhancement of Color Center Emission in Diamond,” *Phys. Rev. X*, vol. 1, no. 1, p. 011007, Sep. 2011.

[31] A. K. Ekert, “Quantum cryptography based on Bell’s theorem,” *Phys. Rev. Lett.*, vol. 67, no. 6, pp. 661–663, Aug. 1991.

[32] S. Garnerone, P. Zanardi, and D. a. Lidar, “Adiabatic Quantum Algorithm for Search Engine Ranking,” *Phys. Rev. Lett.*, vol. 108, no. 23, p. 230506, Jun. 2012.

[33] D. Bouwmeester, J. Pan, K. Mattle, M. Eibl, H. Weinfurter, and A. Zeilinger, “Experimental quantum teleportation,” *Nature*, vol. 390, pp. 575–579, 1997.

[34] W. Pfaff, B. Hensen, H. Bernien, S. B. van Dam, M. S. Blok, T. H. Taminiau, M. J. Tiggelman, R. N. Schouten, M. Markham, D. J. Twitchen, and R. Hanson, “Unconditional quantum teleportation between distant solid-state quantum bits,” *Science*, vol. 1253512, no. May, pp. 1–8, May 2014.

[35] T. D. Ladd, F. Jelezko, R. Laflamme, Y. Nakamura, C. Monroe, and J. L. O’Brien, “Quantum computers.,” *Nature*, vol. 464, no. 7285, pp. 45–53, Mar. 2010.

[36] L. M. Duan, M. D. Lukin, J. I. Cirac, and P. Zoller, “Long-distance quantum communication with atomic ensembles and linear optics.,” *Nature*, vol. 414, no. 6862, pp. 413–8, Nov. 2001.

[37] L. Childress and R. Hanson, “Diamond NV centers for quantum computing and quantum networks,” *MRS Bull.*, vol. 38, no. 02, pp. 134–138, Feb. 2013.

[38] T. Ishikawa, K.-M. C. Fu, C. Santori, V. M. Acosta, R. G. Beausoleil, H. Watanabe, S. Shikata, and K. M. Itoh, “Optical and spin coherence properties of nitrogen-vacancy centers placed in a 100 nm thick isotopically purified diamond layer.,” *Nano Lett.*, vol. 12, no. 4, pp. 2083–7, Apr. 2012.

[39] T. Yamamoto, T. Umeda, K. Watanabe, S. Onoda, M. L. Markham, D. J. Twitchen, B. Naydenov, L. P. McGuinness, T. Teraji, S. Koizumi, F. Dolde, H. Fedder, J. Honert, J. Wrachtrup, T. Ohshima, F. Jelezko, and J. Isoya, “Extending spin coherence times of diamond qubits by high-temperature annealing,” *Phys. Rev. B*, vol. 88, no. 7, p. 075206, Aug. 2013.

[40] J. Wrachtrup, F. Jelezko, B. Grotz, and L. McGuinness, “Nitrogen-vacancy centers close to surfaces,” *MRS Bull.*, vol. 38, no. 02, pp. 149–154, Feb. 2013.

[41] G. Balasubramanian, P. Neumann, D. Twitchen, M. Markham, R. Kolesov, N. Mizuochi, J. Isoya, J. Achard, J. Beck, J. Tissler, V. Jacques, P. R. Hemmer, F. Jelezko, and J. Wrachtrup, “Ultralong spin coherence time in isotopically engineered diamond.,” *Nat. Mater.*, vol. 8, no. 5, pp. 383–7, May 2009.

[42] I. Aharonovich, A. D. Greentree, and S. Prawer, “Diamond photonics,” *Nat. Photonics*, vol. 5, no. 7, pp. 397–405, Jun. 2011.

[43] G. Davies, “Vibronic spectra in diamond,” *J. Phys. C Solid State Phys.*, vol. 7, no. 20, pp. 3797–3809, Oct. 1974.

[44] C. Santori, P. E. Barclay, K.-M. C. Fu, R. G. Beausoleil, S. Spillane, and M. Fisch, “Nanophotonics for quantum optics using nitrogen-vacancy centers in diamond.,” *Nanotechnology*, vol. 21, no. 27, p. 274008, Jul. 2010.

[45] T. van der Sar, Z. H. Wang, M. S. Blok, H. Bernien, T. H. Taminiau, D. M. Toyli, D. a Lidar, D. D. Awschalom, R. Hanson, and V. V Dobrovitski, “Decoherence-protected quantum gates for a hybrid solid-state spin register.,” *Nature*, vol. 484, no. 7392, pp. 82–6, May 2012.

[46] N. Bar-Gill, L. M. Pham, A. Jarmola, D. Budker, and R. L. Walsworth, “Solid-state electronic spin coherence time approaching one second.,” *Nat. Commun.*, vol. 4, p. 1743, Jan. 2013.

[47] P. C. Maurer, G. Kucsko, C. Latta, L. Jiang, N. Y. Yao, S. D. Bennett, F. Pastawski, D. Hunger, N. Chisholm, M. Markham, D. J. Twitchen, J. I. Cirac, and M. D. Lukin, "Room-temperature quantum bit memory exceeding one second.," *Science*, vol. 336, no. 6086, pp. 1283–6, Jun. 2012.

[48] J. Schwartz, S. Aloni, D. F. Ogletree, and T. Schenkel, "Effects of low-energy electron irradiation on formation of nitrogen–vacancy centers in single-crystal diamond," *New J. Phys.*, vol. 14, no. 4, p. 043024, Apr. 2012.

[49] V. Acosta, E. Bauch, M. Ledbetter, C. Santori, K.-M. Fu, P. Barclay, R. Beausoleil, H. Linget, J. Roch, F. Treussart, S. Chemerisov, W. Gawlik, and D. Budker, "Diamonds with a high density of nitrogen-vacancy centers for magnetometry applications," *Phys. Rev. B*, vol. 80, no. 11, p. 115202, Sep. 2009.

[50] D. M. Toyli, C. D. Weis, G. D. Fuchs, T. Schenkel, and D. D. Awschalom, "Chip-scale nanofabrication of single spins and spin arrays in diamond.," *Nano Lett.*, vol. 10, no. 8, pp. 3168–72, Aug. 2010.

[51] B. J. M. Hausmann, T. M. Babinec, J. T. Choy, J. S. Hodges, S. Hong, I. Bulu, A. Yacoby, M. D. Lukin, and M. Lončar, "Single-color centers implanted in diamond nanostructures," *New J. Phys.*, vol. 13, no. 4, p. 045004, Apr. 2011.

[52] C. Santori, P. Barclay, K.-M. Fu, and R. Beausoleil, "Vertical distribution of nitrogen-vacancy centers in diamond formed by ion implantation and annealing," *Phys. Rev. B*, vol. 79, no. 12, p. 125313, Mar. 2009.

[53] B. Naydenov, V. Richter, J. Beck, M. Steiner, P. Neumann, G. Balasubramanian, J. Achard, F. Jelezko, J. Wrachtrup, and R. Kalish, "Enhanced generation of single optically active spins in diamond by ion implantation," *Appl. Phys. Lett.*, vol. 96, no. 16, p. 163108, 2010.

[54] Y. Chu, N. P. de Leon, B. J. Shields, B. Hausmann, R. Evans, E. Togan, M. J. Burek, M. Markham, A. Stacey, A. S. Zibrov, A. Yacoby, D. J. Twitchen, M. Loncar, H. Park, P. Maletinsky, and M. D. Lukin, "Coherent optical transitions in implanted nitrogen vacancy centers.," *Nano Lett.*, vol. 14, no. 4, pp. 1982–6, Apr. 2014.

[55] K. Ohno, F. Joseph Heremans, L. C. Bassett, B. A. Myers, D. M. Toyli, A. C. Bleszynski Jayich, C. J. Palmstrøm, and D. D. Awschalom, "Engineering shallow spins in diamond with nitrogen delta-doping," *Appl. Phys. Lett.*, vol. 101, no. 8, p. 082413, 2012.

[56] K. Ohno, F. J. Heremans, C. F. de las Casas, B. A. Myers, B. J. Alemán, A. C. Bleszynski Jayich, and D. D. Awschalom, "Three-dimensional localization of spins in diamond using 12C implantation," *Appl. Phys. Lett.*, vol. 105, no. 5, p. 052406, Aug. 2014.

[57] J. Michl, T. Teraji, S. Zaiser, I. Jakobi, G. Waldherr, F. Dolde, P. Neumann, M. W. Doherty, N. B. Manson, J. Isoya, and J. Wrachtrup, "Perfect alignment and preferential

orientation of nitrogen-vacancy centers during chemical vapor deposition diamond growth on (111) surfaces," *Appl. Phys. Lett.*, vol. 104, no. 10, p. 102407, Mar. 2014.

[58] W. Pfaff, T. H. Taminiau, L. Robledo, H. Bernien, M. Markham, D. J. Twitchen, and R. Hanson, "Demonstration of entanglement-by-measurement of solid-state qubits," *Nat. Phys.*, vol. 9, no. 1, pp. 29–33, Oct. 2012.

[59] H. Bernien, L. Childress, L. Robledo, M. Markham, D. Twitchen, and R. Hanson, "Two-Photon Quantum Interference from Separate Nitrogen Vacancy Centers in Diamond," *Phys. Rev. Lett.*, vol. 108, no. 4, p. 043604, Jan. 2012.

[60] F. Dolde, I. Jakobi, B. Naydenov, N. Zhao, S. Pezzagna, C. Trautmann, J. Meijer, P. Neumann, F. Jelezko, and J. Wrachtrup, "Room-temperature entanglement between single defect spins in diamond," *Nat. Phys.*, vol. 9, no. 3, pp. 139–143, Feb. 2013.

[61] F. Dolde, V. Bergholm, Y. Wang, I. Jakobi, B. Naydenov, S. Pezzagna, J. Meijer, F. Jelezko, P. Neumann, T. Schulte-Herbrüggen, J. Biamonte, and J. Wrachtrup, "High-fidelity spin entanglement using optimal control.," *Nat. Commun.*, vol. 5, p. 3371, Jan. 2014.

[62] J. P. Hadden, J. P. Harrison, A. C. Stanley-Clarke, L. Marseglia, Y.-L. D. Ho, B. R. Patton, J. L. O'Brien, and J. G. Rarity, "Strongly enhanced photon collection from diamond defect centers under microfabricated integrated solid immersion lenses," *Appl. Phys. Lett.*, vol. 97, no. 24, p. 241901, 2010.

[63] L. Marseglia, J. P. Hadden, A. C. Stanley-Clarke, J. P. Harrison, B. Patton, Y.-L. D. Ho, B. Naydenov, F. Jelezko, J. Meijer, P. R. Dolan, J. M. Smith, J. G. Rarity, and J. L. O'Brien, "Nanofabricated solid immersion lenses registered to single emitters in diamond," *Appl. Phys. Lett.*, vol. 98, no. 13, p. 133107, 2011.

[64] L. Robledo, L. Childress, H. Bernien, B. Hensen, P. F. a Alkemade, and R. Hanson, "High-fidelity projective read-out of a solid-state spin quantum register.," *Nature*, vol. 477, no. 7366, pp. 574–8, Sep. 2011.

[65] T. M. Babinec, B. J. M. Hausmann, M. Khan, Y. Zhang, J. R. Maze, P. R. Hemmer, and M. Lončar, "A diamond nanowire single-photon source.," *Nat. Nanotechnol.*, vol. 5, no. 3, pp. 195–9, Mar. 2010.

[66] A. Faraon, C. Santori, Z. Huang, V. M. Acosta, and R. G. Beausoleil, "Coupling of Nitrogen-Vacancy Centers to Photonic Crystal Cavities in Monocrystalline Diamond," *Phys. Rev. Lett.*, vol. 109, no. 3, p. 033604, Jul. 2012.

[67] J. D. Joannopoulos, P. R. Villeneuve, and S. Fan, "Photonic crystals: putting a new twist on light," *Nature*, vol. 386, no. 6621, pp. 143–149, Mar. 1997.

[68] K. J. Vahala, "Optical microcavities.," *Nature*, vol. 424, no. 6950, pp. 839–46, Aug. 2003.

[69] T. M. Benson, S. V. Boriskina, P. Sewell, A. Vukovic, S. C. Greedy, and A. I. Nosich, "MICRO-OPTICAL RESONATORS FOR MICROLASERS AND INTEGRATED OPTOELECTRONICS Recent advances and future challenges," in *Frontiers in planar lightwave circuit technology*, Springer Netherlands, 2006, pp. 39–70.

[70] T. Yoshie, L. Tang, and S.-Y. Su, "Optical microcavity: sensing down to single molecules and atoms.," *Sensors (Basel).*, vol. 11, no. 2, pp. 1972–91, Jan. 2011.

[71] M. Borselli, T. Johnson, and O. Painter, "Beyond the Rayleigh scattering limit in high-Q silicon microdisks: theory and experiment.," *Opt. Express*, vol. 13, no. 5, pp. 1515–30, Mar. 2005.

[72] L. Andreani, G. Panzarini, and J.-M. Gérard, "Strong-coupling regime for quantum boxes in pillar microcavities: Theory," *Phys. Rev. B*, vol. 60, no. 19, pp. 13276–13279, Nov. 1999.

[73] D. Kleppner, "Inhibited Spontaneous Emission," *Phys. Rev. Lett.*, vol. 47, no. 4, pp. 233–236, Jul. 1981.

[74] J. Riedrich-Möller, L. Kipfstuhl, C. Hepp, E. Neu, C. Pauly, F. Mücklich, A. Baur, M. Wandt, S. Wolff, M. Fischer, S. Gsell, M. Schreck, and C. Becher, "One- and two-dimensional photonic crystal microcavities in single crystal diamond.," *Nat. Nanotechnol.*, vol. 7, no. 1, pp. 69–74, Jan. 2012.

[75] B. J. M. Hausmann, B. J. Shields, Q. Quan, Y. Chu, N. P. de Leon, R. Evans, M. J. Burek, A. S. Zibrov, M. Markham, D. J. Twitchen, H. Park, M. D. Lukin, and M. Lončar, "Coupling of NV Centers to Photonic Crystal Nanobeams in Diamond.," *Nano Lett.*, Nov. 2013.

[76] B. J. M. Hausmann, I. B. Bulu, P. B. Deotare, M. McCutcheon, V. Venkataraman, M. L. Markham, D. J. Twitchen, and M. Lončar, "Integrated high-quality factor optical resonators in diamond.," *Nano Lett.*, vol. 13, no. 5, pp. 1898–902, May 2013.

[77] C. Xiong, W. H. P. Pernice, X. Sun, C. Schuck, K. Y. Fong, and H. X. Tang, "Aluminum nitride as a new material for chip-scale optomechanics and nonlinear optics," *New J. Phys.*, vol. 14, no. 9, p. 095014, Sep. 2012.

[78] W. H. P. Pernice, C. Xiong, and H. X. Tang, "High Q micro-ring resonators fabricated from polycrystalline aluminum nitride films for near infrared and visible photonics.," *Opt. Express*, vol. 20, no. 11, pp. 12261–9, May 2012.

[79] S. Adachi, "Optical dispersion relations for GaP, GaAs, GaSb, InP, InAs, InSb, $Al_xGa_{1-x}As$, and $In_{1-x}GaxAs_yP_{1-y}$," *J. Appl. Phys.*, vol. 66, no. 12, p. 6030, 1989.

[80] Ioffe. Web. Accessed Aug. 22, 2014. http://www.ioffe.ru/SVA/NSM/Semicond/GaP/.

[81] WebElements. Web. Accessed Aug. 22,2014. http://www.webelements.com/compounds/gallium/gallium_phosphide.html.

[82] K.-M. C. Fu, C. Santori, P. E. Barclay, I. Aharonovich, S. Prawer, N. Meyer, a. M. Holm, and R. G. Beausoleil, "Coupling of nitrogen-vacancy centers in diamond to a GaP waveguide," *Appl. Phys. Lett.*, vol. 93, no. 23, p. 234107, 2008.

[83] J. Wolters, A. W. Schell, G. Kewes, N. Nüsse, M. Schoengen, H. Döscher, T. Hannappel, B. Löchel, M. Barth, and O. Benson, "Enhancement of the zero phonon line emission from a single nitrogen vacancy center in a nanodiamond via coupling to a photonic crystal cavity," *Appl. Phys. Lett.*, vol. 97, no. 14, p. 141108, 2010.

[84] D. Englund, B. Shields, K. Rivoire, F. Hatami, J. Vučković, H. Park, and M. D. Lukin, "Deterministic coupling of a single nitrogen vacancy center to a photonic crystal cavity.," *Nano Lett.*, vol. 10, no. 10, pp. 3922–6, Oct. 2010.

[85] K.-M. C. Fu, P. E. Barclay, C. Santori, a Faraon, and R. G. Beausoleil, "Low-temperature tapered-fiber probing of diamond nitrogen-vacancy ensembles coupled to GaP microcavities," *New J. Phys.*, vol. 13, no. 5, p. 055023, May 2011.

[86] A. Gaggero, S. J. Nejad, F. Marsili, F. Mattioli, R. Leoni, D. Bitauld, D. Sahin, G. J. Hamhuis, R. Nötzel, R. Sanjines, and A. Fiore, "Nanowire superconducting single-photon detectors on GaAs for integrated quantum photonic applications," *Appl. Phys. Lett.*, vol. 97, no. 15, p. 151108, 2010.

[87] J. P. Sprengers, A. Gaggero, D. Sahin, S. Jahanmirinejad, G. Frucci, F. Mattioli, R. Leoni, J. Beetz, M. Lermer, M. Kamp, S. Höfling, R. Sanjines, and A. Fiore, "Waveguide superconducting single-photon detectors for integrated quantum photonic circuits," *Appl. Phys. Lett.*, vol. 99, no. 18, p. 181110, 2011.

[88] J. Sosniak, "Gallium–Phosphide Films Deposited by Sputtering," *J. Vac. Sci. Technol.*, vol. 7, no. 1, p. 110, Jan. 1970.

[89] J. Gao, Q. Zhan, and A. M. Sarangan, "High-index low-loss gallium phosphide thin films fabricated by radio frequency magnetron sputtering," *Thin Solid Films*, vol. 519, no. 16, pp. 5424–5428, Jun. 2011.

[90] D. A. Mota, G. Hema Chandra, J. Ventura, A. Guedes, and J. Pérez de la Cruz, "Influence of Process Parameters on the RF Sputtered GaP Thin Films," *J. Mater. Sci. Technol.*, vol. 29, no. 9, pp. 821–829, Sep. 2013.

[91] R. M. Biefeld, "The preparation of device quality gallium phosphide by metal organic chemical vapor deposition," *J. Cryst. Growth*, vol. 56, no. 2, pp. 382–388, Jan. 1982.

[92] C. Ratcliff, T. J. Grassman, J. A. Carlin, and S. A. Ringel, "High temperature step-flow growth of gallium phosphide by molecular beam epitaxy and metalorganic chemical vapor deposition," *Appl. Phys. Lett.*, vol. 99, no. 14, p. 141905, 2011.

[93] H. Pogge, B. Kemlage, and R. Broadie, "Preparation and properties of heteroepitaxial GaP films on Si substrates," *Thin Solid Films*, vol. 36, no. 1, pp. 147–150, Jul. 1976.

[94] I. Németh, B. Kunert, W. Stolz, and K. Volz, "Heteroepitaxy of GaP on Si: Correlation of morphology, anti-phase-domain structure and MOVPE growth conditions," *J. Cryst. Growth*, vol. 310, no. 7–9, pp. 1595–1601, Apr. 2008.

[95] S. Farrell, C. Ebert, and D. Dyer, "High growth rate Gallium Phosphide for red LEDs," *2013 Int. Conf. Indium Phosphide Relat. Mater.*, vol. 4, pp. 1–2, May 2013.

[96] A. Mottram and A. R. Peaker, "The growth of gallium phosphide layers of high surface quality by liquid phase epitaxy," *J. Cryst. Growth*, vol. 27, pp. 193–204, Dec. 1974.

[97] C. R. Allen, J. M. Woodall, and J.-H. Jeon, "Results of a gallium phosphide photovoltaic junction with an AR coating under concentration of natural sunlight," *Sol. Energy Mater. Sol. Cells*, vol. 95, no. 9, pp. 2655–2658, Sep. 2011.

[98] V. Narayanan, N. Sukidi, C. Hu, N. Dietz, K. . Bachmann, S. Mahajan, and S. Shingubara, "Growth of gallium phosphide layers by chemical beam epitaxy on oxide patterned (001)silicon substrates," *Mater. Sci. Eng. B*, vol. 54, no. 3, pp. 207–209, Jun. 1998.

[99] A. Bondi, C. Cornet, S. Boyer, T. Nguyen Thanh, A. Létoublon, L. Pedesseau, O. Durand, A. Moreac, A. Ponchet, A. Le Corre, and J. Even, "Raman investigation of GaP–Si interfaces grown by molecular beam epitaxy," *Thin Solid Films*, vol. 541, pp. 72–75, Aug. 2013.

[100] K. Volz, A. Beyer, W. Witte, J. Ohlmann, I. Németh, B. Kunert, and W. Stolz, "GaP-nucleation on exact Si (001) substrates for III/V device integration," *J. Cryst. Growth*, vol. 315, no. 1, pp. 37–47, Jan. 2011.

[101] K. Rivoire, A. Faraon, and J. Vuckovic, "Gallium phosphide photonic crystal nanocavities in the visible," *Appl. Phys. Lett.*, vol. 93, no. 6, p. 063103, 2008.

[102] S. P. R. Clark, P. Ahirwar, F. T. Jaeckel, C. P. Hains, A. R. Albrecht, T. J. Rotter, L. R. Dawson, G. Balakrishnan, P. E. Hopkins, L. M. Phinney, J. Hader, and J. V. Moloney, "Growth and thermal conductivity analysis of polycrystalline GaAs on chemical vapor deposition diamond for use in thermal management of high-power semiconductor lasers," *J. Vac. Sci. Technol. B Microelectron. Nanom. Struct.*, vol. 29, no. 3, p. 03C130, 2011.

[103] J. Meijer, B. Burchard, M. Domhan, C. Wittmann, T. Gaebel, I. Popa, F. Jelezko, and J. Wrachtrup, "Generation of single color centers by focused nitrogen implantation," *Appl. Phys. Lett.*, vol. 87, no. 26, p. 261909, 2005.

[104] K.-M. C. Fu, C. Santori, P. E. Barclay, and R. G. Beausoleil, "Conversion of neutral nitrogen-vacancy centers to negatively charged nitrogen-vacancy centers through selective oxidation," *Appl. Phys. Lett.*, vol. 96, no. 12, p. 121907, 2010.

[105] M. V. Hauf, B. Grotz, B. Naydenov, M. Dankerl, S. Pezzagna, J. Meijer, F. Jelezko, J. Wrachtrup, M. Stutzmann, F. Reinhard, and J. A. Garrido, "Chemical control of the charge state of nitrogen-vacancy centers in diamond," *Phys. Rev. B*, vol. 83, no. 8, p. 081304, Feb. 2011.

[106] D. O'Mahony, M. N. Hossain, J. Justice, E. Pelucchi, A. O'Riordan, B. Roycroft, and B. Corbett, "High index contrast optical platform using gallium phosphide on sapphire: an alternative to SOI?," in *Proc. SPIE 8431, Silicon Photonics and Photonic Integrated Circuits III*, 2012, vol. 8431, p. 84311H–84311H–8.

[107] Private communication with Jianing Sun, J. A. Woollam Co. Inc.

[108] R. Zallen and W. Paul, "Band Structure of Gallium Phosphide from Optical Experiments at High Pressure," *Phys. Rev.*, vol. 134, no. 6A, pp. A1628–A1641, Jun. 1964.

[109] M. Lorenz, G. Pettit, and R. Taylor, "Band Gap of Gallium Phosphide from 0 to 900°K and Light Emission from Diodes at High Temperatures," *Phys. Rev.*, vol. 171, no. 3, pp. 876–881, Jul. 1968.

[110] Y. Molard, F. Dorson, K. a Brylev, M. a Shestopalov, Y. Le Gal, S. Cordier, Y. V Mironov, N. Kitamura, and C. Perrin, "Red-NIR luminescent hybrid poly(methyl methacrylate) containing covalently linked octahedral rhenium metallic clusters.," *Chemistry*, vol. 16, no. 19, pp. 5613–9, May 2010.

[111] L. Liao, D. R. Lim, A. M. Agarwal, X. Duan, K. K. Lee, and L. C. Kimerling, "Optical transmission losses in polycrystalline silicon strip waveguides: Effects of waveguide dimensions, thermal treatment, hydrogen passivation, and wavelength," *J. Electron. Mater.*, vol. 29, no. 12, pp. 1380–1386, Dec. 2000.

[112] S. Hayashi, M. Joshi, and M. Goorsky, "Chemical Mechanical Polishing of Exfoliated III-V Layers," in *ECS Transactions*, 2008, vol. 16, no. 8, pp. 295–302.

[113] I. Aberg, O. O. Olubuyide, J. Li, R. Hull, and J. L. Hoyt, "Fabrication of strained Si/strained SiGe/strained Si heterostructures on insulator by a bond and etch-back technique," *2004 IEEE Int. SOI Conf. (IEEE Cat. No.04CH37573)*, pp. 35–36, 2004.

[114] J. Widiez, M. Rabarot, S. Saada, J.-P. Mazellier, J. Dechamp, V. Delaye, J.-C. Roussin, F. Andrieu, O. Faynot, S. Deleonibus, P. Bergonzo, and L. Clavelier, "Fabrication of Silicon on Diamond (SOD) substrates by either the Bonded and Etched-back SOI (BESOI) or the Smart-Cut^{TM} technology," *Solid. State. Electron.*, vol. 54, no. 2, pp. 158–163, Feb. 2010.

[115] Y.-B. Park, B. Min, K. J. Vahala, and H. A. Atwater, "Integration of Single-Crystal LiNbO3 Thin Film on Silicon by Laser Irradiation and Ion Implantation– Induced Layer Transfer," *Adv. Mater.*, vol. 18, no. 12, pp. 1533–1536, Jun. 2006.

[116] E. Menard, R. G. Nuzzo, and J. A. Rogers, "Bendable single crystal silicon thin film transistors formed by printing on plastic substrates," *Appl. Phys. Lett.*, vol. 86, no. 9, p. 093507, 2005.

[117] A. Ghaffari, A. Hosseini, X. Xu, D. Kwong, H. Subbaraman, and R. T. Chen, "Transfer of micro and nano-photonic silicon nanomembrane waveguide devices on flexible substrates.," *Opt. Express*, vol. 18, no. 19, pp. 20086–95, Sep. 2010.

[118] K. J. Lee, M. J. Motala, M. a. Meitl, W. R. Childs, E. Menard, A. K. Shim, J. A. Rogers, and R. G. Nuzzo, "Large-Area, Selective Transfer of Microstructured Silicon: A Printing-Based Approach to High-Performance Thin-Film Transistors Supported on Flexible Substrates," *Adv. Mater.*, vol. 17, no. 19, pp. 2332–2336, Oct. 2005.

[119] T. Kraus, L. Malaquin, E. Delamarche, H. Schmid, N. D. Spencer, and H. Wolf, "Closing the Gap Between Self-Assembly and Microsystems Using Self-Assembly, Transfer, and Integration of Particles," *Adv. Mater.*, vol. 17, no. 20, pp. 2438–2442, Oct. 2005.

[120] W. Zheng, P. Buhlmann, and H. O. Jacobs, "Sequential shape-and-solder-directed self-assembly of functional microsystems.," *Proc. Natl. Acad. Sci. U. S. A.*, vol. 101, no. 35, pp. 12814–7, Aug. 2004.

[121] J. W. Chung, E. L. Piner, and T. Palacios, "N-Face GaN/AlGaN HEMTs Fabricated Through Layer Transfer Technology," *IEEE Electron Device Lett.*, vol. 30, no. 2, pp. 113–116, Feb. 2009.

[122] P. Chen, Y. Jing, S. S. Lau, D. Xu, L. Mawst, T. L. Alford, C. Paulson, and T. F. Kuech, "High crystalline-quality III-V layer transfer onto Si substrate," *Appl. Phys. Lett.*, vol. 92, no. 9, p. 092107, 2008.

[123] M. Rabarot, J. Widiez, S. Saada, J.-P. Mazellier, C. Lecouvey, J.-C. Roussin, J. Dechamp, P. Bergonzo, F. Andrieu, O. Faynot, S. Deleonibus, L. Clavelier, and J. P. Roger, "Silicon-On-Diamond layer integration by wafer bonding technology," *Diam. Relat. Mater.*, vol. 19, no. 7–9, pp. 796–805, Jul. 2010.

[124] J. H. Epple, C. Sanchez, T. Chung, K. Y. Cheng, and K. C. Hsieh, "Dry etching of GaP with emphasis on selective etching over AlGaP," *J. Vac. Sci. Technol. B Microelectron. Nanom. Struct.*, vol. 20, no. 6, p. 2252, 2002.

[125] A. R. Clawson, "Guide to references on III–V semiconductor chemical etching," *Mater. Sci. Eng. R Reports*, vol. 31, no. 1–6, pp. 1–438, Jan. 2001.

[126] M. Konagai, M. Sugimoto, and K. Takahashi, "High-efficiency GaAs thin film solar cells by peeled film technology," *J. Cryst. Growth*, vol. 45, pp. 277–280, 1978.

[127] J. J. Schermer, G. J. Bauhuis, P. Mulder, W. J. Meulemeesters, E. Haverkamp, M. M. a. J. Voncken, and P. K. Larsen, "High rate epitaxial lift-off of InGaP films from GaAs substrates," *Appl. Phys. Lett.*, vol. 76, no. 15, p. 2131, 2000.

[128] J. J. Schermer, P. Mulder, G. J. Bauhuis, M. M. a. J. Voncken, J. van Deelen, E. Haverkamp, and P. K. Larsen, "Epitaxial Lift-Off for large area thin film III/V devices," *Phys. Status Solidi*, vol. 202, no. 4, pp. 501–508, Mar. 2005.

[129] I. Pollentier, L. Buydens, P. Van Daele, and P. Demeester, "Fabrication of a GaAs-AlGaAs GRIN-SCH SQW laser diode on silicon by epitaxial lift-off," *IEEE Photonics Technol. Lett.*, vol. 3, no. 2, pp. 115–117, Feb. 1991.

[130] C.-W. Cheng, K.-T. Shiu, N. Li, S.-J. Han, L. Shi, and D. K. Sadana, "Epitaxial lift-off process for gallium arsenide substrate reuse and flexible electronics.," *Nat. Commun.*, vol. 4, p. 1577, Jan. 2013.

[131] E. Yablonovitch, T. Gmitter, J. P. Harbison, and R. Bhat, "Extreme selectivity in the lift-off of epitaxial GaAs films," *Appl. Phys. Lett.*, vol. 51, no. 26, p. 2222, 1987.

[132] A. Ersen, I. Schnitzer, E. Yablonovitch, and T. Gmitter, "Direct bonding of GaAs films on silicon circuits by epitaxial liftoff," *Solid. State. Electron.*, vol. 36, no. 12, pp. 1731–1739, Dec. 1993.

[133] C. Santori, K.-M. C. Fu, P. E. Barclay, and R. G. Beausoleil, "Structures in diamond for optical manipulation of nitrogen-vacancy centers," *Proc. SPIE 7225, Adv. Opt. Concepts Quantum Comput. Mem. Commun. II*, vol. 7225, p. 72250L–72250L–8, Feb. 2009.

[134] R. M. Gibb and P. D. Augustus, "Preferential etching of dislocations and stacking faults in gallium phosphide," *J. Electron. Mater.*, vol. 5, no. 6, pp. 585–599, 1976.

[135] H. Morota and S. Adachi, "Properties of GaP(001) surfaces treated in aqueous HF solutions," *J. Appl. Phys.*, vol. 101, no. 11, p. 113518, 2007.

[136] A. F. Oskooi, D. Roundy, M. Ibanescu, P. Bermel, J. D. Joannopoulos, and S. G. Johnson, "Meep: A flexible free-software package for electromagnetic simulations by the FDTD method," *Comput. Phys. Commun.*, vol. 181, no. 3, pp. 687–702, Mar. 2010.

[137] MEEP. Web. Accessed Aug. 22, 2014. http://ab-initio.mit.edu/wiki/index.php/Meep.

[138] Q. Xu, D. Fattal, and R. G. Beausoleil, "Silicon microring resonators with 1.5-μm radius," *Opt. Express*, vol. 16, no. 6, p. 4309, Mar. 2008.

[139] S. J. Pearton, "Comparison of dry etching techniques for III-V semiconductors in CH4, H2, Ar plasmas," *J. Electrochem. Soc.*, vol. 134, no. 2, p. 19960201, 1996.

[140] J. W. Lee, "Cl_2-Based Dry Etching of GaAs, AlGaaAs, and GaP," *J. Electrochem. Soc.*, vol. 143, no. 6, p. 2010, 1996.

[141] Y. B. Hahn, J. W. Lee, G. A. Vawter, R. J. Shul, C. R. Abernathy, D. C. Hays, E. S. Lambers, and S. J. Pearton, "Reactive ion beam etching of GaAs and related compounds in an inductively coupled plasma of Cl_2–Ar mixture," *J. Vac. Sci. Technol. B Microelectron. Nanom. Struct.*, vol. 17, no. 2, p. 366, 1999.

[142] A. E. Grigorescu and C. W. Hagen, "Resists for sub-20-nm electron beam lithography with a focus on HSQ: state of the art.," *Nanotechnology*, vol. 20, no. 29, p. 292001, Jul. 2009.

[143] T. Barwicz and H. I. Smith, "Evolution of line-edge roughness during fabrication of high-index-contrast microphotonic devices," *J. Vac. Sci. Technol. B Microelectron. Nanom. Struct.*, vol. 21, no. 6, p. 2892, 2003.

[144] M. G. Wood, L. Chen, J. R. Burr, and R. M. Reano, "Optimization of electron beam patterned hydrogen silsesquioxane mask edge roughness for low-loss silicon waveguides," *J. Nanophotonics*, vol. 8, no. 1, p. 083098, Jan. 2014.

[145] A. E. Grigorescu and C. W. Hagen, "Resists for sub-20-nm electron beam lithography with a focus on HSQ: state of the art.," *Nanotechnology*, vol. 20, no. 29, p. 292001, Jul. 2009.

[146] D. S. Weiss, V. Sandoghdar, J. Hare, V. Lefèvre-Seguin, J. M. Raimond, and S. Haroche, "Splitting of high-Q Mie modes induced by light backscattering in silica microspheres.," *Opt. Lett.*, vol. 20, no. 18, pp. 1835–7, Sep. 1995.

[147] M. L. Gorodetsky, A. D. Pryamikov, and V. S. Ilchenko, "Rayleigh scattering in high-Q microspheres," *J. Opt. Soc. Am. B*, vol. 17, no. 6, p. 1051, 2000.

[148] A. M. Edmonds, U. F. S. D'Haenens-Johansson, R. J. Cruddace, M. E. Newton, K.-M. C. Fu, C. Santori, R. G. Beausoleil, D. J. Twitchen, and M. L. Markham, "Production of oriented nitrogen-vacancy color centers in synthetic diamond," *Phys. Rev. B*, vol. 86, no. 3, p. 035201, Jul. 2012.

[149] T. Fukui, Y. Doi, T. Miyazaki, Y. Miyamoto, H. Kato, T. Matsumoto, T. Makino, S. Yamasaki, R. Morimoto, N. Tokuda, M. Hatano, Y. Sakagawa, H. Morishita, T. Tashima, S. Miwa, Y. Suzuki, and N. Mizuochi, "Perfect selective alignment of nitrogen-vacancy centers in diamond," *Appl. Phys. Express*, vol. 7, no. 5, p. 055201, May 2014.

[150] M. Lesik, J.-P. Tetienne, A. Tallaire, J. Achard, V. Mille, A. Gicquel, J.-F. Roch, and V. Jacques, "Perfect preferential orientation of nitrogen-vacancy defects in a synthetic diamond sample," *Appl. Phys. Lett.*, vol. 104, no. 11, p. 113107, Mar. 2014.

[151] L. C. Bassett, F. J. Heremans, C. G. Yale, B. B. Buckley, and D. D. Awschalom, "Electrical Tuning of Single Nitrogen-Vacancy Center Optical Transitions Enhanced by Photoinduced Fields," *Phys. Rev. Lett.*, vol. 107, no. 26, p. 266403, Dec. 2011.

[152] P. Tamarat, T. Gaebel, J. Rabeau, M. Khan, a. Greentree, H. Wilson, L. Hollenberg, S. Prawer, P. Hemmer, F. Jelezko, and J. Wrachtrup, "Stark Shift Control of Single Optical Centers in Diamond," *Phys. Rev. Lett.*, vol. 97, no. 8, p. 083002, Aug. 2006.

[153] V. M. Acosta, C. Santori, A. Faraon, Z. Huang, K.-M. C. Fu, A. Stacey, D. A. Simpson, K. Ganesan, S. Tomljenovic-Hanic, A. D. Greentree, S. Prawer, and R. G. Beausoleil, "Dynamic Stabilization of the Optical Resonances of Single Nitrogen-Vacancy Centers in Diamond," *Phys. Rev. Lett.*, vol. 108, no. 20, p. 206401, May 2012.

[154] M. Mitchell, A. C. Hryciw, and P. E. Barclay, "Cavity optomechanics in gallium phosphide microdisks," *Appl. Phys. Lett.*, vol. 104, no. 14, p. 141104, Apr. 2014.

[155] Y. M. Georgiev, W. Henschel, A. Fuchs, and H. Kurz, "Surface roughness of hydrogen silsesquioxane as a negative tone electron beam resist," *Vacuum*, vol. 77, no. 2, pp. 117–123, Jan. 2005.

[156] S. Mosor, J. Hendrickson, B. C. Richards, J. Sweet, G. Khitrova, H. M. Gibbs, T. Yoshie, A. Scherer, O. B. Shchekin, and D. G. Deppe, "Scanning a photonic crystal slab nanocavity by condensation of xenon," *Appl. Phys. Lett.*, vol. 87, no. 14, p. 141105, 2005.

[157] K. Srinivasan and O. Painter, "Optical fiber taper coupling and high-resolution wavelength tuning of microdisk resonators at cryogenic temperatures," *Appl. Phys. Lett.*, vol. 90, no. 3, p. 031114, 2007.

[158] E. P. Gibson and A. J. Rest, "The determination of the refractive indices of frozen gas matrices at 12 k by emission spectroscopy," *Chem. Phys. Lett.*, vol. 73, no. 2, pp. 294–296, Jul. 1980.

[159] A. C. Sinnock, "Refractive indices of the condensed rare gases, argon, krypton and xenon," *J. Phys. C Solid State Phys.*, vol. 13, no. 12, pp. 2375–2391, Apr. 1980.

[160] A. T. Collins, M. F. Thomaz, and M. I. B. Jorge, "Luminescence decay time of the 1.945 eV centre in type Ib diamond," *J. Phys. C Solid State Phys.*, vol. 16, no. 11, pp. 2177–2181, Apr. 1983.

[161] A. Yariv, "Universal relations for coupling of optical power between microresonators and dielectric waveguides," *Elecronics Lett.*, vol. 36, no. 4, pp. 1–2, 2000.

[162] J. M. Choi, R. K. Lee, and A. Yariv, “Control of critical coupling in a ring resonator-fiber configuration: application to wavelength-selective switching, modulation, amplification, and oscillation.,” *Opt. Lett.*, vol. 26, no. 16, pp. 1236–8, Aug. 2001.

[163] A. Yariv, “Critical coupling and its control in optical waveguide-ring resonator systems,” *IEEE Photonics Technol. Lett.*, vol. 14, no. 4, pp. 483–485, Apr. 2002.

[164] J. T. Choy, B. J. M. Hausmann, T. M. Babinec, I. Bulu, M. Khan, P. Maletinsky, A. Yacoby, and M. Lončar, “Enhanced single-photon emission from a diamond–silver aperture,” *Nat. Photonics*, vol. 5, no. 12, pp. 738–743, Oct. 2011.

Appendix

A Process flows

A.1 Creation of NV^- centers via ion implantation and two-step anneal

Procedure	**Steps & Conditions**
Clean	• 20 min in hot Piranha (3:1 H_2SO4:H_2O_2, freshly prepared) • DI H_2O rinse, N_2 blow dry
Implantation	• Mount in center of 4 inch Si wafer with Kapton tape • CVD diamond: $N^+/10^{10}$-$10^{12}cm^{-2}$/ 10 kV / 7° off-axis • HPHT diamond: $N^+/10^{12}cm^{-2}$/ 50 kV / 7° off-axis
Clean	• Sonication in acetone • Acetone/IPA/DI H_2O rinse • 20 min in Piranha • DI H_2O rinse, N_2 blow dry
High-temperature anneal	• 1 hour at 850°C in 95% Ar / 5% H_2
Inspection	• Photoluminescence measurement to determine presence of NV^0 (electronic-grade CVD substrates) or NV^0 & NV^- (HPHT)
Clean	• Sonication in acetone • Acetone/IPA/DI H_2O rinse • 20 min in Piranha • DI H_2O rinse, N_2 blow dry
Low-temperature anneal	• 10 hours at 460°C in air
Inspection	• Photoluminescence measurement to determine presence of NV^-

A.2 Nano-crystalline GaP photonic devices on diamond

Procedure	**Steps & Conditions**
Clean	• Sonication in acetone • Acetone/IPA/DI H_2O rinse, N_2 blow dry
Electron beam lithography	• Pre-bake: 5 min at 110°C • P20 adhesion promoter: Spread 2 s at 500 rpm Spin 25 s at 6500 rpm • Ma-N2401: Spread 2 s at 500 rpm Spin 55 s at 6500 rpm Bake 5 min at 110°C • Exposure: Dose 480 μCcm^{-2} • Development: 70 s in MF319 DI H_2O rinse N_2 blow dry
Inspection	• Profilometry to measure resist thickness • SEM
Cl_2/Ar ICP-RIE	• Descum: 30 s • Chamber conditioning: 10 min • Test etch patterned GaP bulk sample • GaP Ar/Cl_2 etch: 1 sccm Cl_2/7.5 sccm Ar 4 mT chamber pressure/ 1 T He back pressure 50 W RF / 100 W ICP 40 s
Inspection	• Profilometry to confirm complete etch • SEM
Clean	• Resist removal: 20 min in 1165 resist remover at 80°C • Acetone/IPA/DI H_2O rinse, N_2 blow dry
Inspection	• Profilometry to confirm resist removal • SEM

A.3 GaP waveguides on SiO_2\Si

Procedure	Steps & Conditions
Cleaving	• Cleave MBE GaP\SiO_2\Si substrate into mm^2- sized substrates
Clean	• Sonication in acetone • Acetone/IPA/DI H_2O rinse, N_2 blow dry
Electron beam lithography	• Pre-bake: 5 min at 180°C • P20 adhesion promoter: Spread 3 s at 500 rpm Spin 25 s at 4000 rpm • Ma-N2401: Spread 3 s at 500 rpm Spin 60 s at 3250 rpm Bake 5 min at 110°C • Exposure: Dose 480 μCcm^{-2} • Development: 70 s in MF319 DI H_2O rinse N_2 blow dry
Inspection	• Profilometry to measure resist thickness • SEM
Cl_2/Ar ICP-RIE	• Descum: 60 s • Chamber conditioning: 10 min • Test etch patterned GaP bulk sample • GaP Ar/Cl_2 etch: 1 sccm Cl_2/7.5 sccm Ar 4 mT chamber pressure/ 1 T He back pressure 50 W RF / 100 W ICP 40 s
Inspection	• Profilometry to confirm complete etch • SEM
Clean	• Resist removal: 20 min in 1165 resist remover at 80°C • Acetone/IPA/DI H_2O rinse, N_2 blow dry
Inspection	• Profilometry to confirm complete resist removal • SEM
Clean	• Acetone/IPA/DI H_2O rinse, N_2 blow dry
Spin PMMA cladding	• Pre-bake: 5 min at 180°C • 495k A2.5: Spread 3 s at 500 rpm Spin 60 s at 5000 rpm Bake 3 min at 180°C

A.4 Undercut single-crystalline GaP resonators

Procedure	**Steps & Conditions**
Cleaving	• Cleave MBE GaP\AlGaP\GaP substrate into mm^2- sized pieces
Clean	• Sonication in acetone • Acetone/IPA/DI H_2O rinse, N_2 blow dry
Electron beam lithography	• HMDS treatment • Ma-N2403: Spread 5 s at 500 rpm Spin 30 s at 5500 rpm Bake 5 min at 100°C • Exposure: Dose 420 μCcm^{-2} • Development: 70 s in MF319 DI H_2O rinse N_2 blow dry
Inspection	• Profilometry to measure resist thickness • SEM
Cl_2/Ar ICP-RIE	• Descum: 60 s • Chamber conditioning: 10 min • Test etch patterned GaP bulk sample • GaP Ar/Cl_2 etch: 1 sccm Cl_2/7.5 sccm Ar 4 mT chamber pressure/ 1 T He back pressure 50 W RF / 100 W ICP 40 s
Inspection	• Profilometry to confirm complete etch • SEM
Clean	• Resist removal: 20 min in 1165 resist remover at 80°C • Profilometry to confirm resist removal • Acetone/IPA/DI H_2O rinse, N_2 blow dry
Inspection	• SEM
Clean	• Acetone/IPA/DI H_2O rinse, N_2 blow dry
Undercut	• 1:100 HF (49%): DI H_2O: 30 s to 60 s
Inspection	• SEM

A.5 GaP transfer via etch-back and HF vapor release

Procedure	Steps & Conditions
Cleaving	• Cleave MBE GaP\AlGaP\GaP substrate into mm^2- sized substrates
Clean	• Sonication in acetone • Acetone/IPA/DI H_2O rinse & N_2 blow dry
Deposit front side protective layers	• 1 μm SiO_2 PECVD: 14 min WNF SiOx-Standard • 300 nm Ti electron beam evaporation • Prebake: 5 min at 110°C AZ1512: Spread 3 s at 500 rpm Spin 30 s at 5500 rpm Bake 1:30 min at 110°C
Back side lapping & polishing	• Lapping: 3 μm Al_2O_3 slurry, 7% lap to ~ 120 μm thickness • Polishing: 0.3 μm Al_2O_3 slurry, 7% polish until smooth
Clean	• Sonication in acetone • Acetone/IPA/DI H_2O rinse & N_2 blow dry
Deposit front side protective layer and back side hard mask	• 500 nm SiO_2 PECVD on front: 7 min WNF SiOx-Standard • 1 μm SiO_2 PECVD on back: 14 min WNF SiOx-Standard
Back side photolithography	• Prebake: 5 min at 110°C • AZ1512: Spread 3 s at 500 rpm Spin 30 s at 5500 rpm Bake 1:30 min at 110°C • Exposure: 1x2, 18 mW (direct write) • Develop: 1 min in 1:4 AZ340:DI H_2O DI H_2O rinse N_2 blow dry
Back side hard mask etch	• SiO_2 WNF CHF_3/CF_4 RIE: 33 min
Backside window etch	• 0.33 M $K_3Fe(CN)_6$: 1 M KOH at 80°C: etch until ~ 10 μm GaP remain in windows
Removal of front side protective layers	• 1 min in 10:1 BOE • DI H_2O rinse, N_2 blow dry
Front side photolithography	• Prebake: 5 min at 110°C • AZ1512:

	Spread 3 s at 500 rpm Spin 30 s at 5500 rpm Bake 1:30 min at 110°C • Exposure: 1x2, 18 mW (direct write, aligned to back) • Develop: 1 min in 1:4 AZ340:DI H_2O DI H_2O rinse N_2 blow dry
Front side etch	• GaP SF_6/BCl_3 ICP-RIE (at HP labs): 2 min
Clean	• Resist removal: 20 min in 1165 resist remover • O_2 descum (at HP labs): 3 min • IPA/ DI H_2O rinse, N_2 blow dry
Back side etch	• GaP SF_6/BCl_3 ICP-RIE (at HP labs): etch until windows open
Diamond clean	• Acetone/IPA/DI H_2O rinse • 20 min in Piranha (3:1 $H_2SO4:H_2O_2$) • DI H_2O rinse, N_2 blow dry
HF vapor release	• 49% HF vapor until GaP released
Clean	• Acetone/IPA/DI H_2O rinse, N_2 blow dry

A.6 GaP transfer via epitaxial lift-off

Procedure	Steps & Conditions
Cleaving	• Cleave MBE GaP\AlGaP\GaP substrate into mm^2- sized substrates
Clean	• Sonication in acetone • Acetone/IPA/DI H_2O rinse, N_2 blow dry
Photolithography	• Pre-bake: 5 min at 110°C • AZ1512: Spread 3 s at 500 rpm Spin 30 s at 5500 rpm Bake 1 min at 110°C • Expose: 4 s • Develop: 1 min in 1:4 AZ340:DI H_2O DI H_2O rinse N_2 blow dry
Inspection	• Profilometry to measure photoresist thickness • Optical microscopy
Descum	• 2:30 min in O_2 plasma (barrel etcher)
Cl_2/Ar ICP-RIE	• Chamber conditioning: 10 min • Test etch patterned GaP bulk sample • GaP Ar/Cl_2 etch: 1 sccm Cl_2 / 7.5 sccm Ar 4 mT chamber pressure/ 1 T He back pressure 50 RF / 100 W ICP 3 x 40 s with 5 min cool-down after each etch
Inspection	• Profilometry to measure etch depth • Optical microscopy
HF release	• 1:100 HF (49%): DI H_2O until released
Diamond clean	• Acetone/IPA/DI H_2O rinse • 20 min in hot Piranha (3:1 H_2SO_4:H_2O_2, freshly prepared) • 15 min in fuming sulfuric acid and potassium nitrate (20 ml H_2SO_4 : 1 g KNO_3, freshly prepared) • DI H_2O rinse, N_2 blow dry
Manual transfer of GaP onto diamond	• Transfer released GaP from HF to DI H_2O rinse • Transfer released GaP onto diamond
Inspection	• Optical microscopy
Clean	• Resist removal: 20 min in 1165 resist remover at 80°C • Acetone/IPA/DI H_2O rinse & N_2 blow dry
Inspection	• Profilometry to confirm complete photoresist removal • Optical microscopy • Photoluminescence measurements through GaP to confirm presence of NV^-

A.7 Fabrication of single-crystalline GaP resonator-waveguide structures on mechanical-grade diamond

Procedure	Steps & Conditions
	• E6 CVD substrate with NV^- and transferred GaP sheet
Clean	• Acetone/IPA/DI H_2O rinse, N_2 blow dry
Electron beam lithography	• PECVD SiO_2 adhesion layer: 7 s WNF SiOx-Standard • Pre-bake: 5 min at 150°C • HSQ, 6%: Spread 1 s at 500 rpm Spin 40 s at 5750 rpm Bake 5 min at 80°C • Expose: 2300 μCcm^{-2} • Develop: 4 min in TMAH DI H_2O rinse IPA rinse N_2 blow dry
Inspection	• Profilometry to measure resist thickness • SEM on-chip test structures
Cl_2/Ar ICP-RIE	• Chamber conditioning: 10 min • Test etch patterned GaP bulk sample • GaP Ar/Cl_2 etch: 1 sccm Cl_2/9.5 sccm Ar 3 mT chamber pressure/ 1 T He back pressure 75 W RF / 55 W ICP chuck cooled to 18°C 1:40 min
Inspection	• Profilometry to confirm complete GaP etch • SEM on-chip test structures
Diamond ICP-RIE	• Chamber conditioning: 10 min • Diamond O_2 etch: 20 sccm O_2 25 mT chamber pressure / 2 T He pressure 10 RF / 1500 W ICP 12 min
Inspection	• Profilometry to confirm diamond etch • SEM on-chip test structures

A.8 Fabrication of single-crystalline GaP resonator-waveguide structures on CVD diamond

Procedure	Steps & Conditions
	• E6 CVD diamond substrate with NV^- and transferred GaP sheet
Clean	• Acetone/IPA/DI H_2O rinse, N_2 blow dry
Electron beam lithography	• PECVD SiO_2 adhesion layer: 7 s WNF SiOx-Standard • Pre-bake: 5 min at 150°C • HSQ, 6%: Spread 1 s at 500 rpm Spin 40 s at 7500 rpm Bake 5 min at 80°C • Expose: 2300 μCcm^{-2} • Develop: 4 min in TMAH DI H_2O rinse IPA rinse N_2 blow dry
Inspection	• Profilometry to measure resist thickness • SEM on-chip test structures
Cl_2/Ar ICP-RIE	• Chamber conditioning: 10 min • Test etch patterned GaP bulk sample • GaP Ar/Cl_2 etch: 1 sccm Cl_2/9.5 sccm Ar 3 mT chamber pressure/ 1 T He back pressure 75 W RF / 55 W ICP chuck cooled to 18°C 1:40 min
Inspection	• Profilometry to confirm complete GaP etch • SEM on-chip test structures
Diamond ICP-RIE	• Chamber conditioning: 10 min • Diamond O_2 etch: 20 sccm O_2 25 mT chamber pressure / 2 T He pressure 11 RF / 1500 W ICP 12 min
Inspection	• Profilometry to confirm diamond etch • SEM on-chip test structures

B Design of grating structure and taper regions for hybrid GaP\diamond networks

While future integrated GaP networks on diamond may rely on photon collection with on-chip superconducting single photon detectors [86], [87], the device structures fabricated in this thesis depend on grating couplers, in which light is diffracted out of plane by a periodic array of etched GaP slabs, for the off-chip collection of any NV^- emission or transmitted light. Fig. B.1.1(a) shows the structure of a 2-dimensional (2-D) grating which is utilized for the preliminary design of simpler, periodic grating structures with period $\lambda_{grating}$ and duty cycle *d*. The duty cycle is defined as:

$$d = \frac{w_{GaP}}{\lambda_{grating}} \qquad \text{Eq. B.1}$$

where w_{GaP} is the width of the remaining GaP slab in each period.

The fraction of the flux coupled out-of-plane versus the flux into the grating structures as function of grating period and duty cycle is displayed in Fig. B.1.1(b). The highest coupling can be found for a grating period of 280 nm and a duty cycle between 0.4 and 0.5.

The grating couplers are 2 μm by 2 μm wide to allow for all of a 1 μm^2 diameter focused laser beam to couple into the waveguides. 2-D continuous taper structures are employed for adaption of the waveguide width from the width of the grating to the final waveguide coupled to the resonator. A short taper length (< 10 μm) is preferred to allow for the integration of a large number of devices on the small diamond substrates. 2-D simulations of the flux transmitted from a 100 nm wide waveguide to the end of the tapered regions indicate that 5 μm long tapers are sufficient (> 97% transmission).

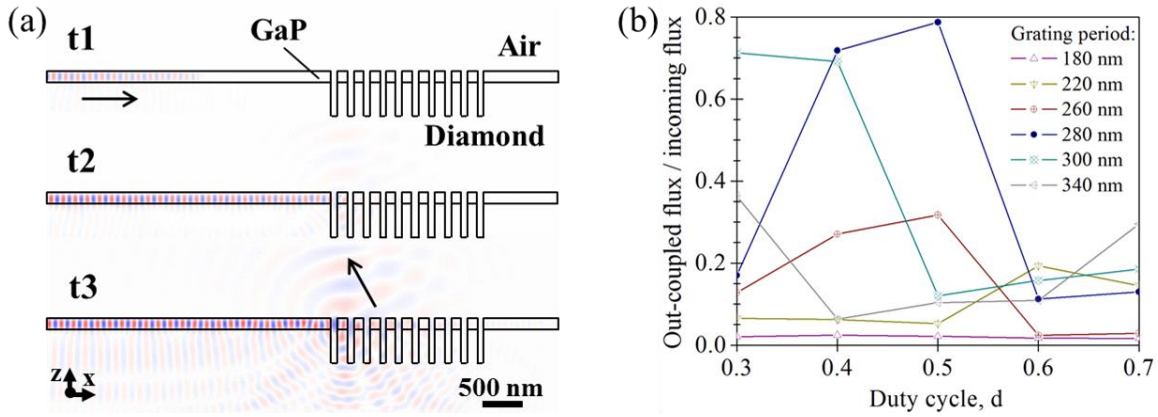

Fig. B.1.1: 2-D FDTD simulation of GaP grating structures on etched diamond substrates. (a) Cross-sectional view of GaP waveguide and grating with electric field at different simulation times. (b) Ratio of flux coupled into the area above the grating structure vs. incoming flux as function of grating period and duty cycle.

C MEEP Scripts

C.1 Quasi-2-D modes of a GaP resonator on diamond

```
(reset-meep)

(define-param h_GaP 1.4)                ; height GaP
(define-param r_GaP 5)                  ; radius GaP disk
(define-param n_GaP 3.31)               ; refractive index GaP

(define-param h_SiO2 0.4)               ; height SiO2 resist
(define-param n_SiO2 1.54)              ; refactive index SiO2

(define-param n_air 1)                  ; refractive index air

(define-param h_diamond_etch 5.5)       ; height diamond etch
(define-param r_diamond_base 11)        ; width diamond at base to determine slope
(define-param n_diamond 2.4)            ; refractive index diamond

(define-param w_PML 1)                  ; width PML
(define-param pad 8)                    ; space between resonator and PML

(define-param res 10)                   ; resolution for simulation
(define-param rt 3000)                  ; run time

(define-param fcen 0.15699)             ; center frequency (637nm)
(define-param df 0.02)                  ; width frequency (620nm .. 660nm)

(define-param mode 11)

(define sr (+ r_GaP pad w_PML))
(define sh (+ (* 2 (+ pad w_PML)) h_GaP h_diamond_etch))

(set! dimensions CYLINDRICAL)

(set! geometry-lattice (make lattice (size sr no-size sh)))

(set-param! m mode)

(set! default-material air)

(set! Geometry
        (list
                (make block     (center 0 0 (/ h_GaP 2) )               ; GaP disk
                                (size (* 2 r_GaP) infinity h_GaP)
                                (material (make dielectric (index n_GaP)))
                )
                (make block     (center 0 0 (+ (/ h_SiO2 2) h_GaP))     ; HSQ resist
                                (size (* 2 r_GaP) infinity h_SiO2)
                                (material (make dielectric (index n_SiO2)))
                )
                (make cone      (center 0 0 (/ h_diamond_etch -2))      ; etched diamond substrate
                                (radius2 r_GaP)                         ; with cone shape
                                (radius r_diamond_base)
                                (height h_diamond_etch)
                                (material (make dielectric (index n_diamond)))
```

```
                )
                (make block     (center   0 0 (+ (* -1 h_diamond_etch) (* -0.5 sh)))    ; diamond substrate
                                (size (* 2 sr) infinity sh)
                                (material (make dielectric (index n_diamond)))
                )
        )
)

(set! pml-layers
        (list
                (make pml       (thickness w_PML))
        )
)

(set-param! resolution res)

(set! sources                                                                   ; define appropriate for TE/TM
        (list
                (make source    (src    (make gaussian-src      (frequency fcen)
                                                                (fwidth df)
                                        )
                                )
                                (component Ez)
                                (center (- r_GaP 0.5) 0 (/ h_GaP 3))
                                (size 0 0 0)
                )
        )
)

(run-sources+ rt
        (in-volume
                (volume (center 0)
                        (size (* 2 sr) 0 sh)
                )
                (at-beginning output-epsilon)
                (at-end output-efield-z)
                (after-sources (harminv Ez (vector3 (- r_GaP 1) 0 (+ h_air (/ h_GaP 2))) fcen df))          ; output Q
        )
)
```

C.2 3-D coupling between ring resonator waveguide and straight waveguide

```
(reset-meep)

(define-param nGaP 3.31)                ; refractive index GaP
(define-param hGaP 1.4)                 ; height GaP layer
(define-param rGaP 5)                   ; radius of GaP disk
(define-param lGaP_WG 100)              ; length GaP waveguides for ring structure
(define-param wGaP_ring 1.2)            ; width of the GaP ring waveguide

(define-param wGaP_WG 1)                ; width of the GaP waveguide
(define-param gap 0.5)                  ; gap between waveguide and disk resonator

(define-param nDiamond 2.4)             ; refractive index diamond substrate
(define-param diamond_etch 5.5)         ; etch depth diamond

(define-param padx 10)                  ; padding between resonator and PML in x
(define-param pady 8)                   ; padding between resonator and PML in y
(define-param padz 8)                   ; padding between resonator and PML in z
(define-param wPML 4)                   ; width PML

(define csx (* 2 (+ padx wPML rGaP)))                                   ; define cell size in x
(define csy (+ (* 2 (+ pady wPML)) lGaP_WG rGaP gap wGaP_WG))           ; define cell size in y
(define csz (* 2 (+ padz wPML)))                                        ; define cell size in z

(define-param res 10)                                   ; resolution

(set! geometry-lattice                                  ; define cell
        (make lattice (size csx csy csz)
        )
)

(define-param no-waveguide false)       ; measure initial flux into the ring waveguide without reflection from
                                        ; the straight waveguide
(set! geometry
        (if no-waveguide
                (list
                        (make cylinder  (center 0 (- (/ csy 2) wPML lGaP_WG) (/ hGaP 2))
                                        (height hGaP)
                                        (radius rGaP)
                                        (material (make dielectric (index nGaP)))
                        )
                        (make cylinder  (center 0 (- (/ csy 2) wPML lGaP_WG) (/ diamond_etch -2))
                                (height diamond_etch)
                                (radius rGaP)
                                (material (make dielectric (index nDiamond)))
                        )
                        (make cylinder  (center 0 (- (/ csy 2) wPML lGaP_WG) (+ (/ diamond_etch -1) (/ (+
                                        hGaP diamond_etch) 2)))
                                        (height (+ hGaP diamond_etch))
                                        (radius (- rGaP wGaP_ring))
                                        (material air)
                        )
```

```
                (make block     (center 0 (- (/ csy 2) wPML (- lGaP_WG rGaP)) (+ (/ diamond_etch -1)
                                (/ (+ hGaP diamond_etch) 2)))
                                (size (* 2 rGaP) (* 2 rGaP) (+ hGaP diamond_etch))
                                (material air)
                )
                (make block     (center (+ (* rGaP -1) (/ wGaP_ring 2)) (- (/ csy 2) (/ (+ wPML
                                lGaP_WG) 2)) (/ hGaP 2))
                                (size wGaP_ring (+ lGaP_WG wPML) hGaP)
                                (material (make dielectric (index nGaP)))
                )
                (make block     (center (+ (* rGaP -1) (/ wGaP_ring 2)) (- (/ csy 2) (/ (+ wPML
                                lGaP_WG) 2)) (/ diamond_etch -2))
                                (size wGaP_ring (+ lGaP_WG wPML) diamond_etch)
                                (material (make dielectric (index nDiamond)))
                )
                (make block     (center (- rGaP (/ wGaP_ring 2)) (- (/ csy 2) (/ (+ wPML lGaP_WG) 2))
                                (/ hGaP 2))
                                (size wGaP_ring (+ lGaP_WG wPML) hGaP)
                                (material (make dielectric (index nGaP)))
                )
                (make block     (center (- rGaP (/ wGaP_ring 2)) (- (/ csy 2) (/ (+ wPML lGaP_WG) 2))
                                (/ diamond_etch -2))
                                (size wGaP_ring (+ lGaP_WG wPML) diamond_etch)
                                (material (make dielectric (index nDiamond)))
                )
)
(list
        (make cylinder  (center 0 (- (/ csy 2) wPML lGaP_WG) (/ hGaP 2))    ; define GaP cylinder
                        (height hGaP)
                        (radius rGaP)
                        (material (make dielectric (index nGaP)))
        )
        (make cylinder  (center 0 (- (/ csy 2) wPML lGaP_WG) (/ diamond_etch -2))  ; diamond pedestal
                        (height diamond_etch)
                        (radius rGaP)
                        (material (make dielectric (index nDiamond)))
        )
        (make cylinder  (center 0 (- (/ csy 2) wPML lGaP_WG) (+ (/ diamond_etch -1) (/ (+ hGaP
                        diamond_etch) 2)))
                        (height (+ hGaP diamond_etch))
                        (radius (- rGaP wGaP_ring))
                        (material air)
        )
        (make block     (center 0 (- (/ csy 2) wPML (- lGaP_WG rGaP)) (+ (/ diamond_etch -1) (/ (+
                        hGaP diamond_etch) 2)))                         ; define half-circle
                        (size (* 2 rGaP) (* 2 rGaP) (+ hGaP diamond_etch))
                        (material air)
        )
        (make block     (center (+ (* rGaP -1) (/ wGaP_ring 2)) (- (/ csy 2) (/ (+ wPML lGaP_WG) 2)) (/
                        hGaP 2))                                        ; define GaP waveguide on the left
                        (size wGaP_ring (+ lGaP_WG wPML) hGaP)
                        (material (make dielectric (index nGaP)))
        )
```

```
		(make block	(center (+ (* rGaP -1) (/ wGaP_ring 2)) (- (/ csy 2) (/ (+ wPML lGaP_WG) 2)) (/
				diamond_etch -2))		; define diamond waveguide on the left
				(size wGaP_ring (+ lGaP_WG wPML) diamond_etch)
				(material (make dielectric (index nDiamond)))
		)
		(make block	(center (- rGaP (/ wGaP_ring 2)) (- (/ csy 2) (/ (+ wPML lGaP_WG) 2)) (/ hGaP
				2))		; define GaP waveguide on the right
				(size wGaP_ring (+ lGaP_WG wPML) hGaP)
				(material (make dielectric (index nGaP)))
		)
		(make block	(center (- rGaP (/ wGaP_ring 2)) (- (/ csy 2) (/ (+ wPML lGaP_WG) 2)) (/
				diamond_etch -2))		; define diamond waveguide on the right
				(size wGaP_ring (+ lGaP_WG wPML) diamond_etch)
				(material (make dielectric (index nDiamond)))
		)
		(make block	(center 0 (- (/ csy 2) wPML lGaP_WG rGaP gap (/ wGaP_WG 2)) (/ hGaP 2))
						; define GaP waveguide to couple to
				(size infinity wGaP_WG hGaP)
				(material (make dielectric (index nGaP)))
		)
		(make block	(center 0 (- (/ csy 2) wPML lGaP_WG rGaP gap (/ wGaP_WG 2)) (/
				diamond_etch -2))		; define diamond waveguide to couple to
				(size infinity wGaP_WG diamond_etch)
				(material (make dielectric (index nDiamond)))
		)
		(make block	(center 0 0 (- (/ csz -2) diamond_etch))		; define diamond substrate
				(size infinity infinity csz)
				(material (make dielectric (index nDiamond)))
		)
	))
)

(set! pml-layers (list
			(make pml (thickness wPML)
			)
		)
)

(set-param! resolution res)

(define-param fcen 0.15699)			; center frequency is ZPL wavelength
(define-param df 0.002)				; pulse width for flux measurements

(set! sources					; define Gaussian source appropriate for TE/TM
	(list
		(make source
			(src
				(make gaussian-src	(frequency fcen)
							(fwidth df)
				)
			)
			(component Hz)
			(center (+ (* rGaP -1) (/ wGaP_ring 2)) (- (/ csy 2) wPML 1) (/ hGaP 2))
			(size wGaP_ring 0 hGaP)
		)
```

```
        )
)

(define-param nfreq 101)                                ; number of frequencies at which to compute flux

(define initial                                         ; initial flux in left waveguide – use for initialization
        (add-flux fcen df nfreq
                (make flux-region
                        (center (+ (* rGaP -1) (/ wGaP_ring 2)) (- (/ csy 2) wPML lGaP_WG) (/ hGaP 2))
                        (size (* wGaP_ring 2) 0 (* hGaP 2))
                )
        )
)

(define trans                                           ; transmitted flux in right waveguide
        (add-flux fcen df nfreq
                (make flux-region
                        (center (- rGaP (/ wGaP_ring 2)) (- (/ csy 2) wPML lGaP_WG) (/ hGaP 2))
                        (size (* wGaP_WG 2) 0 (* hGaP 2))
                )
        )
)

(define coupled
        (add-flux fcen df nfreq
                (make flux-region
                        (center (- (+ padx rGaP) 1) (- (/ csy 2) wPML lGaP_WG rGaP gap (/ wGaP_WG 2)) (/
                                hGaP 2))                ; close to edge of cell so that all leaky modes dis.
                        (size 0 (* wGaP_WG 2) (* hGaP 2))
                )
        )
)

(define coupled2
        (add-flux fcen df nfreq
                (make flux-region
                        (center (* -1 (- (+ padx rGaP) 1)) (- (/ csy 2) wPML lGaP_WG rGaP gap (/ wGaP_WG
                                2)) (/ hGaP 2))
                        (size 0 (* wGaP_WG 2) (* hGaP 2))
                )
        )
)
(run-sources
        (stop-when-fields-decayed 50 Hz (vector3 (- rGaP (/ wGaP_ring 2)) (- (/ csy 2) wPML lGaP_WG) (/ hGaP
                                        2)) 1e-10)
        (at-beginning output-epsilon)
        (at-every 250 (output-png Hz "-Zc dkbluered")); -C $EPS"))
)

(display-fluxes initial coupled coupled2 trans)
```

C.3 3-D GaP disk resonator quality factor as function of resonator-waveguide spacing

```
(reset-meep)

(define-param nGaP 3.31)                ; refractive index GaP resonator
(define-param hGaP 1.4)                 ; height GaP layer

(define-param rGaP 5)                   ; radius of GaP disk

(define-param wGaP_WG 1)                ; width of the GaP waveguide to couple to
(define-param gap 0.7)                  ; resonator-waveguide spacing

(define-param hSiOx 0.4)                ; height SiO2 resist layer
(define-param nSiOx 1.54)               ; refractive index SiO2 at 637 nm

(define-param nDiamond 2.4)             ; refractive index diamond resonator
(define-param diamond_etch 5.5)         ; etch depth diamond
(define-param diamond_base_disk 6)      ; width diamond pedestal

(define-param padx 6)                   ; padding in x
(define-param pady 6)                   ; padding in y
(define-param padz 6)                   ; padding in z

(define-param wPML 2)                   ; width PML

(define csx (* 2 (+ rGaP padx wPML)))   ; define cell size in x
(define csy (* 2 (+ rGaP pady wPML)))   ; define cell size in y
(define csz (* 2 (+ hGaP padz wPML)))   ; define cell size in z

(define-param rt 2000)                  ; run time (after sources for gaussian source)
(define-param res 10)                   ; resolution

(set! geometry-lattice                  ; define simulation cell
        (make lattice (size csx csy csz)
        )
)

(set! geometry
        (list
                (make cylinder          (center 0 0 (/ hGaP 2))                 ; define GaP cylinder
                                        (height hGaP)
                                        (radius rGaP)
                                        (material (make dielectric (index nGaP)))
                )
                (make cone              (center 0 0 (/ diamond_etch -2))        ; define diamond cone
                                        (height diamond_etch)
                                        (radius diamond_base_disk)
                                        (radius2 rGaP)
                                        (material (make dielectric (index nDiamond)))

                )
                (make cylinder          (center 0 0 (+ hGaP (/ hSiOx 2)))       ; define SiO2 top layer
                                        (height hSiOx)
                                        (radius rGaP)
                                        (material (make dielectric (index nSiOx)))
                )
```

```
                (make block             (center 0 (* (+ rGaP gap (/ wGaP_WG 2)) -1) (/ hGaP 2))
                                                                        ; define GaP waveguide to couple to
                                        (size infinity wGaP_WG hGaP)
                                        (material (make dielectric (index nGaP)))
                )
                (make block             (center 0 (* (+ rGaP gap (/ wGaP_WG 2)) -1) (/ diamond_etch -2))
                                                                ; define diamond waveguide to couple to
                                        (size infinity wGaP_WG diamond_etch)
                                        (material (make dielectric (index nDiamond)))
                )
                (make block             (center 0 (* (+ rGaP gap (/ wGaP_WG 2)) -1) (+ hGaP (/ hSiOx 2)))
                                                                ; define SiO2 layer on GaP waveguide
                                        (size infinity wGaP_WG hSiOx)
                                        (material (make dielectric (index nSiOx)))
                )
                (make block             (center 0 0 (- (/ diamond_etch -1) (/ csz 2)))  ; define diamond substrate
                                        (size infinity infinity csz)
                                        (material (make dielectric (index nDiamond)))
                )
        )
)

(set! pml-layers (list
                        (make pml (thickness wPML)
                        )
                )
)

(set-param! resolution res)

(define-param fcen 0.15699)                     ; center frequency is ZPL wavelength
(define-param df 0.01)                          ; pulse width for gaussian source and flux measurements

(set! sources                                   ; define gaussian source appropriate for TE/TM
        (list
                (make source
                        (src
                                (make gaussian-src      (frequency fcen)
                                                        (fwidth df)
                                )
                        )
                        (component Hz)
                        (center 0 (- rGaP 0.5) (/ hGaP 3))
                        (size 0 0 0)
                )
        )
)

(run-sources+ rt
        (at-beginning output-epsilon)
        (at-end output-hfield-z)
        (after-sources (harminv Hz (vector3 0 (* (- rGaP 0.5) -1) (/ hGaP 2)) fcen df))
)
```

C.4 2-D out-of-plane GaP grating on diamond

```
(reset-meep)

(define-param nGaP 3.31)                ; refractive index GaP resonator
(define-param hGaP 1.4)                 ; height of the GaP layer
(define-param lGaP 80)                  ; length GaP waveguide
(define-param period_gr 2)              ; period GaP grating
(define-param nperiod 10)               ; number of grating periods
(define-param duty_cycle 0.4)           ; duty-cycle GaP grating

(define-param nDiamond 2.4)             ; refractive index diamond substrate
(define-param diamond_etch 6)           ; etch depth diamond

(define-param pad 12)                   ; padding between grating and PML
(define-param wPML 3)                   ; width PML

(define csx (+ (* nperiod period_gr) lGaP (* 2 wPML) pad))          ; define cell size in x
(define csy (+ hGaP (* 2 (+ pad wPML))))                            ; define cell size in y

(define-param rt 500)                   ; run time (after sources for gaussian source)
(define-param res 10)                   ; resolution

(set! geometry-lattice                  ; define cell
        (make lattice (size csx csy no-size)
        )
)

(define-param no-grating true)          ; measure initial flux into the waveguide without reflection from
                                        ; the grating
(set! geometry
        (if no-grating
                (list
                        (make block             (center 0 (/ hGaP 2))           ; define GaP waveguide
                                                (size infinity hGaP infinity)
                                                (material (make dielectric (index nGaP)))
                        )
                        (make block             (center 0 (/ csy -2))           ; define diamond substrate
                                                (size infinity csy infinity)
                                                (material (make dielectric (index nDiamond)))
                        )
                )
        (append
                (list
                        (make block             (center 0 (/ hGaP 2))           ; define GaP waveguide
                                                (size infinity hGaP infinity)
                                                (material (make dielectric (index nGaP)))
                        )
                        (make block             (center 0 (/ csy -2))           ; define diamond substrate
                                                (size infinity csy infinity)
                                                (material (make dielectric (index nDiamond)))
                        )
                )
                (geometric-object-duplicates (vector3 period_gr 0) 0 nperiod    ; define GaP grating
                        (make block             (center   (+ (/ csx -2) wPML lGaP (* (- 1 duty_cycle)
                                                        period_gr 0.5)) (+ (/ hGaP 2) (/ diamond_etch -2)))
```

```
                                        (size (* (- 1 duty_cycle) period_gr) hGaP)
                                        (material air)
                                )
                        )
                ))
)

(set! pml-layers (list
                                (make pml (thickness wPML)
                                )
                        )
)

(set-param! resolution res)

(define-param fcen 0.15699)                             ; center frequency is 637 nm

(define-param df 0.002)                                 ; pulse width for flux measurements

(define-param nfreq 101)                                ; number of frequencies to compute flux for

(set! sources                                           ; define appropriate gaussian source
        (list
                (make source
                        (src    (make gaussian-src      (frequency fcen)
                                                        (fwidth df)
                                )
                        )
                        (component Ey)
                        (center (+ (/ csx -2) wPML 1) (/ hGaP 2))
                        (size 0 hGaP)
                )
        )
)

(define incident                                                ;  flux incident on grating
        (add-flux fcen df nfreq                                 ;  use for initialization without grating structures
                (make flux-region       (center 0 (/ hGaP 2))
                                        (size 0 (* hGaP 2))
                )
        )
)

(define above                                                   ; flux coupled into air
        (add-flux fcen df nfreq
                (make flux-region       (center (+ (/ csx -2) wPML lGaP (/ (* nperiod period_gr) 2)) (+ hGaP
                                        2))
                                        (size (* (+ nperiod 1) period_gr) 0)
                )
        )
)

(define underneath                                              ; flux diffracted toward bottom of grating
        (add-flux fcen df nfreq
                (make flux-region       (center (+ (/ csx -2) wPML lGaP (/ (* nperiod period_gr) 2)) (- (*
                                        diamond_etch -1) 2))
```

```
                                        (size (* (+ nperiod 1) period_gr) 0)
                )
        )
)

(define transmitted                                     ; flux transmitted to the right of grating structures
        (add-flux fcen df nfreq
                (make flux-region       (center (- (/ csx 2) wPML 5) (/ hGaP 2))
                                        (size 0 (* hGaP 2))
                )
        )
)

(run-sources+ rt
        (at-beginning output-epsilon)                   ; output refractive index at all points
        (at-every 50 (output-png Ey "-Zc bluered"))     ; output field every 50 time steps
        (at-end output-efield-y)                        ; output respective fields at end of simulation
        (at-end output-efield-z)
        (at-end output-hfield-y)
        (at-end output-hfield-z)
)

(display-fluxes incident above underneath transmitted)          ; output fluxes
```

C.5 2-D Taper

```
(reset-meep)

(define-param nGaP 3.31)                    ; refractive index GaP

(define-param wGaP_WG1 1)                   ; width WG1
(define-param lGaP_WG1 10)                  ; length WG1

(define-param wGaP_WG2 20)                  ; width WG2
(define-param lGaP_WG2 20)                  ; length WG2

(define-param taper 10)                     ; length taper

(define-param pad 17)                       ; padding between grating and PML
(define-param wPML 3)                       ; width PML

(define csx (+ wGaP_WG2 (* 2 (+ wPML pad))))                ; define cell size in x
(define csy (+ lGaP_WG1 lGaP_WG2 taper (* 2 wPML)))         ; define cell size in y

(define-param res 8)                        ; resolution

(set! geometry-lattice                      ; define cell
        (make lattice (size csx csy no-size)
        )
)

(define-param no-taper true)                ; measure initial flux into the waveguide without any reflections

(set! geometry
        (if no-taper
                (list
                        (make block     (center 0 (- (/ csy 2)))
                                        (size wGaP_WG1 csy)
                                        (material (make dielectric (index nGaP)))
                        )
                )
        (list
                (make block     (center 0 (- (/ csy 2) (/ (+ lGaP_WG1 wPML) 2)))     ; define narrow GaP WG
                                (size wGaP_WG1 (+ lGaP_WG1 wPML))
                                (material (make dielectric (index nGaP)))
                )
                (make block     (center 0 (+ (/ csy -2) (/ (+ lGaP_WG2 wPML) 2)))    ; define wide GaP WG
                                (size wGaP_WG2 (+ lGaP_WG2 wPML))
                                (material (make dielectric (index nGaP)))
                )
                (make cone      (center 0 (- (/ csy 2) lGaP_WG1 wPML (/ taper 2)))
                                (radius (/ wGaP_WG2 2))
                                (radius2 (/ wGaP_WG1 2))
                                (height taper)
                                (axis 0 1 0)
                                (material (make dielectric (index nGaP)))
                )
        ))

)
```

```
(set! pml-layers   (list
                        (make pml (thickness wPML)
                        )
                )
)

(set-param! resolution res)

(define-param fcen 0.15699)                ; center frequency is resonance wavelength

(define-param df 0.002)                    ; pulse width for flux measurements

(define-param nfreq 101)                   ; number of frequencies to compute flux for


(set! sources
        (list
                (make source
                        (src      (make gaussian-src      (frequency fcen)
                                                          (fwidth df)
                                  )
                        )
                        (component Hz)
                        (center 0 (- (/ csy 2) wPML 1))
                        (size wGaP_WG1 0)
                )
        )
)

(define incident                           ; flux incident on taper – use for initialziation
        (add-flux fcen df nfreq
                (make flux-region
                        (center 0 (- (/ csy 2) (- lGaP_WG1 1) wPML))
                        (size (* wGaP_WG1 2) 0)
                )
        )
)

(define transmitted                        ; flux after taper
        (add-flux fcen df nfreq
                (make flux-region
                        (center 0 (+ (/ csy -2) (+ wPML 1) wPML))
                        (size (* wGaP_WG2 1.6))
                )
        )
)

(run-sources
        (stop-when-fields-decayed 100 Hz (vector3 0 (+ (/ csy -2) (- lGaP_WG2 1) wPML)) 1e-4)
        (at-beginning output-epsilon)
        (at-every 50 (output-png Hz "-Zc bluered"))
        (at-end output-hfield-z)
)

(display-fluxes incident transmitted)
```

D Current limitations for the realization of large-scale hybrid GaP\diamond networks integrated with NV- centers in diamond

D.1 Impact of fabrication conditions on near-surface NV- defects in diamond

There is concern that exposure of NV^- defects to electron radiation during EBL processing may result in a conversion of NV^- to NV^0, therefore leading to the reduced NV^- counts rates discussed in the previous section [20]. Confocal microscopy of the filtered NV^- PSB and PL spectroscopy are employed to determine any effects of the GaP transfer and electron beam exposure on the defects in the diamond substrate. Measurements are taken after the GaP transfer and an EBL step, respectively. Fig. D.1.1 displays an optical micrograph of the GaP sheet on diamond and a corresponding confocal image. While the PL spectra recorded on the GaP layer

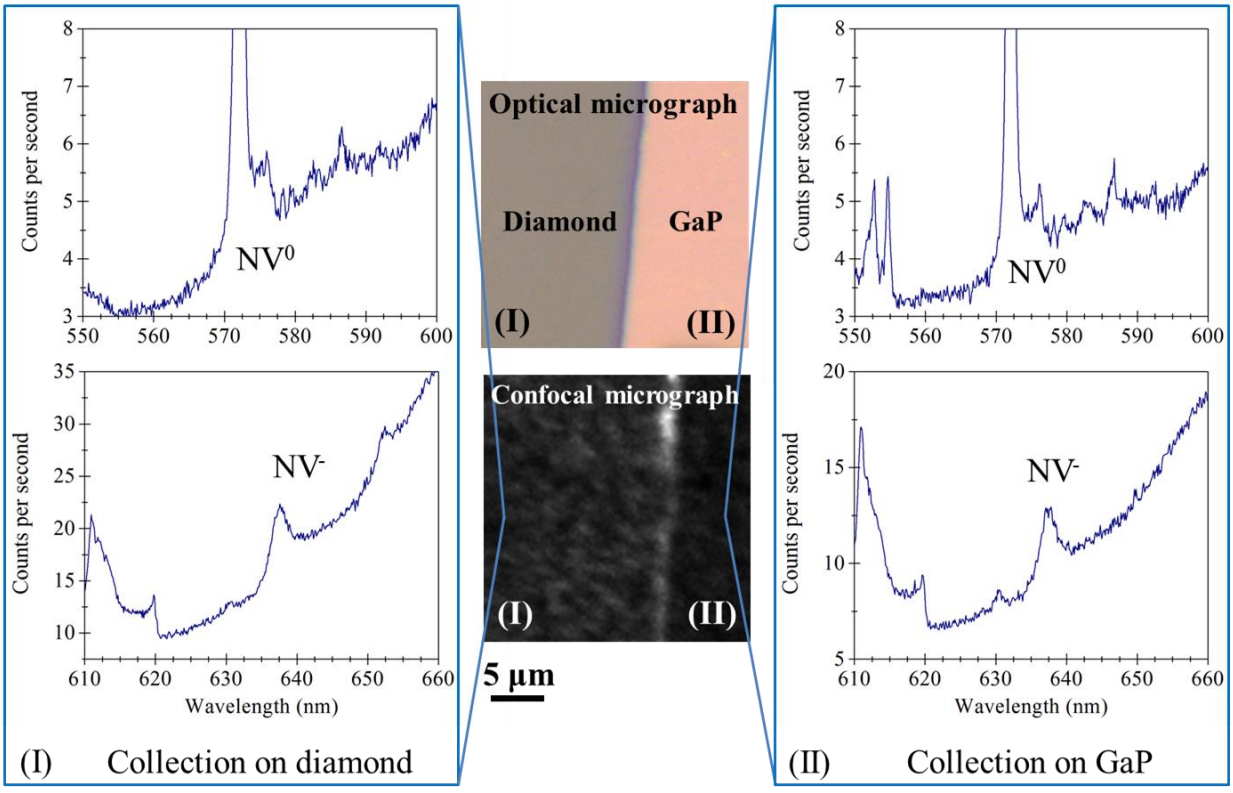

Fig. D.1.1: Effect of GaP transfer on NV^- brightness. Optical micrograph and confocal imaging of filtered NV^- PSB emission of region with bare diamond substrate and GaP sheet bonded via van-der-Waals forces. The confocal micrograph indicates 3 to 4 NV^- present in each excited spot. The room-temperature PL spectra taken on diamond (left panel) and GaP (right panel) do not indicate a significant conversion of NV^- to NV^0. Spectra are taken with 3.5 mW excitation (532 nm).

appear darker, no significant difference in the NV^- to NV^0 ratio can be observed. However, the NV^- count rates appear significantly higher than the one measured for the devices in chapter 6.

The PL measurements are repeated after an EBL exposure to determine if there is an effect of electron beam irradiation on the NV^- defects. Selected areas on the sample are exposed with a 100 kV, 2400 μCcm^{-2} electron beam. The same exposure conditions are used for the HSQ resist process. Fig. D.1.2 displays an optical micrograph of the substrate with the exposed regions appearing as dark resist squares. The confocal micrograph shows a bright fluorescence signature in these areas, indicative of fluorescence from the resist. PL spectra are recorded for exposed and unexposed areas on diamond and GaP, respectively.

The top panel shows the spectra taken on the diamond substrate. While the overall signal appears higher, likely due to the background HSQ fluorescence, similar signals can be obtained for both the NV^0 and NV^- ZPL peaks in both locations. The spectra recorded on and off the EBL square show similar NV^- to NV^0 ratios. Hence, the NV^- appear robust to the GaP transfer process as well as the EBL parameters used for the definition of the HSQ resist pattern. It is therefore currently not possible to determine the cause of the apparent conversion of NV^- to NV^0 observed for the devices fabricated in chapter 6.

D.2 Considerations for a future realization of large-scale hybrid GaP\diamond optical networks integrated with near-surface NV^- centers

D.2.1 Variation in resonance wavelengths in a large device array

Ideally, for enhancement and collection of the NV^- ZPL, the resonance wavelength of each cavity and the ZPL center wavelength of a single defect center coupled to this cavity are identical. In addition, large-scale entanglement networks rely on the interference of photons with identical wavelengths, hence, requiring optical cavities with identical resonance conditions. Fig.

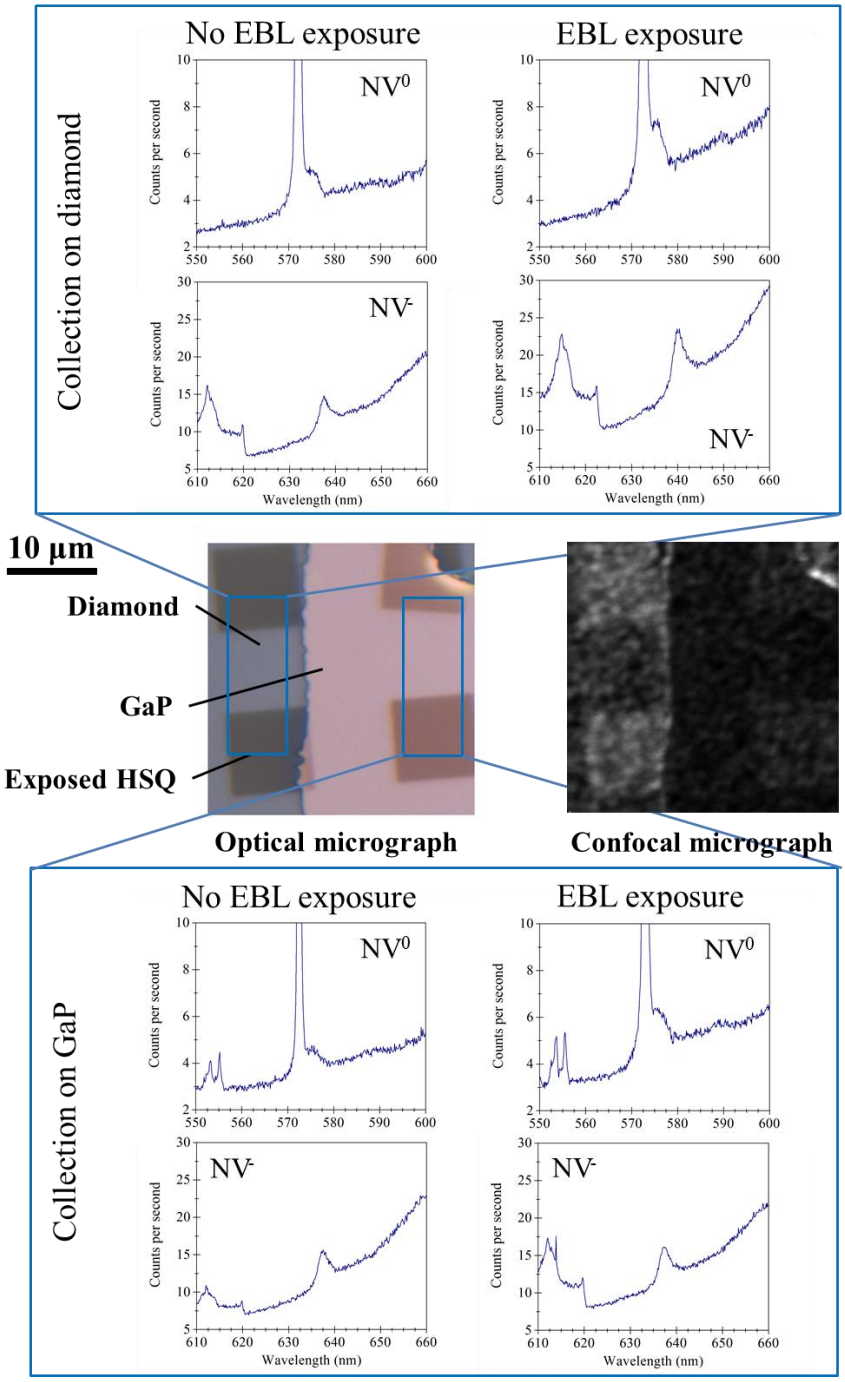

Fig. D.1.2: Effect of electron beam exposure on near-surface NV^- centers. Optical micrograph and confocal imaging of filtered NV^- PSB emission of region showing HSQ resist squares on both diamond and GaP. The PL spectra recorded for both diamond and diamond with electron beam exposure (top panel) as well as GaP and GaP with electron beam exposure (bottom panel) show similar NV^- to NV^0 ratios in unexposed and exposed areas. Spectra are taken at room temperature with 3.5 mW 532 nm excitation.

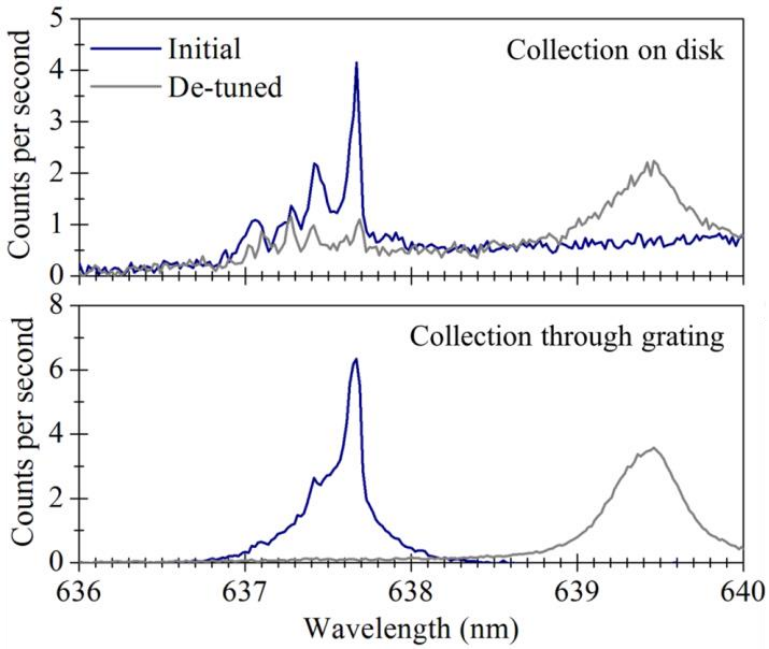

Fig. D.2.1: 1.5 μm diameter cavity with resonance mode aligned with NV^- ZPL. De-tuning of the cavity resonance by the Xe gas condensation technique is used to reveal all uncoupled NV^- centers. Selected NV- lines can be coupled out in the unturned state. The NV^- are excited with a 2.5 mW, 532 nm cw laser Measurements are carried out at 25 K.

D.2.1 displays a device with the resonance mode overlapping with, and possibly enhancing, the NV^- spectral lines (blue line). The scattered PL collected from the top of the disk is shown in the the top panel, while the PL collected through the grating is graphed at the bottom. De-tuning of the cavity mode using the gas condensation technique described in chapter 6 reveals the individual NV^- ZPLs (grey line).

However, current material limitations and fabrication imperfections limit the realization of numerous devices with identical resonance characteristics. Fig. D.2.2 summarizes the resonance wavelengths measured for 185 devices with different diameters. A broad range of resonance wavelengths is visible for each group of devices. The red band illustrates the tuning range available for red-tuning of the single devices using a gas condensation technique as discussed

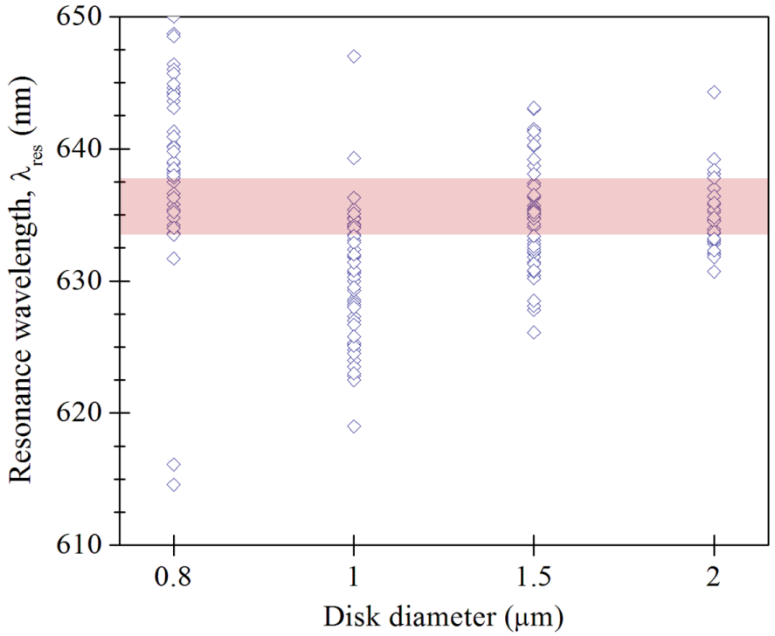

Fig. D.2.2: Resonance wavelengths measured for an array of 185 disk resonators coupled to bus waveguides on the CVD diamond substrates. The resonance wavelengths are determined from transmission measurements of the disk resonators excited with 2.5 mW, 532 nm cw laser light at 82 K in a Janis ST-500 cryostat. The red band indicates the wavelength range available for red-tuning of the resonator wavelengths onto the NV^- ZPL using the gas condensation technique.

above. The broad range in resonance wavelengths can be attributed to both material imperfections and fabrication issues: the single-crystalline GaP layers are grown on small pieces of GaP. Due to to limited material availability the entire substrate is used for the GaP transfer process and device fabrication. Irregularities in GaP height and structure particularly at the edges of the small pieces may result in variations in the resulting device structures. Furthermore, the lithography process may cause variations in the device size, especially in the outer regions of the mm^2-sized diamond substrates where significant variations in resist height can be found. However, these issues may be overcome with higher-quality GaP layers, improved processing, and larger substrates.

D.2.2 Limited quality factors

Another challenge for the enhancement of the spontaneous emission rates of NV^- ZPL photons are the limited quality factors currently realized. High cavity quality factors are essential for strong Purcell enhancement of the NV^- ZPL, and efficient coupling of the NV^- emission to bus waveguides. Fig. D.2.3(a) displays the measured loaded quality factors Q_l for selected GaP cavities on diamond; these devices show coupling of their resonance mode through the grating and exhibit NV^- ZPL signature in their PL spectrum. Fig. D.2.3(b) displays the corresponding simulated loaded quality factors for each diameter as function of the waveguide-resonator spacing, as obtained through 3-D FDTD simulations. The highest quality factors found for coupled devices are ~ 2,500 for 1 μm diameter, ~ 4,100 for 1.5 μm diameter, and ~ 3,900 for 2 μm diameter. With simulated minimum mode volumes of 0.022 μm^3, 0.036 μm^3, and 0.056 μm^3 for the respective disk size, the maximum achievable Purcell enhancements in these structures are ~ 18 for the 1 and 1.5 μm disks, and ~ 10 for the 2 μm disks. Taking into account the non-ideal positioning and orientation of NV- centers in the diamond substrate, these numbers are expected to be significantly lower for real coupling scenarios. Hence, an increase in the intrinsic

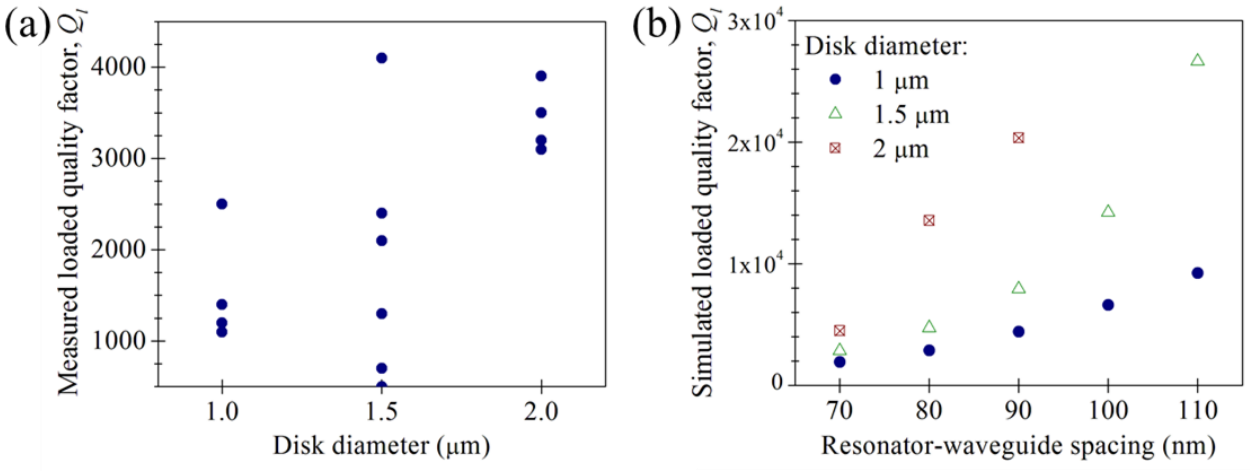

Fig. D.2.3: Loaded quality factors Q_l measured for GaP disk resonators with varying diameters and resonances within the tuning range of the gas condensation technique (634 to 637 nm). Only devices that exhibit NV^- characteristics in their spectra, and can couple the mode through the gratings are considered.

quality factors of the disk will be necessary to significantly increase the spontaneous emission into the NV^- ZPL if the defects are coupled to GaP cavities on diamond.